Chapter 4
Biological Responses

Ken-ichi Yano, Lea Rems, Tadej Kotnik, Damijan Miklavčič, James C. Weaver, Kyle C. Smith, Reuben S. Son, Thiruvallur R. Gowrishankar, P. Thomas Vernier, Zachary A. Levine, Marie-Pierre Rols, Justin Teissie, Lluis M. Mir, Andrei G. Pakhomov, Peter Nick, Wolfgang Frey, David A. Dean, Keiko Morotomi-Yano, Robert E. Neal II, Suyashree Bhonsle, Rafael V. Davalos, and Stephen J. Beebe

Abstract Cells are the structural and functional unit of all living organisms and exhibit fundamental properties of life. Cells are surrounded by the cell membrane and subdivided into various compartments. Pulsed electric fields (PEFs) exert profound effects on cells by interacting with the cell membrane and other cellular components. This chapter describes the biological effects of PEF at cellular and subcellular levels. First, this chapter begins with the overview of cell exposure to PEF from a biophysical point of view. Second, the interaction of PEF with biological membranes, membrane pore formation, and their physiological significance is described from multifaceted standpoints. Next, this chapter explains subcellular events induced by PEF, including the effect on cytoskeleton and signal transduction.

K.-i. Yano (✉)
Kumamoto University, Kumamoto, Japan
e-mail: yanoken@kumamoto-u.ac.jp

L. Rems • T. Kotnik • D. Miklavčič
Faculty of Electrical Engineering, University of Ljubljana, Ljubljana, Slovenia

J.C. Weaver • K.C. Smith • R.S. Son • T.R. Gowrishankar
Harvard-MIT Division of Health Sciences and Technology, Massachusetts Institute of Technology, Cambridge, MA, USA

P.T. Vernier • A.G. Pakhomov • S.J. Beebe
Frank Reidy Research Center for Bioelectrics, Old Dominion University, Norfolk, VA, USA

Z.A. Levine
Department of Physics, University of California Santa Barbara, Santa Barbara, CA, USA

M.-P. Rols • J. Teissie
Institute of Pharmacology and Structural Biology, CNRS and University of Toulouse, Toulouse, France

L.M. Mir
Vectorology and Antitumor Therapies, UMR 8203, CNRS, Univ. Paris-Sud, Université Paris-Saclay, Gustave Roussy, Villejuif, France

H. Akiyama, R. Heller (eds.), *Bioelectrics*, DOI 10.1007/978-4-431-56095-1_4

Lastly, detailed description on irreversible electroporation and cell death by PEF is provided. The topics covered in this chapter serve as the basis for the applications of PEF in medicine, environmental science, and food and biomass processing.

Keywords Electroporation • Electropermeabilization • Computational model • Cell membrane • Cellular effect • Cell death

4.1 Biophysical Aspects of Cell Exposure to Electric Pulses

Lea Rems, Tadej Kotnik, and Damijan Miklavčič

Abstract Exposure of a cell to an external electric field results in induced transmembrane voltage ($\Delta\Psi_m$) which superimposes onto the membrane resting potential. If the absolute value of $\Delta\Psi_m$ is high enough and present long enough, an increased transmembrane transport of ions as well as charged and neutral molecules can be observed, i.e., the cell membrane electroporates. Theoretical models predict that $\Delta\Psi_m$ (related to increased electric field in the membrane) reduces the energetic barrier for formation of small pores in the membrane lipid bilayer and allows pore expansion and stabilization. Although the process of formation and dynamics of each pore is stochastic, on the scale of cells and tissues, the effects of membrane electroporation only become detectable at $\Delta\Psi_m$ exceeding a certain "critical" value. This critical value has been reported in the range from few hundreds of millivolts to about 1 V; though, it was found that it depends on experimental conditions and cell type. Since $\Delta\Psi_m$ appears to be the driving mechanism of electroporation, it is crucial to know its time and spatial distribution during application of an electric pulse. In this chapter we thus review three different approaches for determining $\Delta\Psi_m$: analytical, numerical, and experimental. Based on combined measurements of $\Delta\Psi_m$ and transmembrane molecular transport, we also demonstrate that transmembrane transport is indeed confined to the membrane regions, where $\Delta\Psi_m$ exceeds a certain critical value.

P. Nick
Botanical Institute, Karlsruhe Institute of Technology, Karlsruhe, Germany

W. Frey
Institute for Pulsed Power and Microwave Technology, Karlsruhe Institute of Technology, Eggenstein-Leopoldshafen, Germany

D.A. Dean
Department of Pediatrics, University of Rochester, Rochester, NY, USA

K. Morotomi-Yano
Institute of Pulsed Power Science, Kumamoto University, Kumamoto, Japan

R.E. Neal II
AngioDynamics Inc., Queensbury, NY, USA

S. Bhonsle • R.V. Davalos
Biomedical Engineering, Virginia Tech, Blacksburg, VA, USA

4.1.1 Cell in the Electric Field

From the electrical point of view, a cell can roughly be described as an electrolyte-resembling solution (the cytoplasm) surrounded by a thin layer of dielectric material (the cell membrane) and immersed into another electrolyte-like solution (the extracellular medium). The cell can be thus considered as a closed capacitor. This (electrically) heterogeneous structure allows electric fields to act particularly on the cell membrane and modify the transmembrane voltage. Modification of the transmembrane voltage can then result in a variety of profound biochemical and physiological responses in biological cells, such as cell migration, modulation of cell growth, triggering of action potentials in excitable cells, and membrane electroporation [1–3].

In practically every cell, there is already an endogenous transmembrane voltage present in physiological conditions, which is termed the *resting potential* (or *resting voltage*). The resting potential arises from a charge imbalance on two sides of the cell membrane and is maintained by a system of ion channels and pumps in the membrane. Typically, the interior of the cell is slightly more negative than its exterior, and the resting potential reaches up to several −10 mV (depending on the cell type), when measured from the inside toward the outside of the cell. When exposed to an external electric field (such as by placing the cell between two electrodes connected to a voltage pulse generator), an additional component termed the *induced transmembrane voltage* and denoted by $\Delta\Psi_m$ is superimposed onto the resting potential. Unlike the resting potential, $\Delta\Psi_m$ is present only for the duration of the exposure to the electric field, is proportional to the electric field strength, and varies with the position on the membrane.

Let us first consider the general physical picture of what happens when the cell is placed between two electrodes, and we change the electric potential on one of the electrodes (i.e., a step change in the voltage between the electrodes). At first instance, an electric field is established between the electrodes. The electric field then acts to rotate (polarize) water and other dipolar molecules, e.g., lipid head groups and proteins. The relaxation time of water molecules in pure water is about 8 ps at room temperature, the relaxation time of water molecules bound to the membrane interface is on the order of 100 ps, lipid head groups on the order of 1 ns, and proteins up to the order of 100 ns [4–6]. Particularly the polarization of dipoles at the water–membrane interface partially contributes to an increase in $\Delta\Psi_m$ [7]. The other contribution comes from redistribution of charged ions and molecules in the extracellular and intracellular solutions by the influence of the electrophoretic force, which begins to charge the membrane. How fast this process is, depends on the cell size and the conductivity of the solutions (the mobility and concentration of charged particles in the solution). For cells in medium with physiological conductivity, it takes up to few microseconds to fully charge the cell membrane; however, in low conductive extracellular medium, this process can also take tens of microseconds [8]. As long as the cell membrane is charging and its transmembrane voltage is changing, the interior of the cell is exposed to the electric

field and the membranes of the intracellular organelles are charged as well. In the first tens of nanoseconds, the voltage induced on an organelle membrane is comparable to the voltage induced on the cell membrane. However, the more the cell membrane is charged, the lower is the electric field inside the cell. Due to lowering of the intracellular electric field, the voltage on the organelle membranes starts to drop. After a certain time, the cell membrane is completely charged and reaches a steady-state value of $\Delta\Psi_m$. The cell membrane at this point acts as a shield, preventing its interior to be exposed to the electric field.

This physical picture can be mathematically described in terms of the partial differential equation:

$$\nabla\left[\left(\sigma+\varepsilon\frac{\partial}{\partial t}\right)\nabla\Psi(x,y,z,t)\right]=0 \tag{4.1}$$

with Ψ denoting the electric potential, σ denoting the electrical conductivity, and ε denoting the dielectric permittivity. If we replace the partial derivative $\partial/\partial t$ with its complex equivalent s, the equation can also be solved in the complex frequency domain for sinusoidal electric fields or arbitrary pulse shape using Laplace transform [9, 10]. This approach is general regardless of the size, shape, and arrangement of the cells, but is only valid as long as the finite speed of electromagnetic wave propagation can be neglected, i.e., we assume that the electric field is established between the electrodes instantly. This equation needs to be solved in every region that can be attributed a certain electrical conductivity σ and electric permittivity ε (Fig. 4.1a). The $\Delta\Psi_m$ can then be calculated as the difference between the electric potentials on each side of the region, representing the membrane.

If at any point $\Delta\Psi_m$ gets high enough to induce sufficient number of conductive pores, the pores allow enhanced ionic transport through the membrane which increases the membrane conductivity by several orders of magnitude. This in turn partially discharges the membrane and thereby reduces $\Delta\Psi_m$ during the pulse [11, 12]. In such case the membrane conductivity has to be considered as a function of $\Delta\Psi_m$ [13], which will be in more detail described in Sect. 4.2. In this chapter, however, we will only consider the case of $\Delta\Psi_m$ for nonporated membrane, where the membrane conductivity can be considered constant.

4.1.2 Determination of the Induced Transmembrane Voltage

For cells with regular shapes (spheres, spheroids, cylinders) that are sufficiently far apart (in dilute suspensions), Eq. (4.1) and thereby the time dependence and spatial distribution of the $\Delta\Psi_m$ can be derived *analytically* [15]. In the case of irregular shapes, cells close to each other (in dense suspensions, cell clusters, tissues), or when including nonlinear equations describing pore formation and pore dynamics accompanied by changes in the membrane conductance, the analytical approach is no longer possible. In such case, Eq. (4.1) has to be solved *numerically*. Another

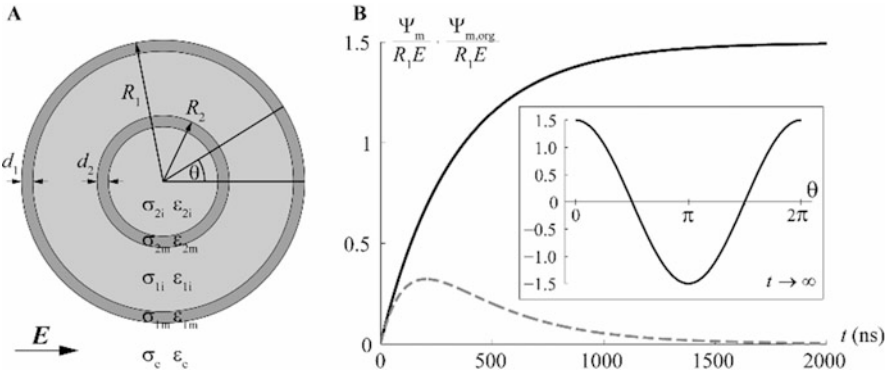

Fig. 4.1 (**a**) Model of a spherical cell with a concentric spherical organelle. The model consists of five regions, each characterized by an electrical conductivity (σ, in S/m) and a dielectric permittivity (ε, in As/Vm). Subscript index "e" corresponds to the extracellular solution, index "1" to the cell and index "2" to the organelle. (**b**) The time course of $\Delta\Psi_m$ (*solid*) and $\Delta\Psi_{m,org}$ (*dashed*), normalized by the electric field strength E and the cell radius R_1, at the point on the membrane, where the $\Delta\Psi_m$ and $\Delta\Psi_{m,org}$ reach the highest value ($\theta = 0$). Calculation was obtained based on analytical approach for solving (4.1) (see Sect. 4.1.2.1) for a spherical cell with radius $R_1 = 10$ μm containing a concentrically positioned spherical organelle with radius $R_2 = 3$ μm in medium with physiological conductivity. Inset shows the normalized $\Delta\Psi_m$ along the cell membrane in steady state, when the charging of the cell membrane is completed (Adapted from Ref. [14])

way for determining the $\Delta\Psi_m$ is by *experimental measurements* with voltage-sensitive fluorescence dyes. In the following subsections, we describe these three methods in more detail.

4.1.2.1 Analytical Derivation

We will begin with a model of an isolated spherical cell placed in a homogeneous electric field. Although biological cells are not perfect spheres, in theoretical treatments they are often considered as such. Particularly for cells in suspensions, this is a reasonable approximation.

If an electric pulse is long enough so that $\Delta\Psi_m$ reaches steady state, the time derivatives in (4.1) are zero, and the partial differential equation simplifies to the Laplace equation: $\Delta\Psi(x, y, z) = 0$. This equation can be solved in a particular coordinate system: for a spherical cell, in spherical coordinates by applying physically realistic boundary conditions (finiteness of Ψ, continuity of Ψ and its derivatives, and asymptotic vanishing of the cell's effect on Ψ with increasing distance from the cell). The detailed derivation of the spatial distribution of $\Delta\Psi_m$ can be found in [15]; we will only outline the results here.

As a first approximation, we can consider that the cell membrane has zero conductivity and that the intra- and extracellular solutions are perfect conductors. Moreover, since the cell membrane acts as a shield, the interior of the cell can also be neglected. This leads to a well-known steady-state Schwan equation:

$$\Delta\Psi_{\mathrm{m}} = 1.5\,ER\cos\theta \tag{4.2}$$

The $\Delta\Psi_{\mathrm{m}}$ is proportional to the electric field strength E and the cell radius R and varies with the cosine of the angle θ between the direction normal to the membrane surface and the direction of the applied electric field (Fig. 4.1, inset in B). The highest absolute value of $\Delta\Psi_{\mathrm{m}}$ is thus established at the points, which are closest to the electrodes (often referred to as the "poles" of the cell). This approximation is well suited for cells, which are placed in a solution of physiological conductivity (~1 S/m); however, for media with much lower conductivity (particularly 0.01 S/m and less [8]), the factor 1.5 reduces considerably. Moreover, when pulses are few microseconds long or less, the time dependence of $\Delta\Psi_{\mathrm{m}}$ of the membrane charging should also be taken into account. The more general expression describing $\Delta\Psi_{\mathrm{m}}$, which also takes into account the membrane conductivity, is the first-order Schwan equation:

$$\Delta\Psi_{\mathrm{m}} = fER\cos\theta\left(1 - e^{-t/\tau_{\mathrm{m}}}\right) \tag{4.3a}$$

$$f = \frac{3\sigma_e\left[3dR^2\sigma_i + \left(3d^2R - d^3\right)(\sigma_m - \sigma_i)\right]}{2R^3(\sigma_m + 2\sigma_e)\left(\sigma_m + \frac{1}{2}\sigma_i\right) - 2(R-d)^3(\sigma_e - \sigma_m)(\sigma_i - \sigma_m)} \tag{4.3b}$$

$$\tau_m = \frac{R\varepsilon_m}{d\frac{2\sigma_e\sigma_i}{2\sigma_e+\sigma_i} + R\sigma_m} \tag{4.3c}$$

Note that both the factor f and the time constant of membrane charging τ_m depend on the properties of the extracellular medium as well as the electrical and geometrical properties of the cell.

If the pulse length is further reduced below 1 μs, the dielectric permittivity of the aqueous media surrounding the cell needs to be taken into account, and expression (4.3) expands into the second-order Schwan equation [10]. This also applies for sinusoidal electric fields with frequencies above 1 MHz.

In the submicrosecond range, particularly for pulses that are on the order of 10 ns, the transmembrane voltage on intracellular organelles becomes comparable to the transmembrane voltage on the cell membrane (Fig. 4.1) [14]. For a spherical organelle positioned concentrically inside a spherical cell, the $\Delta\Psi_{\mathrm{m}}$ (here denoted $\Delta\Psi_{\mathrm{m,org}}$) can also be derived analytically. Such representation of a cell is referred to as the "double-shell model" and is also often used for determining electrical properties of cells using dielectric spectroscopy [6, 16]. The analytical expression is rather complicated and lengthy and will not be presented here, but can be found in [14]. Let us just note that both the $\Delta\Psi_{\mathrm{m}}$ and $\Delta\Psi_{\mathrm{m,org}}$ are proportional to the electric field strength and vary with cosine of θ, but both are also dependent on the electrical properties of the extracellular medium, as well as geometrical and electrical properties of the cell and the organelle. For cells that have a large nucleus, the nucleus can considerably affect the $\Delta\Psi_{\mathrm{m}}$ during the charging phase, so a double-shell model needs to be used also for correctly determining $\Delta\Psi_{\mathrm{m}}$ on the cell

membrane, even if $\Delta\Psi_m$ on the nuclear membrane is not of interest [17]. The $\Delta\Psi_{m,org}$ is also roughly proportional to the size of the organelle, so a higher electric field is required to induce a similar $\Delta\Psi_{m,org}$ on a smaller organelle [18].

In the nanosecond range, $\Delta\Psi_m$ and $\Delta\Psi_{m,org}$ become comparable; therefore, nanosecond pulses which result in sufficiently high electric field can be used to electroporate both the cell membrane and membranes of intracellular organelles. This corroborates with experiments [19–22]. An example is shown in Fig. 4.2, where multiple 60-ns, 50-kV/cm pulses were used to electroporate membranes of postendocytotic vesicles in mouse melanoma cells B16-F1 [22]. Electroporation of vesicles (detected by release of fluorescent dye Lucifer yellow) was also accompanied by plasma membrane electroporation, detected by uptake of propidium ions.

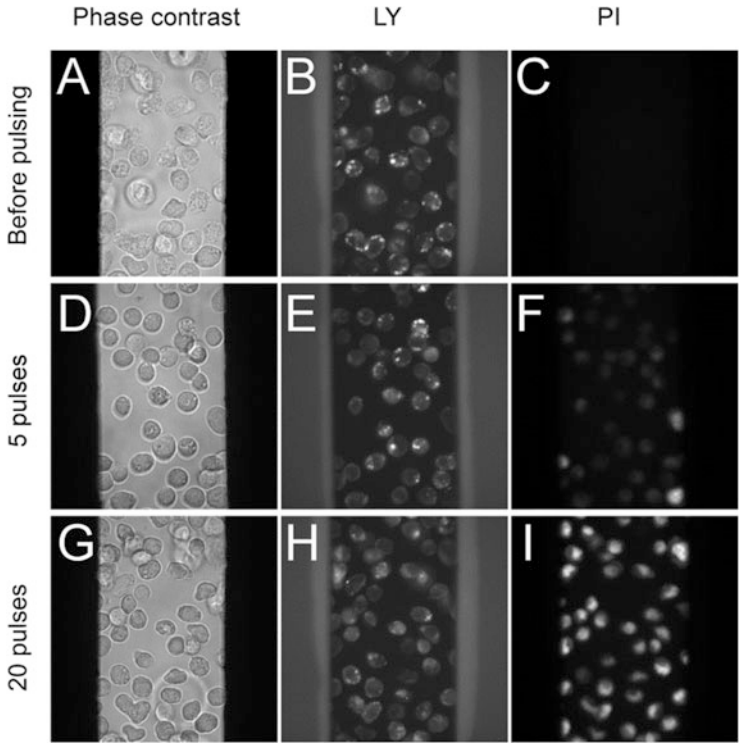

Fig. 4.2 Electroporation of postendocytotic vesicles in mouse melanoma cells B16-F1 cells after applying multiple 60 ns, 50 kV/cm at 1 kHz repetition frequency. Vesicles were loaded with membrane-impermeable dye Lucifer yellow (LY), and the extracellular medium contained membrane-impermeable dye Propidium Iodide (PI). Phase contrast, LY, and PI fluorescence images of cells before pulsing (**a**–**c**), 10 min after applying five pulses (**d**–**f**) or 20 pulses (**g**–**i**). When no pulses are applied, vesicles appear in LY fluorescence image (**b**) as distinct bright dots. The cell membrane is intact as can be seen by the absence of fluorescence in PI fluorescence image (**c**). After application of five pulses, only electroporation of the cell membrane is detected by an increase in PI fluorescence inside the cells (**f**). After 20 pulses, electroporation of vesicles is also detected by release of LY from the vesicles, which can be seen as decrease in fluorescence of the vesicles accompanied by increased LY fluorescence in the cytosol (**h**) (From Ref. [22])

4.1.2.2 Numerical Computation

Numerically, (4.1) can be solved, e.g., with finite difference method [23], finite volume method [24], finite element method [25], distributed equivalent circuit representation [26], or a transport lattice approach [27]. Here, we present the finite element method, which is well suited for handling curved boundaries and has been used by our group to compute the steady-state $\Delta\Psi_m$ of irregularly shaped cells [25, 28]. Finite element computation of $\Delta\Psi_m$ is generally performed in four steps. First, the three-dimensional geometry of the cell(s) of interest is constructed. Second, the continuous geometry is "meshed" into discrete, usually tetrahedral elements, and the partial differential Eq. 4.1 describing the electric potential is transformed by the finite element method into a matrix equation of algebraic expressions. Third, the matrix equation is solved, either directly or iteratively (until reaching adequate convergence). Finally, the transmembrane potential is extracted from the computed spatial distribution of the electric potential as the difference between the electric potential on each side of the membrane. The three-dimensional model of an irregularly shaped cell can be constructed from a sequence of cross-sectional images of the cell under consideration, based on microscopic images of the cell membrane, stained with a fluorescent membrane dye, such as di-8-ANEPPS (Fig. 4.3). This model can be imported into a suitable software package (e.g., Comsol Multiphysics), which discretizes the model into finite elements and solves (4.1) by the finite element method.

Explicit representation of the cell membrane in the model can nevertheless lead to problems. The meshing of the cell membrane, which is over 1000-fold thinner than the dimensions of a typical cell, requires the model to consist of an extremely large number of small finite elements. This consequently requires a large amount of computer memory and long computational time to solve the matrix equation. However, unless the spatial distribution of the electric potential inside the membrane is of interest, this can elegantly be avoided by representing the membrane with a boundary condition describing the transmembrane current density J_n [25]. As far as intracellular and extracellular potential is concerned, the effect of the membrane with thickness d, electrical conductivity σ_m, and electric permittivity ε_m is equivalent to the effect of an interface with thickness 0, surface electrical conductivity σ_m/d, and surface electric permittivity ε_m/d:

$$J_n = \frac{\sigma_m}{d}(\Psi_{\text{int}} - \Psi_{\text{ext}}) + \frac{\varepsilon_m}{d}\frac{\partial}{\partial t}(\Psi_{\text{int}} - \Psi_{\text{ext}}) \tag{4.4}$$

The first term on the right-hand side represents the conductive and the second term the capacitive component of the electric current flowing through the membrane. By assuming that σ_m is a function of $\Delta\Psi_m$, this approach can be extended further, e.g., to simulate the time course of electroporation [28].

In addition to irregular cells, numerical computation can be used for determination of $\Delta\Psi_m$ in cells in dense suspensions. When cells are close to each other, the local field around each cell is affected by other cells, and the spatial distribution of $\Delta\Psi_m$ starts to deviate significantly from that given by (4.2) and (4.3). As the volume

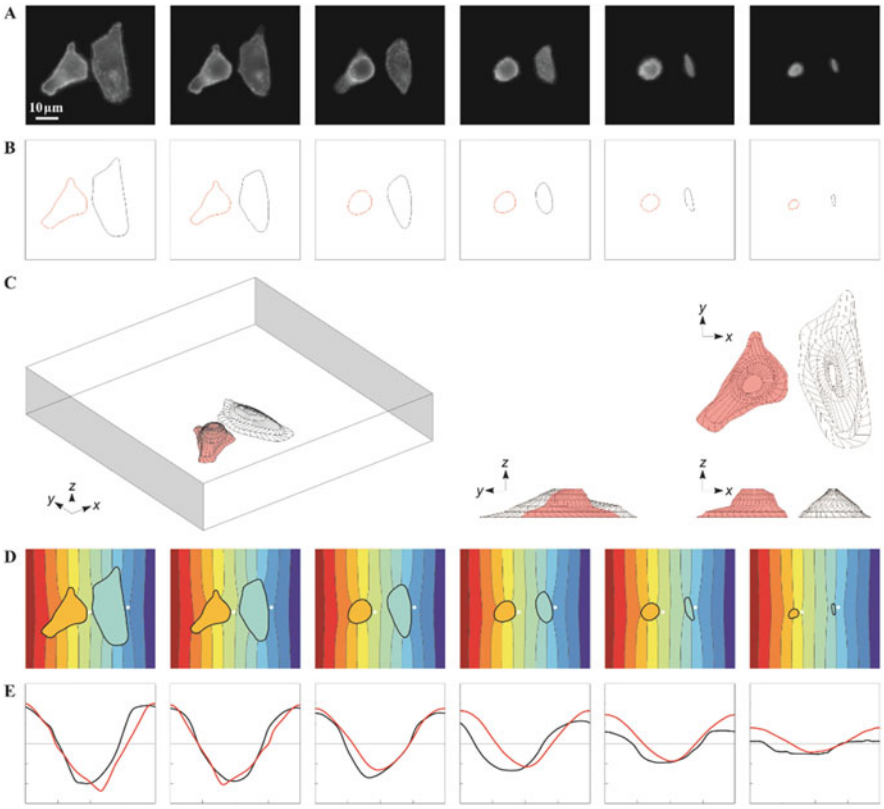

Fig. 4.3 Numerical computation of $\Delta\Psi_m$: (**a**) fluorescence cross-section images of two cells, (**b**) contours of their cross sections, (**c**) three-dimensional model of the cells constructed from the contours, (**d**) computed distribution of electric potential, (**e**) computed $\Delta\Psi_m$ (*red*: left cell, *black*: right cell) (From Ref. [25])

fraction occupied by the cells increases beyond 10 % and approaches 50 %, the factor 1.5 gradually decreases toward 1, and the distribution also starts to diverge from the ideal cosine shape [29, 30]. Due to the lower $\Delta\Psi_m$, the efficiency of electroporation with the same pulse parameters is typically lower in dense suspensions than in dilute ones [31].

4.1.2.3 Experimental Measurement

An alternative to both analytical and numerical determination of $\Delta\Psi_m$ is the experimental approaches. These include measurements with microelectrodes and with potentiometric fluorescent dyes. Microelectrodes (either conventional or patch clamp) were used in pioneering measurements of the action potential propagation [32, 33] and were preferred for their simple use and high temporal resolution. Nevertheless, the invasive nature of microelectrodes, their low spatial resolution,

and physical presence, which distorts the external electric field, are considerable shortcomings. In contrast, measurements by means of potentiometric dyes are noninvasive, offer higher spatial resolution and do not distort the field and by that the $\Delta\Psi_m$, and allow the measurement to be performed on a number of cells simultaneously. Potentiometric dyes such as di-8-ANEPPS [34–36], RH292 [11, 12], and ANNINE-6 [37, 38] have thus become the preferred tool in experimental studies and measurements of $\Delta\Psi_m$, experimental studies of voltage-gated membrane channels, and monitoring of nerve and muscle cell activity. These dyes incorporate into the lipid bilayer of the cell membrane, where they start to fluoresce, with their fluorescence spectra being dependent on the amplitude of the transmembrane voltage; the relative change in fluorescence of these dyes is linearly dependent on the transmembrane voltage in a certain range of voltages. With a suitable experimental setup incorporating a pulse laser, a fast and sensitive camera, and a system for synchronizing the acquisition with the field exposure, these dyes enable monitoring of the time variation of $\Delta\Psi_m$ with a resolution of microseconds, and in the case of ANNINE-6, down to nanoseconds. The latter dye was used to determine $\Delta\Psi_m$ during exposure to electroporating 60-ns long pulses [37, 38]. However, the measurements revealed that $\Delta\Psi_m$ on the cathodic side of the membrane is considerably lower that on the anodic side, which was attributed to reorientation of lipid head groups by the electric field. This reorientation could locally affect the electric field, which is felt by the dye molecules incorporated into the outer leaflet of the membrane bilayer.

The measured voltage can then be compared to theoretical prediction, either by analytical derivation (e.g., the case of spherical cells) or by numerical computation for irregularly shaped cells. In both cases, one obtains a very good agreement, which confirms the applicability of (4.1) for determining the transmembrane voltage (Fig. 4.4), at least in the microsecond and millisecond range and below electroporation threshold, i.e., while membrane conductivity can be considered constant. Figure 4.4c compares $\Delta\Psi_m$ measured with di-8-ANEPPS during a nonporative 50-ms pulse to numerically predicted steady-state $\Delta\Psi_m$.

4.1.3 Correlation Between Induced Transmembrane Voltage and Molecular Transport

To monitor transmembrane molecular transport and thereby determine the electroporated regions of the membrane, cells are exposed to the electroporating electric field in the presence of an otherwise membrane–impermeant fluorescent dye such as propidium iodide (PI). The fluorescence of PI increases by several orders of magnitude when the dye is bound to nucleic acids, due to which the localized entry of the dye through electroporated regions of the membrane into the cell is detected as a local increase in fluorescence. The correlation between the $\Delta\Psi_m$ and the electroporation-mediated transport across the membrane can be demonstrated particularly clearly by combining potentiometric measurements and

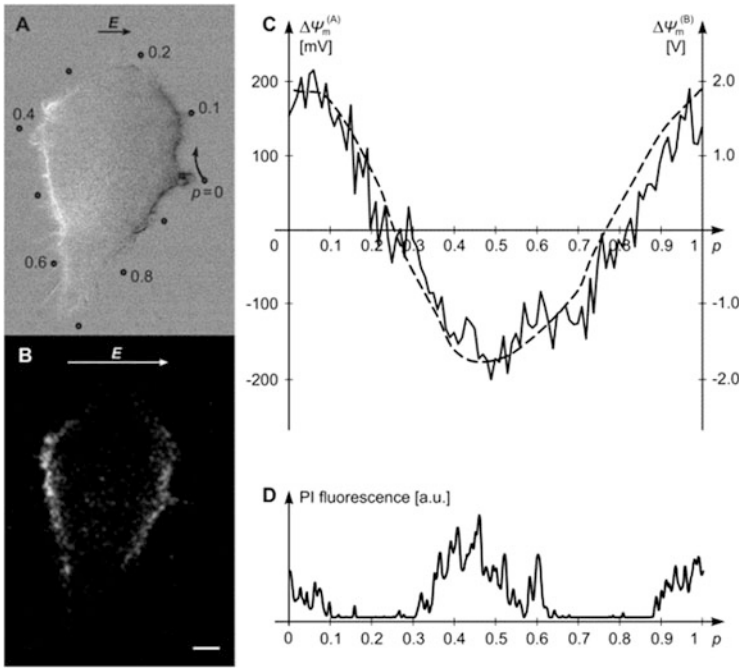

Fig. 4.4 The induced transmembrane voltage ($\Delta\Psi_m$) and electroporation of an irregularly shaped Chinese hamster ovary (CHO) cell: (**a**) changes in fluorescence of di-8-ANEPPS reflecting $\Delta\Psi_m$, with dark regions corresponding to membrane depolarization and bright regions corresponding to membrane hyperpolarization; (**b**) fluorescence of propidium iodide (PI), reflecting transport of PI across the membrane; (**c**) $\Delta\Psi_m$ along the path shown in (**a**) as measured (*black solid*) and as predicted by numerical computation (*gray dashed*); (**d**) fluorescence of PI along the path shown in (**a**) (Adapted from Ref. [45])

monitoring of transmembrane transport on the same cell. An example is shown in Fig. 4.4. These experimental results confirm the theoretical prediction that the highest values of $\Delta\Psi_m$ are found in the membrane regions facing the electrodes (the "poles" of the cell) and show that electroporation-mediated transport is detected in these same regions, i.e., the areas for which the absolute value of $\Delta\Psi_m$ is above a certain critical value. This critical value is though a very rough estimate. It has been reported in the range from few hundreds of millivolts to about 1 V; however, it was found that it depends on experimental conditions and cell type and can vary even among cells of the same type [39]. Furthermore, the threshold of uptake detection depends on the sensitivity of the imaging system and generally on the dye being used for detection of molecular transport [40–43]. Due to stochastic nature of pore formation, higher $\Delta\Psi_m$ is also predicted to be required for formation of a similar number of pores, and hence detectable electroporation, if the pulses are shorter [44]. Albeit the critical value of $\Delta\Psi_m$ cannot be considered as a general predictor of detectable electroporation, the dependence of membrane electroporation and transmembrane molecular transport on sufficiently high $\Delta\Psi_m$ clearly demonstrates that molecular transport is closely correlated to $\Delta\Psi_m$.

4.2 Continuum Modeling for Bioelectrics

James C. Weaver, Kyle C. Smith, Reuben S. Son, and Thiruvallur R. Gowrishankar

Abstract A model is a quantitative hypothesis. For bioelectrics a model predicts what will happen for particular electrical conditions. Here we consider isolated, single cells with a single, outer membrane (plasma membrane or PM). Related models with multiple membranes treat cells with organelles or multiple cells close together (tissue). We use computational models, which can be both precise and complex, while still allowing quantitative testing. Existing models include multiple interactions and parameters and accept a wide range of applied field waveforms as inputs. Complex computational models are increasingly key to science and engineering. Here we present bioelectric modeling based on nonequilibrium processes. Physically, fields drive movement and/or reorientation of entities with permanent or induced charge. Biologically, living cells exist far from equilibrium, driven by metabolism. We recognize both sources of nonequilibrium processes as a basis for bioelectric models. Living cells involve many active processes. Some take place near or within membranes, which amplify externally applied electric fields by responding with larger membrane field changes. These amplified membrane fields couple to cell functions such as voltage-gated channels and the transient pores of electroporation (EP). For bioelectrics the electrical response (transmembrane voltages, local fields) and chemical changes (transport) are of interest. Many early models are passive, with electrical properties remaining fixed when a field is applied. We describe a meshed transport network method, focusing on EP, which causes changing membrane properties. These models' responses can be estimated for fields with strengths of 0–100 kV/cm and durations from ~1 ns to ~1 s, for both idealized and digitized experimental pulse waveforms.

4.2.1 Model Construction

Passive models with analytical expressions for cell responses are well established [10, 48]. Models with irregular membrane geometries and complex physiologic behavior are also established for normal physiology where bioelectrics is unimportant. Here we focus on models with large, spatially distributed membrane conductance changes by EP, using a general method. EP is the generally accepted mechanistic hypothesis for rapid (nanosecond) increases in local membrane conductance by field pulses [46, 47]. EP accounts for key experimental behaviors (e.g., flattening of the transmembrane voltage profile) and transport of dissolved (free) ions and molecules through the outer (plasma) and inner (organelle) membranes. EP is fundamentally nonthermal: there is Joule heating, but temperature rise itself causes insignificant pore creation.

4.2.2 Modeling Based on Nonequilibrium Transport

Models based on transport recognize that (1) fields drive charged species transport, e.g., electrodiffusion of small ions and large molecules, and (2) living cells operate far from equilibrium, e.g., metabolically driven resting potential sources. Basing models on transport inherently allows inclusion of both gentle and steep gradients in space and time. Gradients in electric potential define fields; gradients in solute concentrations (ions and molecules) drive electrodiffusion. Ubiquitous small ions control electrical behavior, while electrodiffusion of larger ions and molecules occurs within bulk media and through dynamic pore populations [46]. Meshing constrained by membrane geometry establishes transport networks [46]. Transport between nodes is governed by established equations, with solutions obtained by Kirchhoff's laws [49]. Here we discuss basic features of our modeling methods. Details and basic equations are publicly available [46, 47].

4.2.3 Simplest Cell Model

For basic concepts we use a cell model with a single curved membrane (cylindrical geometry, Fig. 4.5a, d) [46, 47]. In addition to being the simplest case, it is a starting point for multiple membrane models (Fig. 4.5b, c, e, f). In our models "transport" is general, including sources and sinks for transported free solutes. Even "movement" of pore radius (r_p) within a changing landscape where pores expand and contract is considered transport, mathematically analogous to electrodiffusion of solutes, described by the Smoluchowski equation (SE) [46, 50]. Here we focus on the simplest model (Fig. 4.5a, d).

4.2.4 Pore Models

Models of nanometer-scale pores include cylindrical, toroidal, and trapezoidal holes. Trapezoidal geometry reflects some cylindrical and toroidal features (Fig. 4.6a, b) and compares favorably with molecular dynamic (MD) pore geometries (Sect. 4.1). The trapezoidal model has some of the focusing fields within the flared openings, with the full focusing fields having well-known "spreading resistance" or "access resistance" [46, 47]. Focusing fields guide free charged solutes (ions and molecules, approximated as cylindrical) toward and away from pore interior regions. Within heterogeneous focusing field regions, solutes move by electrodiffusion toward and away from membrane pore interiors. Inside the restrictive, cylindrical pore interior (half the membrane thickness), electrodiffusion is more complicated.

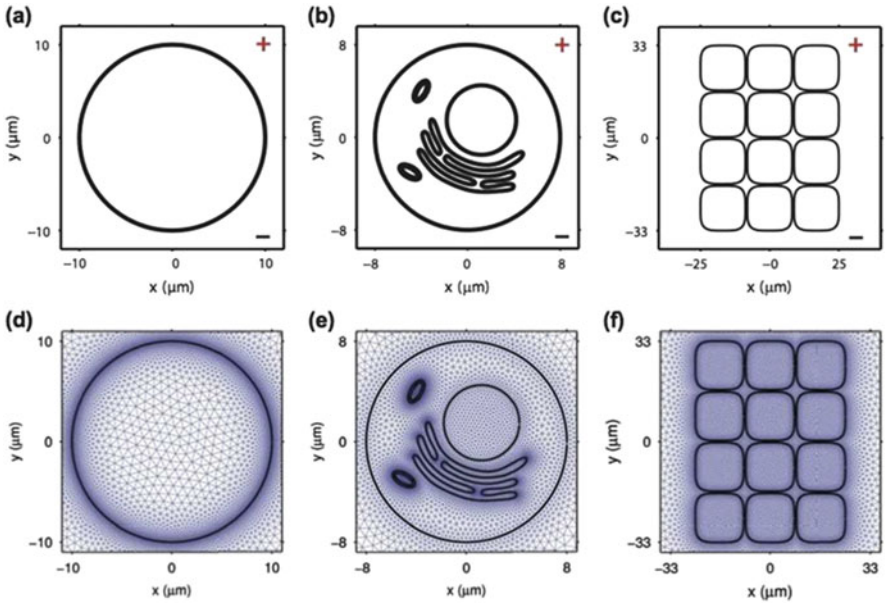

Fig. 4.5 Geometry and meshed transport network for cell models. (**a**) PM with the simplest, single curvature [46, 47]. (**b**) Multiple intracellular membranes, for example, two mitochondria (*ovals*) with mitochondrial outer and inner membranes (MOM and MIM, respectively), a very large endoplasmic reticulum membrane (*convoluted*) and a large double-membrane nuclear envelope (*circular*). As depicted here, a single curve represents either a single or double membrane, but the models have separate membranes, with different electrical properties when appropriate [46]. (**c**) Multiple cell model for studying basic EP-mediated solute transport in tissue. (**d–f**) Corresponding meshed transport networks for (**b–c**)

The mesh interconnects all nodes, with most in bulk aqueous media (Fig. 4.5). The most complex interactions occur in the membrane. Transmembrane node pairs contain local models for fixed (passive) components of the conductive and capacitive membrane properties, a metabolically driven resting potential source, and also a complete nonlinear, hysteretic membrane EP model with (1) an absolute rate equation for pore creation at r^*, (2) the Smoluchowski equation (SE) for pore expansion/contraction within the changing (U_m-dependent) energy landscape (Fig. 4.6c), and (3) pore destruction. The many interconnected interactions yield a cell system model.

The model includes K, the partition factor, which depends on pore size (radius, r_p) and electrical charge (charge number, z_s). Transport also depends on H, the hindrance factor, which is most restrictive for the pore interior. H depends on the relative size of the solute (radius, r_s) and pore radius (r_p) [46]. Electrodiffusion of each solute (e.g., propidium, calcein) is computed separately [47].

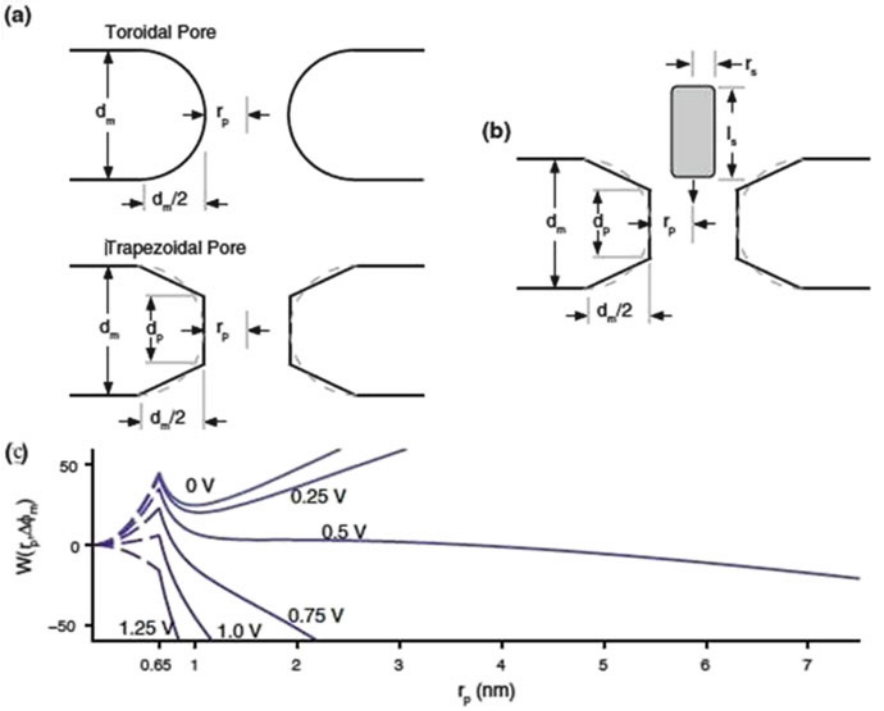

Fig. 4.6 Pore and solute geometries and energy landscape [46, 47]. (**a**) Toroidal and trapezoidal pores. (**b**) Trapezoidal pore with approaching cylindrical solute. (**c**) Pore energy landscapes for transmembrane voltage $U_m = 0$ to 1.25 V

4.2.5 Pore Energy Landscape and Pore Behavior

When a pore is created, it appears in the landscape, W, at r^* (0.65 nm, Fig. 4.6c). The Smoluchowski equation and landscape together govern the resulting "motion" of r_p, with pore expansion equivalent to r_p increasing and for pore contraction r_p decreasing. During a pulse W at each of the many transmembrane node pairs changes, so that pore populations (pore-size histograms) at different membrane sites evolve and eventually vanish postpulse. Pore populations interact through the aqueous portion of the mesh, so that the model's behavior is a system response. The landscape is usually shown for the case with a single minimum size pore ($r_{min} \approx$ 1 nm) present. The landscape is populated by stochastic pore creation at r^*, estimated by an absolute rate equation with a highly nonlinear dependence on U_m. After a typical pulse, the membrane is depolarized ($U_m = 0$). The landscape is then depopulated as pores diffuse to reach a small pore radius r_d slightly below r^* (a model feature) [46]. Due to the landscape's downward slope away from r_d at elevated U_m, a negligible fraction of pores reach r_d during a pulse.

4.2.6 Active and Passive Versions of Cell Models

To understand U_m-mediated effects, we need to know $U_m(t)$ over the PM. Early models use fixed (passive) electrical properties [10, 48]. But experiments [51] showed vividly that the local membrane conductance increases dramatically in some regions of a cell membrane for large field pulses, those now associated with electroporation. This is an active response. For the same membrane geometry, both passive and active versions can be created, with the only difference that electroporation is "knocked out" (omitted) in passive models, leaving only fixed local conductance and capacitance (dielectric) membrane values (Supplementary Information of [47]).

Figure 4.7a is early ($t = 1$ μs) in the long pulse. It exhibits the traditional cosinusoidal passive (dot-dash curve) response, with "approximate amplification" $(R_E)_{max} \approx 2300$, but for the active (solid) curve $(R_E)_{max} \approx 1800$, and at the poles only ~50, the site of appreciable R_E flattening [51]. (b) As in (a) but at 99 μs, end of the short pulse flat peak value. Here the passive case has $(R_E)_{max} \approx 4000$, but the active case has smaller $(R_E)_{max}$ within porated regions, owing to significant expansion of some pores, which increases membrane conductance that diminishes E_m. Both (a) and (b) show voltage division dominated by membrane conductance, which due to poration is much larger for (b) than (a). (c) Early (1 ns) in short pulse with passive and active curves indistinguishable, as only a few pores are created, with insignificant membrane conductance increase. $(R_E)_{max}$ is only ~10, due to dielectric voltage division (displacement current >> conductance density) [13] (Fig. 4.7c). (d) Late (9 ns) in the short pulse, the passive and active responses are indistinguishable except near the poles, where enough pores exist that conduction currents exceed displacement currents. Here $(R_E)_{max} \approx 100$ for the passive case and ≈ 90 for the active case.

Figure 4.7 illustrates important constraints. Comparison of the long pulse (conventional EP) and short pulse (surpa-EP by nsPEF) reveals the increasingly important contribution of dielectric effects as pulse durations are shortened. R_E becomes

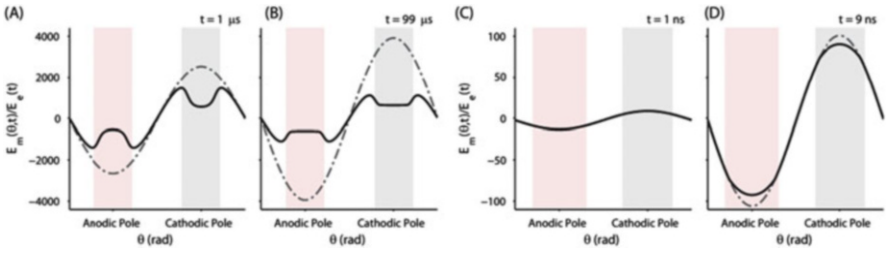

Fig. 4.7 Amplification gain factor, E_m/E_e, is shown as a function of angle at different times. (**a, b**) Show the response to a 1.5 kV/cm, 100 μs pulse at the start and end of the pulse maximum. (**c**, **d**) Show the response to a 40-kV/cm, 10-ns pulse at the start and end of the pulse maximum. The *dash-dotted curve* represents the passive membrane amplification response, in which the dynamic electroporation model has been "knocked out." In (**c**), the two curves are indistinguishable because the onset of electroporation has not occurred [47]. *Light red* and *gray* regions show porated regions

relatively small, and an increasingly large creation rate is needed to compensate for a shorter pore creation time. Both small R_E and short pulse duration tend to decrease pore creation. Nevertheless nsPEF is very effective in porating multiple cell membranes. As field strength increases progressively, smaller organelle membranes are porated, such as the MOM and MIM of mitochondria are permeabilized and then depolarized after the pulse.

4.2.7 Electrical and Poration Behavior

EP is characterized by first rapid and then slow changes. Figure 4.8d, j shows pore number, $N(t)$ for the entire membrane. Figure 4.8a, g shows $U_m(t)$, averaged over quadrants of the membrane. Although the total pore number, $N(t)$, increases for widely used pulses, the pore-size distributions (dynamic pore populations) change during the pulse. Importantly, $U_m(t)$ and $N(t)$ are interrelated, each affecting the other. This complexity arises from rapid electrical interactions within the cell and almost equally rapid changes in membrane properties (pore creation/expansion). This results in spatially distributed, conducting pores of changing sizes, which interact electrically through the aqueous media within the model [46, 47].

Figure 4.8a shows $U_m \approx$ first rising by membrane charging for the long pulse. As U_m approaches ~1 V, a burst of pore creation occurs, creating a large membrane conductance, and U_m falls in ~1 μs to ~0.5 V. This phenomenon is termed reversible electrical breakdown (REB). Figure 4.8g has simpler behavior for the short pulse, with a peak U_m due simply to the pulse maximum ending at 9 ns. For both pulses (Fig. 4.8a, g), pore creation and destruction are well separated on the pulse timescales. Creation rates are finite, so a nonzero time is needed to create enough pores to cause a detectable EP effect. This means there are no general critical values of U_m. For typical pulses longer than a few microseconds, two pore populations evolve during a pulse. One has small pores, while the other has dynamic large pores. At the pulse end, large pores rapidly contract, leaving a narrow distribution of small pores, and these slowly (seconds) vanish stochastically [46, 47].

4.2.8 Solute Transport Rates and Cumulative Amounts

Figure 4.9 shows illustrate influx rates and cumulative amounts (molecule numbers) for transport of two fluorescent probes, calcein and propidium, for the long pulse. This provides estimates of the relative importance of free solute transport during and after a pulse. These show the rates of influx, both during and after the pulse, with postpulse diffusive transport estimated for five 4 s pore lifetimes (20 s), for two versions of the basic model.

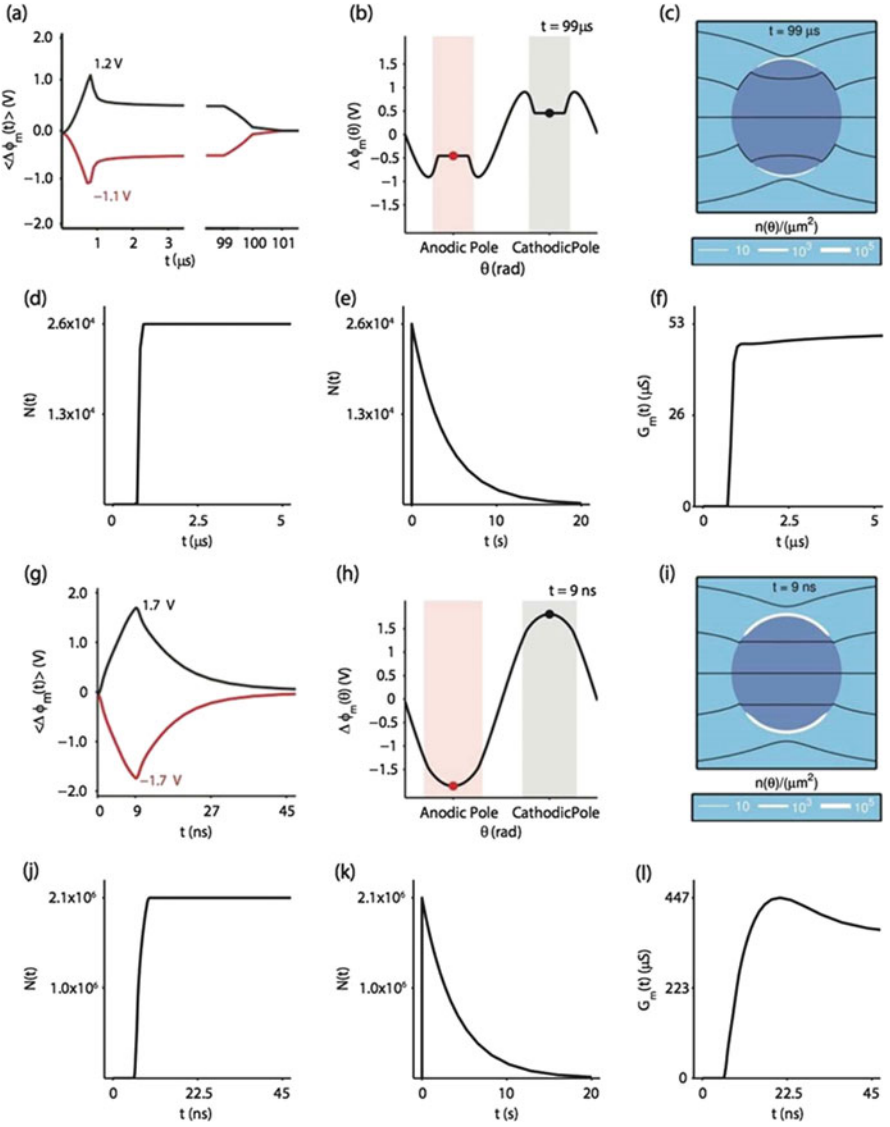

Fig. 4.8 Illustrative EP responses for a "long pulse" (1.5 kV/cm, 100 μs; **a–f**) and a "short pulse" (40 kV/cm, 10 ns; **g–l**). Average transmembrane voltage, $< \Delta\varphi_m(t) >$, is spatially averaged over the polar quadrants. Angular transmembrane voltage, $\Delta\varphi_m(\theta)$, at the end of the pulse maximum shows the spatial heterogeneity in the electrical response across the membrane. Light red and black shaded regions represent electroporated regions of the membrane. Similarly, pore density, $n(\theta)$, at the end of pulse maximum shows the spatial extent of electroporation. The total number of pores, $N(t)$, rises after REB and decreases exponentially after the pulse in accordance with pore lifetime, $\tau_p = 4$ s. Similarly, the total membrane conductance, $G_m(t)$, increases with pore creation and expansion [47], with short pulse creating ~10× larger membrane conductance

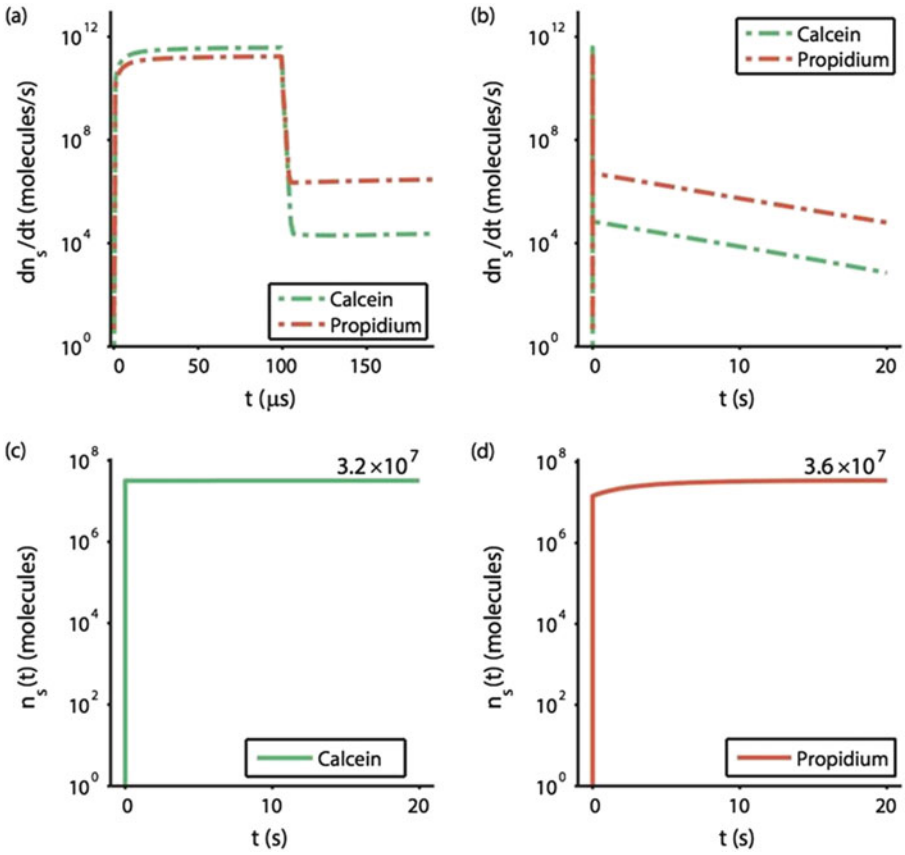

Fig. 4.9 Electrodiffusive transport rates of propidium and calcein, dn_s/dt, into the cell for a 1.5-kV/cm, 100 μs pulse on two different timescales (**a**, **b**) [47]. Cumulative solute influx, $n_s(t)$ (**c**, **d**), shows the total amount of solute inside the cell as a function of time. During the 1.5-kV/cm, 100 μs pulse, 3.2×10^7 molecules of calcein and 1.5×10^7 molecules of propidium are transported into the cell. After the 100 μs pulse, 2.8×10^5 molecules of calcein and 2.1×10^7 molecules of propidium are transported into the cell

4.3 Molecular Models of Lipid Electropores

P. Thomas Vernier and Zachary A. Levine

4.3.1 Molecular Models of Electroporation Before Molecular Dynamics

Early studies of electroporation (electropermeabilization) combined experimental observations of artificial and living cell membranes in porating electric fields with analytical models of the transformation of an impermeant barrier to a permeabilized

membrane. Electroporation at first was understood primarily phenomenologically, as an increase in membrane conductance caused by the application of external electric fields. This change in the electrical properties of the membrane was associated with an increase in the permeability of the membrane to ions and small molecules, but there were at the time no experimental methods capable of revealing the membrane structural modifications that might be involved. Thus the first models of electropermeabilization were based on selected physical properties of lipid bilayers combined with the understanding of cell membrane structure that was available at the time, summarized in the fluid mosaic model [52], and did not include a description of the molecular rearrangements of membrane constituents that must be involved. The phenomenon was clear, but the mechanism was poorly understood.

Even the earliest models of electropermeabilization, however, did not entirely ignore the molecular composition and organization of cell membranes and lipid bilayers. The stochastic membrane defects whose formation is favored when the transmembrane potential is increased were defined, almost from the beginning, not simply as "defects" or as sites of "breakdown", but as populations of membrane-spanning pores, with probabilities of creation and annihilation, subject individually and in composite to expanding and contracting forces. Theoretical models and experimental observations were consistent with pore diameters on the order of 1 nm, comparable to the area occupied by the individual phospholipid molecules making up the lipid bilayer [53]. Placing the electric field-facilitated evolution of a population of transient aqueous pores on the framework of the fluid mosaic model of the cell membrane implied nanometer-scale dimensions for individual pores, but the molecular architecture of the pores themselves was not known.

Not surprisingly, given the absence of observational evidence and the likelihood that none would be forthcoming soon, this lack of knowledge did not prevent theoreticians (and some experimentalists) from picturing lipid electropores in molecular detail, at least in schematic form. Diagrams ("cartoons") of porated membranes, showing the individual phospholipids in the bilayer with the arrangement of the head and tail portions of the molecules emphasized, appear in some of the earliest electropermeabilization papers [54–57]. These drawings demonstrate the conceptualized structures of hydrophobic and hydrophilic pores, and they help to visualize how the head group dipole might participate in pore formation.

Because these schematic views do not include water and because they do not quantitatively represent how head group dipoles respond to the electric fields that are present when pores form, they fostered assumptions that led to incomplete descriptions of the roles of water and head group dipoles in lipid electropore initiation and construction [7, 58, 59]. With no direct observational methods on the horizon, the next step toward a more complete understanding of the mechanisms of electroporation was a physics-based, atomically detailed model of the lipid electropore, through molecular dynamic simulations.

4.3.2 Molecular Dynamic Models of Lipid Bilayers

The term molecular dynamics is commonly applied to two broad categories of molecular models. One kind of molecular dynamics—quantum mechanical (QM)—incorporates quantum mechanical considerations into the electronic interactions, both intramolecular and intermolecular, among the constituent atoms of the system. This approach is necessary when simulating chemical reactions, including electron transfer, or any system in which the conformation or any other property of a molecule is dependent on electronic energy levels or electron density distributions.

Quantum electronic molecular dynamics is computationally demanding, however, which limits simulations in most cases to a relatively small number of atoms and relatively short timescales. Representing pore formation in a lipid bilayer requires the inclusion of hundreds of thousands of atoms and hundreds of nanoseconds, system sizes that are at present out of reach.

The second kind of molecular dynamics—molecular mechanical (MM)—does not explicitly represent electronic states. Instead, MM tracks the mechanical and electrostatic interactions of atoms described by utilizing classical potential functions (with coefficients that are determined by "force fields," in the jargon of molecular dynamics). This greatly reduces the computational complexity per atom, enabling molecular simulations of systems large enough to represent lipid electropore formation.

The mathematics that permit this depend on several assumptions. For instance, the Born–Oppenheimer approximation allows us to calculate nuclear (atomic) trajectories without taking electron distributions into account. Atoms are treated as point masses with fractional charges, classically distributed to mimic the true electronic structure. Bonded interactions are described by three functions: axial (stretching), angular (planar), and torsional (twisting). The functional forms of these functions are harmonic, necessitating the use of spring constants across multiple degrees of freedom. Nonbonded interactions are tabulated over longer ranges (electrostatic) and shorter ranges (van der Waals). Each of these functions are optimized empirically, atom type by atom type, to produce spatially dependent potential energy expressions that map as closely as possible to the experimentally known behavior of the molecules represented in a given system.

A third variant of molecular dynamics, which we may expect to see more in the future, is a hybrid of the quantum and molecular mechanical approaches (QM/MM). In QM/MM, a critical portion of a molecule (e.g., the active site of an enzyme) is described quantum mechanically and then mapped onto a set of molecular mechanical coordinates across the entire system [60].

Within the framework of the molecular mechanical approach, which has proven to be both useful and practical for studies of phospholipid bilayers in electric fields, several levels of detail and definition are possible. One must judge whether the increased precision or accuracy justifies the longer simulation times or the larger number of computing cores needed for a given simulation. For example, instead of

"all-atom" force fields, which represent each individual atom in the system, one may elect to use a "united-atom" model, in which small groups of atoms are treated as single entities. The $–CH_3$ and $–CH_2$ groups in a hydrocarbon chain, including those in the "tail" of a membrane phospholipid, behave very similarly in united-atom and "all-atom" simulations, but the computational demands of united-atom models are considerably smaller. For lipid bilayers, at least, the united-atom approach has proven effective [61, 62].

Some groups have moved even further in this direction, with coarse-grained models that extend the united-atom method to larger atom groups. This has the benefit of further savings in computational costs, but it remains to be seen whether coarse-grained simulations of electroporation are accurate enough to be quantitatively predictive or to capture the details of pore creation and annihilation, which seem to be critically dependent on the interactions of individual water molecules and phospholipid atoms. It seems likely that atomic-scale resolution is necessary, not only to represent the molecule-by-molecule construction of membrane-spanning bridges of intruding water that marks the pore initiation process and the closely coordinated hydration of the phospholipid head groups that follow the water into the membrane interior but also to model the interactions of ions and other solutes with pore walls in simulations of electrophoretic and diffusive transport through electropores.

Additional simulation details for phospholipid bilayer systems that must be taken into account include the specific models chosen for water and inorganic ions and for other constituents such as amino acids, sugars, mononucleotides, and larger molecules. More accurate models, such as those including polarizable bonds (e.g., for water), may be essential for accurate predictions of pore creation time and pore lifetime and for better representations of pore geometries in the presence of different salts at varying ionic strengths and interfacial lipid and water properties at the pore mouth and along the pore walls. Increasing access to more computing power will make the implementation of these options more efficient and standardized within the molecular dynamic community.

Although great insights and improved understanding have come from molecular dynamic simulations of lipid bilayers, it is important to keep in mind the limitations of these models, which constrain what they can tell us about living cell membranes in electric fields. The patch of membrane represented is very small, about one ten-millionth of the area of a typical cell. Even areas of a few hundred square nanometers, where multiple pores might form simultaneously and which would be large enough so that the diverse composition of a cell membrane (multiple lipid types, membrane attachments and associations with intracellular and extracellular structures, membrane proteins) might begin to be represented, are barely within reach. Simulation times are similarly limited by practically available computing power, to less than a microsecond for typical computing clusters. Finally, as mentioned above, most of the systems simulated today in electroporation studies contain only a few lipid types (often only one) and usually no other membrane constituents, the most glaring missing component being membrane proteins.

4.3.3 Molecular Dynamic Simulations of Lipid Bilayers in Electric Fields

To simulate electroporation, we first assemble a membrane. Most molecular dynamic simulations of electroporation in the literature use homogenous, fully hydrated phospholipid bilayers, for reasons discussed above. A system might contain, for example, palmitoyloleoylphosphatidylcholine (POPC, a common phospholipid found in many cell membranes), water, and nothing else (Fig. 4.10). Although this is far from the complexity of a living cell membrane and the

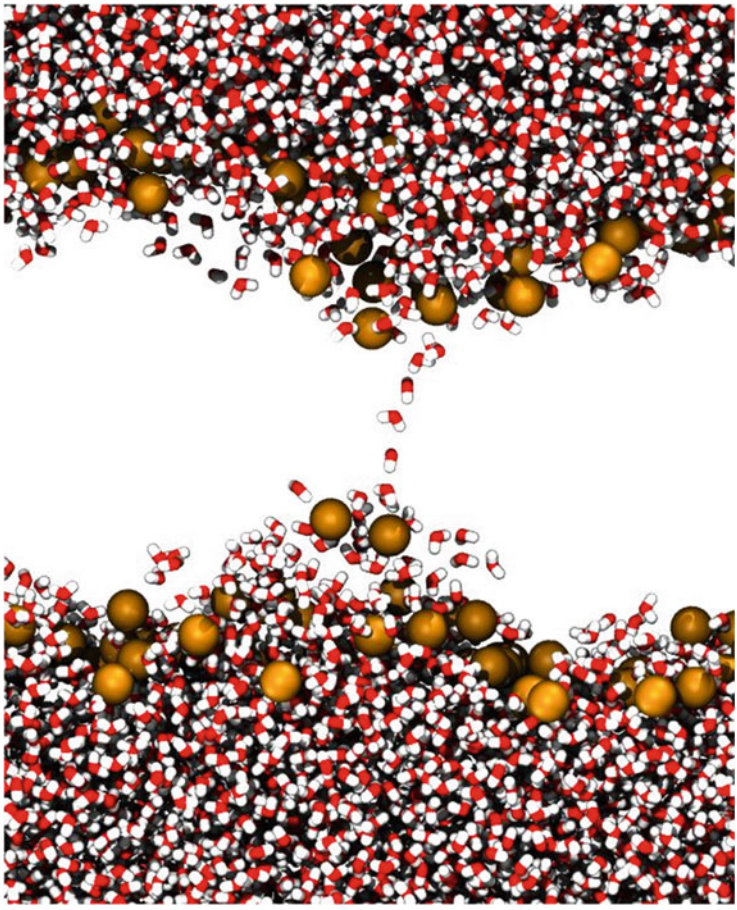

Fig. 4.10 Water bridge in POPC bilayer formed after application of an external electric field. Water molecules are *red* (oxygen) and *white*. Note the alignment of the water dipoles in the electric field in the low-permittivity environment of the membrane interior. The *gold spheres* are the acyl oxygens on the glycerol backbone of POPC. The phospholipid hydrocarbon tails are not shown. The simulated volume is approximately $7 \times 7 \times 10$ nm

surrounding medium, much has been learned from experimental observations of electroporation of artificial membranes of similar composition, and this body of knowledge can be used to validate the molecular models. With accumulated experience and increasing computing power, molecular simulations can iteratively become more complex and more realistic.

More and more, as molecular simulation tools are used to probe the process of electroporation more deeply, it becomes necessary to move beyond homogenous (single-phospholipid) bilayers in water; and consistently to include other lipids like phosphatidylserines, cardiolipins, sphingolipids, glycolipids, and cholesterol, and to represent a more physiological aqueous medium containing sodium, potassium, chloride, calcium, and other ions.

After the construction and stabilization of the membrane, a transmembrane electric potential must be applied. This can be done either by applying an external electric field or by creating an imbalance in the distribution of free charges on either side of the membrane. (These two methods can also be combined.)

The first method, which is simpler and is more often used, is implemented by globally applying a force vector $q\boldsymbol{E}$ to each charged atom in the system, in the direction of a specified external electric field **E**. This force vector is summed with the other force vectors acting locally on each atom at each simulation step, which updates the position and velocity of each atom in the system. The field can be applied with the same magnitude at each simulation step or the magnitude can be time varied, for example, to approximate the effect of a finite rise time for the electrical stimulus.

It is important to note that the "applied" field is only one component of the electric force experienced by any given charge in the system. In a typical phospholipid bilayer simulation, the water dipoles and the phospholipid head group dipoles reorient in a globally applied electric field (which is the field that would be felt in a vacuum at that point). This produces a counter "polarization field", so that the net electric field experienced by a particular atom or atom group, which is the sum of the vectors of the external field, the fields from nearby charges, and all of the dipole fields at that point, is considerably less than the value of the externally applied field alone.

In the second method, a charge imbalance is imposed across the membrane by placing an excess of positive ions on one side and an excess of negative ions on the other. Because molecular dynamic simulations use periodic boundary conditions to minimize edge effects in small simulation volumes, it is not possible to create an ion imbalance in a system containing a single bilayer with water on each side, since the solvent on the two sides of the bilayer is actually connected (the simulation box "wraps around" in the x-, y-, and z-directions). One way to work around this is to place two parallel bilayers in the system, so that there is an inner volume of water that is confined between the two bilayers in the direction normal to the bilayers. This inner compartment is isolated from the outer compartment, which is located on the other side of the two bilayers, as long as the membranes remain intact. Another

approach is to create a simulation with a single bilayer with a stack of water covering the bilayer on each side, followed by a slab of vacuum (or air) covering the water layer on each side. The vacuum is continuous in the z-direction and "wraps around" the water slabs, but the water on each side of the bilayer is isolated by the vacuum from the water on the other side.

4.3.4 Lipid Electropore Formation in Molecular Dynamic Simulations

Initial reports of molecular simulations of the electroporation of lipid membranes [63–65] were followed by an extension of the early results to a variety of lipid types and simulation conditions and to detailed molecular descriptions of pore creation and annihilation [59]. These processes are similar for many types of amphiphilic phospholipid bilayers, for heterogeneous and asymmetric bilayers containing anionic phospholipids, and even for "membranes" composed of octane [66] or vacuum [67]. The common sequence of events for all of these systems is the intrusion of interfacial water into the low-permittivity environment of the membrane interior and the stabilization of membrane-spanning water columns by the applied electric field [68]. For phospholipid bilayers the construction of these water bridges is accompanied by the energy-minimizing reorganization of the head groups along the field-stabilized water columns to form the wall of a lipid pore.

Although the construction of an electropore, once initiated, is deterministic and driven by the electric field, the first step—the appearance of the first stack of two or three water molecules climbing away from the interface into the membrane interior—is a random event. Increasing the transmembrane potential increases the probability that a pore will form at a certain place within a certain time [59]. The statistical nature of pore initiation at the molecular scale is consistent with the stochastic pore model that is the basis of popular continuum models of electroporation, bolstering confidence that the two perspectives will someday be unified.

With model membrane systems that are more complex and more representative of living cell membranes, we will be able to see how this simple, field-driven, water-directed mechanism of lipid electropore formation is modified by a variety of factors: ions in the medium, cholesterol, regions of different lipid compositions (lipid rafts, sites of peroxidation), membrane protein–lipid boundaries, permeabilizing peptides, DMSO, detergents, cytoskeletal attachments and other mechanical constraints on lipid motion, and many others. In this way we can move from molecular-scale reconstructions of the membrane in an applied electric field to a better understanding of electropermeabilization in living cells and tissues.

4.4 Electropermeabilization

Marie-Pierre Rols, Justin Teissie, and Lluis M. Mir

Electropermeabilization using μs and ms pulses has also been termed "classical electroporation," as opposed to the nsPEF effects achieved using ns pulsed electric fields. This subchapter reviews what is known about the electropermeabilization processes of cells and tissues submitted to μs and ms electric pulses. It aims to describe the basic aspects at the membrane level (the modulation of the transmembrane potential, the way to conduct experiments) and summarizes its short- and long-term consequences at the membrane and cell levels.

4.4.1 Resting and Electro-induced Transmembrane Potentials

As already described in Sects. 4.1.1 "Cell in the Electric Field" and 4.1.2 "Induced Transmembrane Voltage," the key nonthermal effect of electric field on cells is a position-dependent change in the resting transmembrane potential difference $\Delta\Psi_o$ of the plasma membrane [69–71]. The electrically induced potential difference $\Delta\Psi_E$, which is defined as the difference between the potentials inside (Ψ_{in}) and outside (Ψ_{out}) the target cell, at a point M on the cell surface, is given by

$$\Delta\Psi_E(t) = \Psi_{in} - \Psi_{out} = g(\lambda) r E \cos(\theta_M)\left[1 - e^{\frac{-t}{\tau}}\right] \tag{4.5}$$

where t is the time after the onset of the electric pulse; g is a function that depends on the conductivities λ of the cytoplasm, the plasma membrane, and the extracellular medium; r is the radius of cell; E is the field strength; θ_M is the angle between the normal to the plasma membrane at the position M and the direction of the field; and τ is the membrane-charging time (≈1 μs in the case of eukaryotic cells in suspension in a physiologically conductive medium) [72].

For isolated spherical cells, in a conductive buffer a few microseconds after the beginning of the pulse, a steady-state potential difference is present:

$$\Delta\Psi_E = 1.5\ rE\cos\ \theta \tag{4.6}$$

The field-induced potential difference is added to the resting transmembrane potential difference:

$$\Delta\Psi = \Delta\Psi_0 + \Delta\Psi_E \tag{4.7}$$

Being dependent on the angular parameter θ, the field effect is position dependent on the cell surface. Membrane electropermeabilization is observed when the transmembrane potential reaches a critical value (between 0.2 and 0.4 V) [73]. The transmembrane potential difference of a cell exposed to an electric field is a critical parameter for successful cell permeabilization, whatever the size of cell, its shape, and its orientation. It defines the sites (location, size) where molecule uptake can take place [74–76].

4.4.2 Basics Aspects of Electropermeabilization

4.4.2.1 How to Conduct Experiments (Determination of the Experimental Protocol According to Cell Characteristics: Choice of Electrodes, of Cuvette or Petri Dish, of Pulsing Medium, of Temperature, etc.)

In most experiments, square wave electric pulses generators are used. They allow the independent control of the amplitude of the electric field and the duration of the pulse [77]. The electric pulses are delivered through a set of electrodes connected to the generator. Like the electric pulse parameters, the choice and the placement of electrodes have to be carefully selected considering the characteristics of the cells, both in the case of in vitro 2D and 3D cell cultures or of tissues in vivo [78].

The biodistribution of the local electric field is dependent on the electrode geometry and placement. The most commonly used applicators are plate, contact, and needle electrodes [79]. The plate electrodes are mostly used for attached cells grown on Petri dishes, for cells in suspension and for skin, muscles, and other superficial tissues. The tissue must be pinched between the electrodes to obtain an optimized distribution of the field effect [80]. With the contact electrodes, the penetration depth of an effective electric field is rather small and depends on the interelectrode distance. In contrast to plate electrodes, needle electrodes are invasive and have to be inserted throughout the tissue. Regardless of the kind of electrodes, the local electric field is highest around the electrode for needle and contact, whereas for plate electrodes, it decreases very rapidly outside of the electrode gap. Thus, if the cells (or the tissues) to be treated are grown on a surface that is larger than the interelectrode distance, the entire surface (or tissue) will have to be treated by successive displacements of the electrodes to cover the entire surface by the repetitive application of electric pulses [81]. Because of the structural heterogeneity of cell cultures grown at high density, especially in the case of 3D cell cultures and tissues, the electric field is difficult to determine. So the applied voltage (V) to distance between the electrode (d) ratio has to be used to describe the pulse amplitude instead of an electric field value. To this end, both V and d must be reported.

While tissues can be “simply” permeabilized by the direct application of the electric pulses through contact or needle electrodes, permeabilization of cells in culture can be conducted on different ways. The bottom of the Petri dish serves as

an electropulsation chamber. For cells in suspension, special cuvettes can be purchased but "homemade" chambers can be designed: the cells can even hold by surface tension forces between two plate electrodes if the distance between the plates is 1 or 2 mm. Alternatively, the plate electrodes can be placed directly on the bottom of the Petri dish to form a sort of open cuvette.

Another parameter that can be adjusted is the temperature. Experiments are usually performed at room temperature, but incubating the cells on ice before pulsation or during the minutes following can improve the uptake of molecules. However, for preserving cell viability and depending on the goal of the experiment, the tip is to place the cells immediately at 37 °C after the pulses [82]. In another respect, to limit the Joule effect that strongly depends on the buffer conductivity, classical culture medium can be replaced by a low ionic, iso-osmotic buffer particularly in the case of cells grown on Petri dishes. The composition of this medium is generally a 10-mM phosphate buffer pH 7.4, 250-mM sucrose (to keep the isotonicity), and 1-mM $MgCl_2$ (for preserving the cell physiology) [83].

4.4.2.2 Limits on Detection Due to the Sensitivity of the Assay Method

The first experiments to detect membrane permeabilization were performed on cell populations by measuring conductivity changes or radioactive and/or small-molecule uptake (such as sugars, trypan blue, Lucifer yellow) [84–87]. The use of fluorescent dyes allows detecting membrane permeabilization by a more convenient way. Visualization can be performed at the single-cell level using a fluorescent light microscope, while flow cytometry permits to quantify the uptake of molecules on a large number of cells [88, 89]. Quantification can be subject to artifacts as the sensitivity of the detection method highly depends on the fluorescent dye (size, fluorescent quantum yield) and on the cell autofluorescence [86]. Another very sensitive method constitutes the exposure of the cells in the presence of a toxic compound such as Ca^{2+} or bleomycin, a non-permeant cytotoxic drug at very low external concentrations [90]. Indeed, the uptake of 500 molecules is sufficient to kill the cells in culture. Interestingly, quantitative comparisons can be performed through the determination of cell viability using precise methods like the cloning efficiency approach. Consequently, the statement that a cell has been successfully permeabilized or not requires the delivery of additional information including the type of molecule used in the assay and the detection method employed (Fig. 4.11).

4.4.2.3 Effect of the Electric Field Parameters (Pulse Amplitude, Pulse Shape, Pulse Duration, Number, Polarity, and Repetition Frequency)

Permeabilization occurs only on the areas of the plasma membrane where the membrane potential difference has been brought above its critical value ($\Delta\Psi c$, close to 200–300 mV for ms pulses independently of the cell type). Membrane permeabilization is therefore controlled by the electric field strength. This means

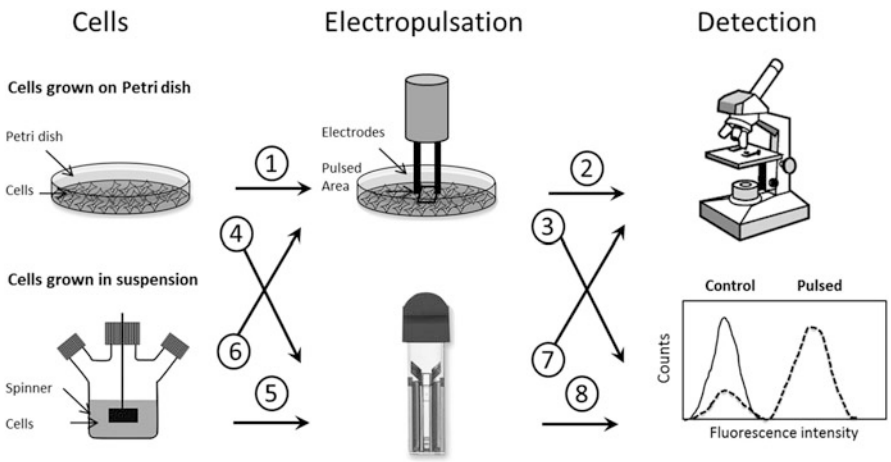

Fig. 4.11 Tips for your experiments. Cells grown in Petri dish can be directly electropermeabilized on the Petri dish by using plated electrodes (*1*). Detection and quantification of the permeabilized cells can be performed by direct counting under microscope (*2*) or by flow cytometry after careful trypsinization of the pulsed area (*3*). They can also be electropulsed in suspension on cuvettes after trypsinization (*4*). Cells grown in suspension can be electropermeabilized on cuvettes (*5*) or on "homemade" pulsation chamber by using plated electrodes (*6*). Detection of the permeabilized cells can be performed under microscope (*7*) or by flow cytometry (*8*)

that a field intensity E larger than a critical value, Ep, needed to induce $\Delta\Psi c$ must be applied. Ep is dependent on the size of the target cells (Eqs. 4.5 and 4.6, above). Large cells are more sensitive than the small ones. Electric field values have to be adapted to each cell line in order to avoid affecting their viability. The field strength triggers permeabilization: when $E > Ep$, it controls the area of the cell surface, which is affected. From Eqs. 4.5 and 4.6, it is clear that for field intensities close to Ep, permeabilization is only present for θ values close to 0 or π. Under that condition, only the localized parts of the membrane surface facing the electrodes are affected. However, within these permeabilized cell regions, the local level of permeabilization is controlled by the number and the duration of the electric pulses. So, membrane permeabilization only occurs for electric field values E higher than the threshold value Ep, whatever the number and duration of electric pulses. Increasing E, above Ep, leads to increase in the extent of membrane area where permeabilization takes place, and in that specific area, the extent efficacy of permeabilization is determined by the number and duration of electric pulses [75, 86].

As it will be described in Chap. 5, "Electrotransfer Mechanism for Drug and Gene and Delivery," permeabilization can be improved by changing the polarity of the electric pulses and the frequency.

4.4.3 Electropermeabilization, a Fast, Transient, and Localized Process

4.4.3.1 Available Direct Methods for Cell Electropermeabilization Measurement: Optical Imaging, Atomic Force Microscopy, Nuclear Magnetic Resonance, Electron Microscopy, and Coherent Anti-Stokes Raman Scattering

These methods are not based on the transport of substance across the electropermeabilized membranes. Video microscopy allows visualization of the process at the single-cell level. In addition to fluorescence microscopy, phase contrast can be used to detect cell swelling or bleb formation that can appear following cell electropermeabilization or to detect lipid loss inducing several membrane alterations (pore, tubule, and vesicle formation) as observed on giant unilamellar vesicles [91]. The need of data recorded directly at the single-cell level without any staining or preparation is of great interest. In this context, the effects of membrane destabilization resulting in permeabilization to small molecules can be addressed by performing direct quantitative biophysical measurements using atomic force microscopy (AFM) [92, 93] and nuclear magnetic resonance (NMR) [94, 95] or phase-contrast and coherent anti-Stokes Raman scattering (CARS) microscopy as relevant optical approaches to gain insight into membrane changes [96]. The resolution of these techniques is quite poor compared to electron microscopy where ultrastructural modifications of membranes and cell organelle can be detected (but EM requires fixation of the cells).

4.4.3.2 Visualization of the Uptake of Molecules and Its Dependence to the Molecule Properties

Membrane electropermeabilization is a fast and localized process. Propidium iodide, a fluorescent non-permeant molecule, can be used as a probe for small molecules ($\leq$4 kDa). Its uptake in the cytoplasm is a fast process that can be detected during and after the application of electric pulses. In less than 1 min, it appears at the nucleus level [41, 89]. PI does not allow for quantitative measurements as its fluorescence depends on its molecular environment. As reported by Silve and Mir, there is an inverse relationship between the size and number of molecules internalized using identical cells and pulse parameters [97].

As described in Sect. 4.4.2.2, fluorescent dyes allow visualizing membrane permeabilization on a convenient way. Visualization can be performed at the single-cell level under fluorescent microscopes but can be subject to artifacts as the sensitivity of the detection depends on the molecule properties (size, charge) and the way the experiments are conducted (microscope adjustment).

4.4.3.3 Direct and Localized Access to the Cytoplasm

Exchange across the pulsed cell membrane is not homogeneous on the whole-cell membrane. It occurs on the two caps at the cell surface facing the electrodes. Uptake is asymmetrical. Using PI (which has a direct access to the cytoplasm after the cell membrane permeabilization), it has been shown that uptake is more pronounced at the anode-facing side of cells than at the cathode one, i.e., in the hyperpolarized area than in the depolarized one, in agreement with above theoretical considerations and Eqs. 4.5 and 4.6 [98]. As will be described in Chap. 5 "Electrotransfer Mechanism for Drug and Gene and Delivery," large molecules such as plasmid DNA are internalized in the cells by more complex mechanisms.

4.4.3.4 Resealing (Assays, Temperature, Energy, Cytoskeleton)

Once electropermeabilized, cells can stay permeable after switching off the pulse generator. Lifetime of permeabilization can be assayed by adding fluorescent dyes at various times following the pulses. If the cell membrane is still permeable, then the cell will be fluorescent. One key actor of that phenomenon is the cytoskeleton [99]. Lipid vesicles can be permeabilized but resealing occurs in less than 1 s. Cells pretreated with drugs that affect the cytoskeleton can be permeabilized by electric pulses but have a very fast resealing rates. Resealing varies from a few seconds (when cells are put at 37 °C just after pulsation) to several hours (when cells are maintained on ice) according to the experimental conditions (temperature and pulse parameters). However, one has to take into account that viability can be affected since ATP release will occur [100].

4.4.3.5 Short- and Long-Term Membrane Permeabilization and Cell Alterations (Lipids and Proteins and Cytoskeleton)

Mechanisms at the molecular level are detected after the pulse application. These data could be correlated with the transient reorientation of the phospholipid head group reported on mammalian cells and lipid bilayers by ^{31}P NMR as well as a field pulse correlated phosphatidylcholine flip/flop restricted to the permeabilized regions [101]. Transient phosphatidylcholine flip/flop in nucleated mammalian cells appears as a direct effect of electric fields and not a secondary one as reported in red blood cells.

Changes in living cell membrane properties due to EP process can be assessed by AFM in real time. AFM can be used for the quantification of the destabilization process in terms of elasticity. Stiffness data gives new insight of the permeabilization process. Data obtained on fixed cells give access to information at a specific moment of the EP phenomenon. Topological images of membrane on living cells at high resolution can be recorded and give direct visual information

about EP effect. Moreover, AFM senses an effect of EP that is shorter than plasma membrane permeabilization and that is linked to cortical actin destabilized by electric pulses [92].

Altogether, these short- or long-term membrane alterations will have direct consequences on molecule uptake as will be described in the next chapter.

4.4.4 Cells Responses: From 1D (Single-Cell Analysis) to 3D Studies (Using 3D Cell Aggregates)

4.4.4.1 Single Cells: Endocytosis-Like Processes Are Present

Electric pulses alter the plasma membrane permeability leading to the uptake of molecules that can enter the cells. The membrane structures driving the permeability are thought to result from lipid mismatches (aqueous conductive defects), allowing small molecules to have a direct access to the cytoplasm. Although these membrane defects are present for several minutes and are associated to its passage, DNA has not a direct access and accumulates at the membrane as will be described in chapter 5. DNA internalization thus occurs after membrane resealing and involves the passage of large-sized DNA aggregates [102]. Endocytosis-like process takes place as it is the case for many viral or chemical vectors. Macropinocytosis was earlier reported for the delivery of proteins, when added during the minutes following pulse delivery. One has to notice that electric pulses, applied under conditions that do not lead to "classical" permeabilization, can enhance natural endocytosis pathways [103, 104].

4.4.4.2 Monolayers: A Fusogenic State Is Triggered

One direct consequence of membrane permeabilization, which may occur when cells are into contact, as it is the case of cells growing in Petri dishes up to confluence or artificially brought into contact, is membrane fusion [105, 106]. Fusion can also be obtained when cells submitted to electric pulses are brought into contact by centrifugation or filtration. This fusogenic state can also be observed in vivo in the liver [107].

4.4.4.3 Spheroids: The Use of 3D Models of Cell Culture as Relevant Tools to Access In Vivo Electropermeabilization Constraints (Mainly Cell Density and Contact)

Even if the high majority of studies underlying molecule transfer by electric fields have been performed on 2D cell culture in Petri dish or in cells cultured in suspension, 3D multicellular spheroids represent a nice, relevant, cheap, easy-to-

handle in vitro model to gain understanding of in vivo tissue electropermeabilization and electrogene delivery processes [108] and optimization of electromediated drug delivery protocols [109]. Small-molecule uptake is present but spatially heterogeneous within a 3D multicellular spheroid after electroporation, with a progressive decrease from peripheral to interior cells [110]. This can be due to the increased diffusional lag time required for solutes to penetrate homogeneously throughout the extracellular space within spheroid before applying electric field, to limited extracellular reservoir of molecules surrounding densely packed cells, to local perturbation of the electric field due to heterogeneous high-density multicellular environment electrical properties, and finally to a position-dependent variation in cell size as reported in Sect. 4.1.2.2 "Numerical Computation."

Moreover, in the case of large molecules as plasmid DNA, spheroids allow showing that electrophoresis, and not tissue deformation or electroosmosis, is the driving force for interstitial transport. At the opposite of cells in 2D cultures, only cells on one side of the outer leaflet expressed the reporter gene [111]. This low expression is in fair agreement with in vivo experiments on tumors [112]. Close contacts between cells and extracellular matrix may act as a physical barrier that limits/prevents uniform DNA distribution and explain the absence of gene expression in the inner region of spheroid [113]. The limited access of plasmid DNA to central region of spheroid remains a significant barrier to efficient gene delivery in tissue. In addition, three-dimensional reconstructed human connective tissue model could become a useful tool to study skin electrotransfer mechanisms and would help improve electrogene therapy approaches such as the systemic delivery of therapeutic proteins and DNA vaccination [114].

4.5 Basic Properties of Nanoelectropores and Their Impact on Cell Function

Andrei G. Pakhomov

4.5.1 Nanoelectropore Definition

High-amplitude electric pulses weaken the barrier function of the cell membrane, making it more "leaky." As a result, solutes that were unable or had a limited ability to cross the membrane move more freely down their electrochemical gradients. For example, the concentration of free Ca^{2+} inside biological cells is roughly 10^5 times lower than in the outside medium, so opening of membrane pores permeable to Ca^{2+}

will cause its transmembrane flow from outside into the cytosol. The negative charge inside the cell will assist the flow of positively charged Ca^{2+}.

Likewise, electropermeabilized membranes may allow the transmembrane flow of anions and neutral solutes, small molecules (such as ATP and dyes like YO-PRO-1), and water. The size of pores puts a limit on which species can cross the membrane; therefore testing different species may be the first step to estimate the size of pores. In the first approximation, the size of pores formed by electroporation depends on the electric pulse amplitude and duration. Once pores are created, the continued application of external voltage leads to pore expansion. That is why "long" (micro- and millisecond duration) pulses may open pores permeable to larger solutes than pores opened by shorter nanosecond-duration electric pulses (nsEP). The diameter of pores formed by the conventional electroporation using micro- and millisecond pulses is estimated to fall within 1–100-nm range [115–117]. The principal primary effect of nsEP, as demonstrated by both in silico models [13, 118–120] and live cell measurements, is the formation of small pores having the diameter on the order of 1–1.5 nm [43, 121–123]. Consequently, the term "nanoelectroporation" has established a dual meaning as (1) application of nanosecond-duration pulses for electroporation and other bioeffects and (2) a treatment that causes preferential formation of the smallest membrane pores (also called "nanopores" or "nanoelectropores"). The size-based definition is more common and will be used below in this chapter. With that said, application of high-voltage nsEP is perhaps the most common way to create nanometer-sized pores, so the two definitions of "nanoelectropore" are not necessarily contradictory.

At present, there is no consensus as to whether nanoelectropores are discrete membrane structures with long lifetime; or they are transient structures which randomly emerge and expire in membranes disrupted by electric pulses; or the term "nanopores" is just a convenient way to characterize the selective leakiness of electropermeabilized membranes to certain solutes. Although the exact nature of electropermeabilization of membranes by nsEP is not fully understood, the concept of the formation of long-lived nanopores is consistent with most if not all available experimental data.

4.5.2 How to Make Nanoelectropores in Live Cells

As mentioned above, exposure of living cells to high-voltage nsEP is a common way to open long-lived nanopores, but other approaches may be employed as well. In principle, nanopores may be the first stage of larger pore formation by conventional electroporation [115, 124], and stable nanometer-sized pores were also reported to form by gradual shrinking of larger electropores [115–117]. Some chemical and physical factors cause membrane perturbations and bioeffects similar to nsEP, which could potentially be explained by nanopore formation [125–127]. Finally, prolonged holding of cell membrane at marginally permeabilizing transmembrane potentials (~200 mV) using whole-cell patch clamp increases the

membrane conductance by opening nanometer-sized pores [128]. The sameness of these pores to those opened by nsEP has yet to be proven, but there are no reasons to suspect that they are different.

While nanopores are not a unique effect of nsEP, stimulation by nsEP is a convenient way to create nanopores to study their properties and impact on cells. With longer electric pulses ("conventional electroporation"), it is problematic to identify nanopores and explore their properties in heterogeneous pore populations. The time interval until larger pores shrink is variable and uncertain, and profound consequences of large pore opening can mask nanopore effects. On the contrary, nsEP forms a relatively uniform population of stable nanopores, thereby offering an opportunity to explore nanopore properties and their impact on cells. At the same time, anticipated findings with nsEP-opened nanopores will likely broadly apply to nanopores created by longer pulses and nonelectrical stimuli as well.

4.5.3 Detection of Nanoelectropores and Their Properties

Contrary to larger pores formed by the conventional electroporation, nanopores exert complex behaviors that are traditionally thought to be unique for protein ion channels [122, 129]. Nanopores are inward rectifying, voltage and current sensitive, and ion selective; they can remain open for minutes while oscillating between electrically silent and open states. Nanopores appear adequately equipped to replace or complement a number of transmembrane ion transport functions that are now ascribed to classic ion channels. Consequently, the lasting disruption of the cell membrane barrier function impacts a wide spectrum of living cell functions.

The detection of nanopores is inherently related to their specific properties, which is why they are considered together in this chapter. We will consider nanopore detection by (1) differential uptake of fluorescent markers (dyes, reporter ions, or molecules), (2) changes of the cell volume due to water uptake or loss, and (3) direct measuring of membrane current using patch clamp.

4.5.3.1 Fluorescent Dye Uptake Techniques

The cell membrane integrity can be routinely tested by measuring the transmembrane flow of substances which do not penetrate through the intact membrane. DNA stains like propidium iodide and YO-PRO-1 are essentially nonfluorescent in extracellular media, but show bright fluorescence upon binding to nucleic acids (DNA in particular) inside the cell. The intact cell membrane is essentially impermeable to these dyes, and adding them to the external medium does not change the fluorescence of cells. However, if the membrane barrier function is compromised, these dyes can enter the cell and bind to DNA and RNA, which is detected by an increase in cell fluorescence (Fig. 4.12).

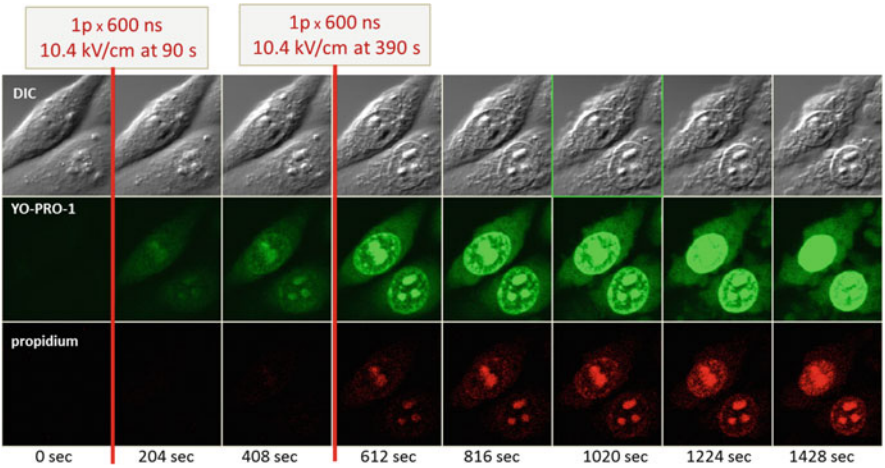

Fig. 4.12 Detection of membrane nanoporation by the entry of fluorescent dyes YO-PRO-1 (*center row*) and propidium (*bottom*). Shown are sequential images of CHO cell images subjected to two treatments with nsEP, at 90 and 390 s into the experiment (a single 600-ns pulse at 10.4 kV/cm) . The *top row* shows the cells as seen with differential interference contrast (DIC) optics. The time from the start of the experiment is indicated under the images. Note that the entry of YO-PRO-1 after the first nsEP treatment was not accompanied by any detectable entry of propidium

(Of note, traditionally most publications abbreviate propidium iodide to "PI" and discuss the PI uptake by electroporated cells. However, it should be taken into account that in water, PI dissociates into propidium cation and iodide anion; it is the propidium cation that penetrates the membrane and causes fluorescence changes, not the entire PI molecule. This difference is particularly important when talking about the pore size. Therefore, below we will use a more accurate term "propidium uptake" (Pr uptake). The YO-PRO-1 dye actually is supplied and added to solutions as an iodide salt (which also dissociates), so referring to YO-PRO-1 uptake is correct.)

Pr fluorescence is commonly used to detect dead cells and cells with membrane disrupted by conventional electroporation. However, the entry of Pr through nanopores is relatively modest, so when fluorescence detectors are tuned to the detection of dead cells, the Pr entry through nanopores can remain undetected. In Fig. 4.12 (bottom), there is no detectable Pr uptake after a single 600-ns pulse at 10.4 kV/cm, whereas the application of the second pulse triggers the uptake. In early studies with nsEP, this peculiarity was erroneously interpreted as a lack of damage to the cell membrane by nsEP. More detailed later studies suggested that it is the small size of membrane pores that limits Pr uptake, whereas the fact of membrane permeabilization can be readily demonstrated by other methods, such YO-PRO-1 uptake. The molecule of YO-PRO-1 is smaller and its passage through nanopores is not restricted to such a degree as for Pr. In Fig. 4.12 (center row), the entry of YO-PRO-1 is obvious even after the first nsEP treatment.

Even more sensitive detection of nanoporation is based on the uptake of still smaller solutes, such as Ca^{2+} and Tl^{+} ions [123, 130, 131]. For Tl^{+} uptake detection, cells are preloaded with a Tl^{+}-sensitive dye FluxOR® (Invitrogen, Eugene, OR) and placed in a medium with Tl^{+} added (of note, Tl^{+} precipitates with Cl^{-}, so the medium should be properly formulated to exclude Cl^{-} or minimize its concentration). Since Tl^{+} cation is not found in living cells in any appreciable amount, the fluorescent method of detection of Tl^{+} entry is highly sensitive and always reflects Tl^{+} entry through the plasma membrane (in contrast to Ca^{2+} detection, since Ca^{2+} can come into the cytosol from intracellular depots). Intact lipid membrane is impermeable to Tl^{+}, but this ion can potentially enter the cell via "classic" voltage-gated K^{+}-selective ion channels and various nonspecific cation channels. The differentiation between Tl^{+} entry through endogenous channels and through nsEP-opened nanopores may be challenging and requires careful selection of the cell type and/or pharmacological inhibition of the channels.

Most of living cells at rest have about 100 nM of free Ca^{2+} in the cytosol, which is about 10,000-fold less than in extracellular fluids. Thanks to this naturally high transmembrane Ca^{2+} gradient, opening of nanopores quickly leads to an increase in the intracellular Ca^{2+} concentration, which can be detected by various Ca^{2+}-sensitive fluorescent dyes. Ca^{2+} detection methods are among the best developed, most affordable, and most reliable. A broad selection of Ca^{2+}-sensitive dyes is available, including dyes like Fura-2 for fast quantitative measurement of Ca^{2+} concentration by ratiometric imaging. Detection of nanopores by Ca^{2+} uptake is almost as sensitive as with Tl^{+}, but more caveats need to be taken into account. First, the resting level of Ca^{2+} in the cytosol can transiently increase into the millimolar range when cells are activated. Second, Ca^{2+} can come into cells through voltage-gated Ca^{2+} channels and many types of other channels. Third, Ca^{2+} can enter cytosol not only from the outside but also from intracellular stores, such as the endoplasmic reticulum (ER). Finally, cells express multiple mechanisms that can either amplify weak Ca^{2+} signals by opening Ca^{2+} channels in both the plasma membrane and the ER or reduce and terminate Ca^{2+} increase by actively pumping Ca^{2+} out of the cytosol. While it is tempting to use ratiometric Ca^{2+} imaging to quantify its inflow through the nanoporated cell membrane (in order to measure the nanopore transport), the impact of biological factors may be difficult to rule out. This is the reason why Ca^{2+} imaging is more often employed to study the downstream consequences of nanopore formation rather than for quantitation of the transport.

The dye and ion uptake methods described above are only indicative of the pore size and, as a rule, are more useful for comparison of different treatment conditions rather than for accurate pore-size measurements. Smaller pores will restrict the flow of larger molecules to a greater extent than the flow of smaller ones. For example, if a 100-ns pulse triggers high uptake of Tl^{+} (a small solute) and little uptake of Pr (a relatively large solute), whereas a 10-ms pulse triggers high uptake of both Tl^{+} and Pr, such data indicate that pores opened by the 10-ms pulse are larger. Under certain conditions, the ratio of the entry of two solutes of different molecular size can be used for a more definitive estimation of pore size [43].

4.5.3.2 Changes of the Cell Volume Due to Water Uptake or Loss

Typically, permeabilization of cell membrane leads to cell swelling. The mechanism of cell volume changes is reasonably well understood and results from Donnan-type colloid osmotic pressure [116, 122, 132]. It should be emphasized that the colloid osmotic force depends on the molecular size of solutes rather than on the overall osmolarity of the medium.

The mechanism of the colloid osmotic effect is explained in Fig. 4.13. The simplified scenario presented in this figure disregards any active volume control mechanisms [132, 133] and considers only three types of solutes which differ in the molecular size. In the top row (before poration), the extracellular buffer contains only small molecules, whereas inside the cell, there are both large and small molecules. The osmolality inside and outside the cell is made the same (300 mOsm/kg), which results solely from small solutes outside and from both small and large solutes inside (250 and 50 mOsm/kg, respectively). We assume that electroporation (right panel) makes the membrane permeable to the small solutes but not to the large ones. Then, the small solutes enter the cell up to the same concentration as outside and their osmolality inside reaches 300 mOsm/kg (the cell volume is assumed to be negligible compared to the outside solution volume). Large solutes remain trapped in the cell, still contributing their 50 mOsm/kg. Hence the total osmolality inside will be 350 mOsm/kg (more than outside), causing water entry and cell swelling. In real life, even a small increase in osmolality is offset by water uptake and continual swelling (so that the maximum osmolality stays just above 300 mOsm/kg).

Alternatively, if we initially have only large (pore-impermeable) solutes outside the cell, the electroporation leads to the loss of small intracellular solutes which is not compensated by any uptake (Fig. 4.13, middle row). The osmolality within the cell drops to 50 mOsm/kg (from large solutes only), and water leaves the cell, causing its shrinking. Finally, an extracellular solute which is marginally permeable through the pores (comes in very slowly, e.g., because it can utilize just a small fraction of pores) may cause biphasic volume changes, namely, initial shrinking followed by swelling (bottom row).

Thus, the direction of volume changes (shrinking or swelling) after the electroporation depends on whether the outside solute(s) can or cannot enter the cell through the pores. One can put molecules of different sizes into the outside solution to test if they inhibit swelling in electroporated cells. When a solute blocks swelling (and converts it into shrinking), it indicates that pores are smaller than the molecule of this solute.

This approach was employed for measuring nanopore size, by using differently sized neutral sugars and different polyethylene glycols to “calibrate” the pore size by blocking swelling [121]. This method was remarkably sensitive, e.g., it readily distinguished between the effects of adonitol and mannitol, the molecules which have the same cross section and differ just by a single carbon alcohol group. This study established that cell volume changes after the exposure to either 60- or 600-ns

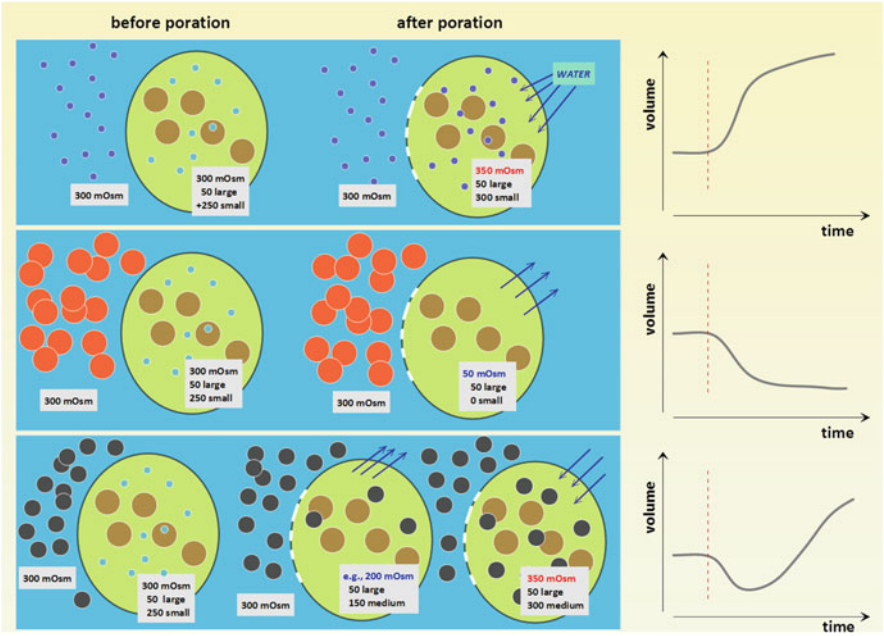

Fig. 4.13 A simplified schematic explaining the colloid osmotic mechanism of cell swelling or shrinking after membrane permeabilization. Smaller, intermediate, and larger solutes are depicted by different size circles. Three rows represent three different scenarios depending on the size of solutes in the extracellular medium. The scenarios are with a small solute which easily passes the electroporated membrane (*top*), with a large solute that cannot pass the electroporated membrane (*center*), and with an intermediate-sized solute with slow or limited pore permeability (*bottom*). The initial osmolality inside and outside the cell is the same for all scenarios (300 mOsm/kg). The intracellular osmolality (before poration) is produced by large, pore-impermeable solutes (50 mOsm/kg) and small, pore-permeable solutes (250 mOsm/kg). In the bottom row, the cell is shown before poration and early and late after the poration. See text for more details

pulses are determined by pores smaller than 0.9 nm in diameter, which is arguably the most accurate to date assessment on nanopore size. However, there is a small fraction of Pr-permeable (larger) pores, which would allow Pr entry, but have little impact on cell volume. The study also suggested that the pore diameter may increase with more intense nsEP treatments.

4.5.3.3 Direct Measuring of Membrane Current Using Patch Clamp

Once the cell membrane is permeabilized, its electrical conductance increases. This change is most reliably and quantitatively measured using the whole-cell configuration of the patch clamp method [134]. To date, electrophysiological

measurements proved more sensitive for the detection of nanopores than any fluorescent dye detection. With a single pulse of either 60- or 600-ns duration and using different pulse voltages, the extent of membrane permeabilization was shown to be proportional to the absorbed dose, with the threshold at about 10 mJ/g [135]. Sample heating at this dose is less than 0.01 °C, which shows that membrane electropermeabilization is a nonthermal effect.

The electrical conductance of nanopores is dependent on the membrane potential. The maximum conductance increase occurs at the most negative potentials and corresponds to the maximum inward current. Such differential enhancement of the inward current, or inward rectification, proved to be a hallmark feature of nanopores and distinguishes them from larger, propidium-permeable pores (which show a linear current–voltage dependence). We found that cells which display inward rectification after nsEP exposure remain completely or largely impermeable to propidium, whereas the onset of the propidium uptake marks the reduction and subsequent loss of the inward rectification [129].

Numerous experiments performed to date suggest that the inward rectification is an intrinsic and universal property of nanopores, which also points to their functional and structural asymmetry. The induction of inward rectification can be used as a nanopore "signature," i.e., as an indirect but reliable and sensitive sign of nanopore formation. However, it may not be easy to distinguish nanopores from classic ion channels which may also display inward-rectifying properties (e.g., [136, 137]).

Other remarkable features of nanopores include their extended lifetime (minutes), the sensitivity to the electric current, and ion selectivity [122, 138]. Among various pharmacological agents that block ion channels and were tested for blocking nanopores, only lanthanide ions (Gd^{3+} and La^{3+}) inhibited nanopore currents, probably by restructuring of the lipid bilayer [122, 139, 140].

4.5.4 Impact of Nanopore Formation on Cell Physiology

Long-lasting disruption of the plasma membrane barrier function expectedly affects many if not all physiological processes in living cells. Therefore, it is usually not productive to explore the impact of nanopores on a certain intracellular structure in isolation; instead, one should look at mechanisms and pathways which result in biochemical, physiological, and morphological effects.

In simple terms, bioeffects of nanopore formation can be divided into physiological and pathological. Physiological effects usually are associated with (1) depolarization of the membrane and activation of voltage-gated Na^+ and Ca^{2+} channels and/or (2) Ca^{2+} entry into the cytosol through nanopores. In both cases, nanopore formation leads to an increase of the cytosolic Ca^{2+} level.

This increase is perhaps the most consequential effect of nanopore formation. The resting Ca^{2+} concentration in most cells is held tightly at about 100 nM, and its changes (increases) serve as a versatile and universal signal for activation of Ca^{2+}-dependent cascades. Depending on the cell type and physiology, as well as on the amplitude and timing of Ca^{2+} transients, they may lead to such diverse effects as cell differentiation or division, cytoskeleton rearrangements, endo- and exocytosis, synthesis and release of neuromediators, activation of immune cells, and apoptotic or necrotic cell death [141]. Ca^{2+} entry through nanopores mimics Ca^{2+} signaling that would normally originate from the activation of membrane receptors and channels and may lead to similar downstream effects. Among the first downstream effects are the amplification of the Ca^{2+} signal by calcium-induced calcium release (CICR) [130, 131] and activation of the phosphoinositide signaling cascade [142, 143]. Nanopore formation by nsEP stimulation may be a unique approach for nonchemical activation of Ca^{2+} signaling in various types of cells, including cells that have no voltage-sensitive membrane channels. It has been proposed earlier to employ nsEP for heart pacing [128] and stimulation of catecholamine release [130, 138], but better understanding of nsEP effects may open the way for numerous other applications.

However, if nanopores are too numerous, flooding of cells with Ca^{2+} may become the primary cause of cell death. Ca^{2+} signaling is critically involved, in many ways, in both the initiation and effectuation of the cell death (see [144] for a review and other chapters of this book). Damaged cells develop necrotic blebbing, swelling, cytoplasm granulation, destruction of the cytoskeleton, shrinkage of the nuclei (pyknosis), and other pathological signs. While nanoporation can lead to either necrotic or apoptotic cell death [145–150], the increased Ca^{2+} facilitates the early necrosis and thereby decreases the cell population that could potentially become apoptotic. Recently we demonstrated that Ca^{2+}-mediated necrosis results from a delayed, abrupt, irreversible, and osmotically independent expansion of pores in the cell membrane [148].

Even with lower levels of ambient Ca^{2+}, the disruption of the membrane barrier function by nanopore formation may culminate in cell death. In this case, the primary cause of necrosis is the persistent plasma membrane permeabilization to small solutes (<1 nm). As described above, it results in the osmotic imbalance, water uptake, cell swelling, and cell membrane rupture. When the uptake of water is blocked by an iso-osmotic addition of a pore-impermeable solute such as sucrose [121], cells are rescued from the necrotic death, but nonetheless die later on by apoptosis [149]. However, the cause of the apoptosis in cells rescued from the necrosis is not fully understood. The cell death mechanisms and pathways resulting from nanopore formation are discussed in more details in other chapters of this book. For a more detailed analysis of nanopore properties, impact on cell physiology, and their hypothetical structure, please see a specialized review [122].

4.6 The Cytoskeleton as Target: Electromanipulation of Sensing at the Plant Cell Membrane

Peter Nick and Wolfgang Frey

Electromanipulation by pulsed electric fields can induce very specific and sometimes surprising, cellular effects. In this context, the current chapter wants to transport two main ideas: (1) The cellular effect is not determined by physics alone, but decisively shaped by cell biology. (2) The cellular effect is intimately linked with the cytoskeleton, and the specific differences in the electrically induced responses of animal and plant cells have to be seen in the context of qualitative differences in cytoskeletal functions. This chapter will therefore first survey the structural features of the plant cytoskeleton and then explore the different cellular functions conveyed by these plant-specific cytoskeletal arrays. Whereas the cytoskeleton in animal cells has been mostly discussed with respect to its structural and architectural role, the plant cytoskeleton seems to be rather of a sensory nature. It is this sensory function that renders the plant cytoskeleton a versatile and rewarding target for bioelectrical manipulation. Since plant cells are immobile and stabilized by a cell wall, the architectural function of the cytoskeleton has become partially obsolete. However, the tensegral organization of the cytoskeleton cannot only be used to confer structural organization; it can simultaneously be used as integrative sensory structure. This sensory function of the cytoskeleton has become dominant in plant cells and provides the conceptual framework to understand the effect of electromanipulation on the membrane-associated cytoskeleton, and the physiological functions conveyed by this membrane–cytoskeletal signaling hub with focus on volume control and programmed cell death/apoptosis. We propose a role for a membrane-associated, highly dynamic population of actin as a sensor for membrane integrity and a primary target for electromanipulation.

4.6.1 The Cytoskeleton as Central Switch for Plant Cells

Similar to their animal counterparts, plant cells can be specifically manipulated by bioelectrical treatments. However, the response of plant cells shows certain characteristics that can only be understood, when the plant-specific peculiarities of cellular structure and function are considered.

Although it is important to describe the biophysics behind these effects, a mere reduction of the phenomena to physics will fail to explain most of the biological effects. Cells are not passive targets of physical manipulation, but they actively *respond* to this physical manipulation by specific cellular events that are integrated into a biological context. This subchapter is motivated by the idea that electric

manipulation will be *actively* perceived as *signal* that conveys *information* and therefore will elicit in the receiver cell an *active response*. When we understand the *biological context* of this *active response*, we will be able to design smarter and more specific strategies to evoke the cellular effects we desire to achieve. This subchapter will attempt to illustrate this mission using electromanipulation of the plant cytoskeleton as a proof of concept.

Plant cells move only rarely, and therefore this central topic of animal development does not play a role in plants. On the cellular level, plants respond to signals (such as electromanipulation) by three phenomena: (1) directional cell expansion, (2) directional cell division, and (3) patterned cell differentiation. All three phenomena are intimately linked with plant-specific arrays of the cytoskeleton.

4.6.2 Players of the Plant Cytoskeleton

In contrast to their animal counterparts, plant cells harbor only two of the cytoskeletal systems: microtubules and actin filaments. Despite intensive efforts, the third cytoskeletal system, the intermediate filaments, could never be convincingly demonstrated in plants, neither on the structural nor on the molecular level. However, microtubules and actin filaments are complemented by a structurally complex cell wall that is linked with the cytoskeleton through transmembrane connections into a tensegral network that is often termed *cell wall cytoskeletal continuum* [151].

4.6.2.1 Microtubular Arrays

During interphase, plant cells display a peculiar array of parallel microtubule bundles subtending the plasma membrane and usually oriented perpendicular with the axis of preferential cell expansion (Fig. 4.14a). These so-called *cortical microtubules* control the movement of cellulose-synthesizing enzyme complexes in the plasma membrane and thus the direction of cellulose deposition. Since cortical microtubules can reorient in response to various stimuli, they represent a tool, by which plant cells can regulate the directionality of expansion [152].

When a cell prepares for mitosis, cortical microtubules are complemented by additional arrays that are not seen during interphase. As the first event heralding the ensuing mitosis, the nucleus moves into the cell center which is nothing else than the site where later the new cross wall will be laid down. This nuclear movement is linked with a *radial microtubule* array that emanates from the nuclear surface and merges with the cortical cytoskeleton (Fig. 4.14b), tethering the nucleus to its new position. This nuclear movement sets the pace for the actual mitotic division—in tobacco cells, where the movement is delayed—due to overexpression of a plant-specific microtubule motor, cell division is delayed as well [153]. Once the nucleus has reached its final position in the cell center, the *cortical microtubules* suddenly disappear and are replaced by a broad band of microtubules around the cell equator (Fig. 4.14c). This so-called *preprophase band* predicts site and plane of the new cell plate that will be formed much later, once mitosis has been completed. The

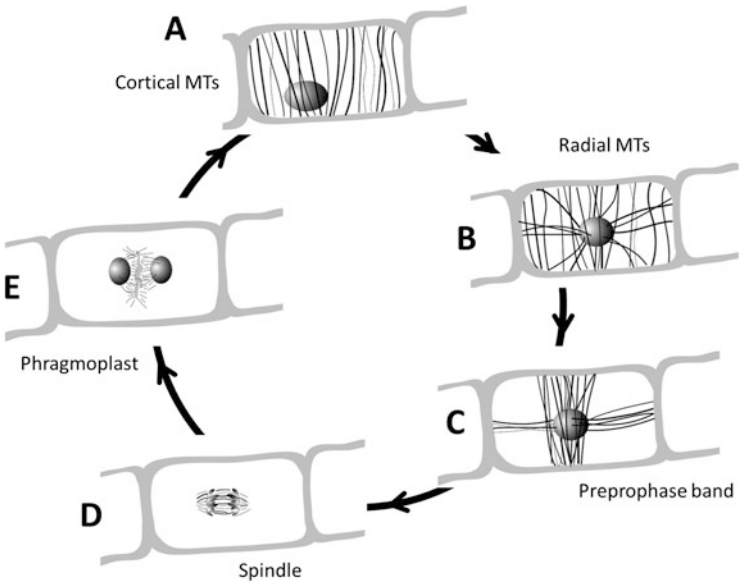

Fig. 4.14 Dynamic organization of plant microtubules during interphase and the cell cycle

preprophase band is necessary and sufficient for the correct organization of the cell plate [154]. The division *spindle* is always laid down orthogonal with the *preprophase band* [155] such that the *spindle* equator is located in the plane of the *preprophase band* (Fig. 4.14d). As soon as the chromosomes have separated, a new array of microtubules, the *phragmoplast*, appears at the site that had already been marked by the preprophase band (Fig. 4.14e). The phragmoplast controls the transport of vesicles to the periphery of the growing cell plate and consists of a double ring of interdigitating microtubules that increases in diameter with growing size of the cell plate and acts as a track for plant-specific minus-end-directed kinesins [156].

4.6.2.2 Actin Arrays

The dynamic complexity of microtubular organization is mirrored and complemented by a complex structure of the actin cytoskeleton.

During interphase, three distinct arrays can be discriminated (Fig. 4.15a): an array of transvacuolar actin cables (1), connecting a highly dynamic network of short actin filaments underneath the plasma membrane (2), and a perinuclear basket of actin bundles (3).

Unlike microtubules, the overall setup of the transvacuolar actin cables does not change much during the cell cycle, except for the fact that these cables are reoriented into a structure resembling a Maltesian cross during the premitotic nuclear migration (Fig. 4.15b). This so-called *phragmosome* seems to be interconnected with the premitotic *radial microtubules*. In contrast to the

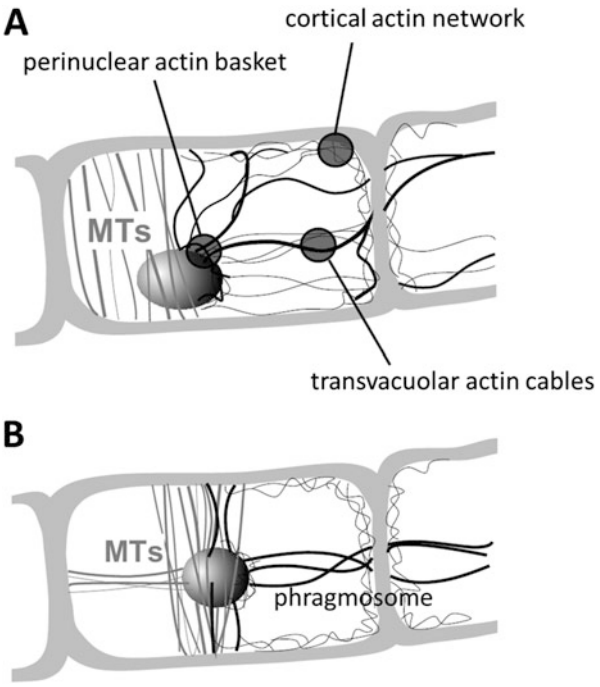

Fig. 4.15 Organization of plant actin filaments during interphase and the cell cycle

microtubular *preprophase band*, the phragmosome persists during meta- and anaphase and seems to participate in the organization of new microtubules during the formation of the phragmoplast [156]. During interphase, these transvacuolar cables are oriented parallel with the axis of cell expansion [157], and the rigidity of these transvacuolar strands as well as the degree of their bundling is under control of signals including plant hormones [158], kinase cascades [159], or light [160].

The transvacuolar cables are complemented by a fine network of highly dynamic microfilaments subtending the plasma membrane. This network had first been overlooked, because it could be rendered visible only by specific pretreatment with protein cross-linkers [161] or upon very mild fixation [160]. This peripheral meshwork was found to be linked with auxin-triggered cell elongation [162, 163], but only recently the advances of GFP-based live cell imaging made it possible to visualize this network in a consistent way such that it could be followed through the development or the response to signals [164, 165].

The perinuclear actin basket had first been discovered in dividing cells [166] and overlaps with *radial microtubules*. The actin basket and radial microtubules are cross-linked by a plant-specific minus-end-directed kinesin motor [153, 156]. The function of this actin basket is to move the nucleus to the division site. By super-resolution microscopy, we were able to see the three-dimensional topology during nuclear movement [167] and found, surprisingly, that the nucleus is not pulled by actin, but squeezed in a peristaltic manner.

4.6.2.3 Molecular Players of the Cytoskeleton

The qualitatively different organizations and functions of the plant cytoskeleton are achieved on the base of surprisingly similar building blocks: The major components tubulin and actin are almost identical between plants and animals (for a review on tubulins, see [168]; for a review on actins, see [169]). Although both proteins are encoded by gene families, whose members are differentially expressed depending on tissue, developmental stage, or signals (reviewed in [170] for actin and in [171] for tubulin), there seems to be little, if any, functional diversification of these isotypes. For instance, tubulin from animals can readily co-assemble with plant tubulin in vitro as well as in vivo. Upon microinjection into plant cells, it participates in the dynamic reactions of the host cytoskeleton in the same way as the endogenous tubulin (cell division [172, 173], cell expansion [174, 175]. From this, it can be concluded that the factors responsible for the specific organization of the plant cytoskeleton are extrinsic to actin and tubulin themselves. In fact, there is considerable diversification between plants and animals with respect to actin-binding proteins (for a review see [176]), microtubule-binding proteins (for a review see [177]), kinesin motors (for a review see [178]), and myosin motors (for a review see [179]).

4.6.2.4 The Cell Wall Cytoskeletal Continuum

In animal cells, a continuum between the cytoskeleton and the extracellular matrix is central for mechanosensing (reviewed in [180]) and employs membrane-spanning integrins that bind on their one side to proteins of the extracellular matrix containing Arg-Gly-Asp (RGD) motives and on the other side to the actin cytoskeleton (for a review see [181]). Plants seem to lack integrin homologues, but there is evidence for cytoskeletal reorganization after treatment with RGD peptides [182–184]. As a molecular basis for the plant cytoskeleton–plasma membrane–cell wall continuum, cell wall-associated kinases, arabinogalactan proteins, pectins, and cellulose synthases are discussed (for a review see [185]). The rich, but more or less circumstantial evidence for such transmembrane interactions of the cell wall and cytoskeleton has been assembled into a model of a so-called *plasmalemmal reticulum* as a third element of the plant cytoskeleton [151]. This *plasmalemmal reticulum* is probably a tensile structure and seems to participate in the control of cellulose deposition. Moreover, it was proposed to represent a manifestation of the plant version of lipid rafts.

4.6.3 The Plant Cytoskeleton as Membrane Sensor

Plants have evolved the peculiar cytoskeletal arrays described in the previous section to address specific functions. It is important to consider these functions, because they set the logical framework to understand the specific effects of electromanipulation. For all of these functions, a system property of the cytoskeleton is relevant: *tensegrity*. Microtubules are fairly stiff structures, which, with respect to their mechanic properties, can be compared to delicate glass fibers and therefore they are able to transduce compression forces [186]. In contrast, actin filaments are more flexible (mechanically comparable to silk) and therefore able to transduce traction forces. The concept of *tensegrity* became popular by the fundamental architectural work of Richard Buckminster Fuller (1895–1983). He accomplished the highest structural stability by combining a minimum of stiff and tensile elements. In fact, it is cytoskeletal *tensegrity* that shapes animal cells (for a review see [187, 188]). However, this architectural function of the cytoskeleton became mostly obsolete in plant cells due to the presence of a cell wall which is built as a composite structure with elongate load-absorbing elements (cellulose microfibers) embedded in an amorphous matrix of hemicellulose pectins and proteins.

Cellular architecture employs the tensegral principle to reach maximal mechanical stability and, simultaneously, flexibility on the basis of parsimonious use of resources and load-bearing elements. In addition, it can adapt continuously to the ever-changing conditions of growing and developing cells. This requires efficient sensing of forces and strains followed by appropriate reorganization of the tensegral building blocks. Thus, the tensegral cytoskeleton is not only a device to provide mechanical stability. It must also sense patterns of stresses and strains. This mechanical stimulation feeds back to the organization of the cytoskeleton in such a way that a stable minimum of mechanical energy is reached and continuously adjusted. It is this hidden sensory function of the tensegral cytoskeleton that dominates over architectural roles in the walled plant cells that are under continuous turgor pressure and use this pressure for regulated expansion. During plant evolution, the interphasic plant cytoskeleton was therefore shaped by selective pressures toward optimized sensing and integration at the plasma membrane. It is this sensory nature of the cytoskeleton that becomes also relevant for the response of plant cells to electromanipulation.

4.6.3.1 Cortical Microtubules and Cell Wall Texture

The parallel bundles of *cortical microtubules* are usually oriented perpendicular to the axis of preferential cell expansion. The *cortical microtubules* were found to define the biophysical properties of the yielding cell wall and thus the geometry of expansion. In cylindrical cells, where isotropic action of turgor pressure is predicted to produce only half of the strain in the longitudinal direction relative to the transverse direction, a transverse orientation of *cellulose microfibrils* maintains

the lateral reinforcement needed to drive elongation [189]. In fact, filamentous structures acting as "reinforcement mechanism" to counteract lateral expansion were predicted merely from these biophysical considerations and termed "microtubules" [190]. This prediction stimulated an intense search for such structures and 1 year later led to the discovery of "microtubules" by electron microscopy [191]. The classical model assumes that *cortical microtubules* control the orientation in which newly synthesized *cellulose microfibrils* will be laid down (reviewed in [192, 193]).

Cortical microtubules can change their orientation in response to a broad range of signals, both exogenous and endogenous, and thus allow tuning of plant morphogenesis with the challenges of the environment. Signal-dependent reorientation of microtubules will cause altered deposition of *cellulose microfibrils*, a mechanism that allows adjusting the direction in which the cell wall yields to the turgor pressure exerted by the expanding protoplast and eventually alters the proportionality of cell expansion in response to the stimulus. The cellulose-synthesizing enzyme complexes are integrated into the membrane by fusion of exocytotic vesicles and are thought to move within the fluid membrane leaving a "trace" of crystallizing cellulose. The movement of the enzyme complex will determine cellulose orientation and thus the anisotropy of the cell wall. It is the direction of this movement where cortical microtubules interfere with the mechanical anisotropy of the expanding cell wall.

The direct contact between *cortical microtubules* and newly emerging *cellulose microfibrils* has been demonstrated by electron microscopy, but is also supported by a wealth of data, where signal responses of cell expansion were preceded by a corresponding reorientation of *cortical microtubules*. As to be expected from a microtubule-based mechanism for cellulose orientation, elimination of *cortical microtubules* by inhibitors produces a progressive loss of ordered cellulose texture. The resulting loss of axiality causes lateral swelling and bulbous growth. The striking parallelism between *cortical microtubules* and newly deposited *cellulose microfibrils* led to a "monorail" model proposing that motor proteins move along *cortical microtubules* and pull cellulose synthetases [194]. A concurrent "guard-rail" model, where the crystallizing cellulose pushes the synthetase complex within microtubule-dependent protrusions, has been recently discarded, based on direct molecular evidence: Mutants with reduced cell wall integrity were affected in the microtubule-severing protein katanin [195] or in kinesin-related proteins [196]. Moreover, fluorescently tagged cellulose synthases were shown to move in tracks adjacent to the subtending cortical microtubules [197], and a cellulose synthase (CSI1) binds directly to microtubules [198].

This means that *cortical microtubules* are physically linked to proteins that span the plasma membrane and might transduce conformational changes (such as those caused by electromanipulation) directly upon the microtubular cytoskeleton.

4.6.3.2 Cortical Microtubules Act as Sensors for Abiotic Stress

As a central element of their adaptive strategy for survival, plants must integrate the signaling evoked by different stress factors into a balanced and appropriate response. Many of these stress factors can be sensed through alterations of membrane tensions: These not only include evident situations such as direct mechanic load or osmotic forces (that in the case of ionic stress are complemented by electrostatic forces) but also stimuli reporting on other environmental factors, such as gravity, wounding, wind, touch, or pathogen attack, as well as factors modulating membrane fluidity, such as cold and heat (for a review, see [199]).

As the tensegral cytoskeleton is connected with the cell wall through integrative linkers, the mechanical strains produced by cellulose microfibrils can align cortical microtubules, thus closing a self-referring circuit between the cell wall and cytoskeleton in the growing plant cell. The cell expansion reinforced in a direction perpendicular to the orientation of microtubules and microfibrils will generate forces parallel with the major strain axis [200]. These forces will then relay back through the plasma membrane upon cortical microtubules that are aligned in relation to these strains. As individual microtubules mutually compete for tubulin heterodimers and as the number of microfibrils is limited by the quantity of cellulose synthase rosettes, this regulatory circuit should follow the rules of a reaction–diffusion system [201] and therefore be capable of self-organization and patterning.

Microtubules might sense mechanical stress themselves, because during growth, they build up considerable mechanical tension [202]. This tension has to be compensated by specific proteins complexing the growing end (so-called +TIP proteins). Any mechanic stimulus at the tip will impair this compensation and the accumulated tension will be discharged as catastrophic outward bending of protofilaments. This innate mechanosensitivity makes microtubules ideal signal amplifiers in concert with other mechanosensors. In fact, microtubules were identified as interactors of stretch-activated ion channels from genetic studies in the worm *Caenorhabditis* [203] and pharmacological studies suggest that mechanosensitive calcium channels are also active in plants [204, 205]. Moreover, osmotic challenge of membranes causes assembly of cortical microtubules [206, 207]. This will stimulate phospholipase D, whose product phosphatidic acid-dependent activates a membrane-bound NADPH oxidase, producing an oxidative burst as a trigger for plant adaptation to drought stress [208].

Cortical microtubules have therefore emerged as important components of a signaling hub at the membrane of plant cells that is able to sense and process different stress signals into different and specific signatures [209].

4.6.3.3 Cortical Actin Filaments Act as Sensors of Membrane Integrity

Plant actin is essential for intracellular transport of various cargoes such as peroxisomes [210], chloroplasts [211], mitochondria [212], or Golgi vesicles [213]. Also, the active transport of plasmid DNA after electrotransfer is accomplished by the actin cytoskeleton [214]. Transvacuolar actin cables structure transvacuolar cytoplasmic strands [215] and drive the premitotic migration of the plant nucleus [153, 156]. The function of the dynamic actin network subtending the plasma membrane has remained enigmatic, however. The cortical actin net seems to be physically interconnected with the distal ends of the transvacuolar cables that on their proximal ends are linked with the perinuclear actin basket. The bundling of cortical actin filaments can be modulated by signals such as the plant hormone auxin [160, 163], and this will feed back on the cellular sensitivity to auxin [216], leading to the concept of an actin–auxin oscillator [217]:

Auxin regulates actin organization [165] by controlling actin dynamics through auxin-dependent differential membrane association of actin depolymerization factor 2 [167]. Actin, in turn, regulates auxin transport [218] constituting a self-referring oscillating circuit. This circuit oscillates with a period of around 20 min and underlies the regulation of cell expansion and cell division by auxin. Any disturbance of membrane integrity will impact on these oscillations and result in a dissociation of actin from the membrane and a contraction of the transvacuolar cables toward the nucleus.

This remodeling of actin is usually followed by programmed cell death. Similar to apoptosis of animal cells, programmed cell death in plants fulfills important functions for genetic integrity and plant survival. In particular, it is a central feature of immunity against so-called biotrophic pathogens (for a review, see [219]). This specialized group of pathogens does not kill the host cell, but invades them after manipulating basal immunity and reprogramming the host cell to deliver nutrients, thus turning its victim into a kind of defenseless zombie. The most efficient strategy to encounter these pathogens is to activate programmed cell death. Thus, the infected cell will commit suicide for the sake of its healthy neighbors. Prior to its final sacrifice, the reprogrammed cell activates the accumulation of antimicrobial toxins in the vacuole. The controlled breakdown of the vacuole will then execute suicidal cell death, but at the same time kill the invader in a kind of "kamikaze" strategy.

Elicitors or pharmaceutical compounds that can trigger programmed cell death cause a rapid breakdown of the dynamic meshwork of cortical actin filaments followed by a contraction of transvacuolar cables [220–222]. This phenomenon is not confined to plant immunity, but is found across eukaryotic cells in general (for reviews see [223, 224]) and for plant cells in particular [225, 226].

Cortical actin filaments have therefore emerged as part of an oscillatory sensor that can sense membrane integrity. Any impact on membrane integrity will cause a phase shift of the actin–auxin oscillations and result in actin remodeling, which is then transduced into programmed cell death. Since actin filaments are linked with

the unknown plant functional analogues of animal integrins, they should be able to respond to conformational protein changes at the membrane. From these considerations it is predicted that electromanipulation, even at energies that are not sufficient to cause irreversible pores, should impact on this actin-based switch between life and death.

4.6.4 The Plant Cytoskeleton Responds to nsPEFs

Methods shape concepts—the availability of fluorescent proteins allowing for imaging of specific organelles in living cells has revealed the seemingly static plant cells as highly dynamic systems. The term "cytoskeleton" was coined at a time when actin filaments and microtubules were accessible only through electron microscopy in ultrathin sections of fixed material. The concept of a static "cellular skeleton" has been replaced meanwhile by the model of a dynamic cytoskeletal equilibrium as evident, when fluorescent markers are followed after local bleaching (so-called fluorescence recovery after photo bleaching, FRAP) or when local changes of fluorescent color are followed, a novel approach made possible by the use of photoconvertible fluorescent proteins [227]. The fluorescent protein technology in combination with advanced fluorescence microscopy provided the tools to get insight into the dynamic changes of the plant cytoskeleton and the plant endomembrane system in response to electromanipulation. A panel of transgenic lines of the cellular plant model tobacco BY-2 (reviewed in [228]) expressing either GFP fusions of plant tubulin, the actin-binding domain 2 of plant fimbrin, or the retention motif for the endoplasmic reticulum, HDEL, in fusion with GFP, made it possible to follow the response of cytoskeleton and endomembrane system in living cells. These reporters were chosen, because they do not constrain the functionality of the cytoskeleton (in contrast to fluorescent phalloidin). A second prerequisite was the construction of a device that allowed administering nanosecond pulsed electric fields (nsPEFs) directly under the microscope, such that the cellular responses could be followed already during the first minutes after challenge. In fact, this approach revealed that the membrane-associated cytoskeleton responds swiftly and dramatically to electromanipulation [229].

Already a single pulse of 33 $kV.cm^{-1}$ at a duration of 10 ns was sufficient to disorder and disassemble cortical microtubules such that the fluorescently tagged tubulin used for visualization diffused into the mesh-like cortical cytoplasmic strands. This response had already initiated in the first minute after the pulse and was fully manifest at 3 min after pulsing. At the same time, the nucleus lost its ellipsoidal shape and was rounded up, which was a few minutes later followed by blebbing of the nuclear envelope. The response of actin was even swifter: cortical actin meshwork was rapidly depleted, while the transvacuolar cables contracted toward the nucleus within the first minute after the pulse. Similar to actin, the endoplasmic reticulum is subdivided into a highly dynamic submembrane meshwork of sheets that are connected by strands, whereas the transvacuolar ER strands

and the nuclear envelope appear to be relatively static. Nevertheless, a treatment with nsPEFs not only degraded the cortical ER, but produced a disintegration of the nuclear envelope followed by invasion of the GFP signal into the karyoplasm, from where it remained excluded in non-challenged control cells. This breakdown of the nuclear envelope occurred around 3–4 min after pulsing, which parallels the blebbing of the perinuclear microtubules.

These rapid responses of cortical microtubules and especially cortical actin were followed by somewhat slower changes in the behavior of the plasma membrane. To probe for potential disintegration of the plasma membrane, we measured the uptake of trypan blue, a dye that cannot permeate the membrane of living cells and is therefore classically used for viability assays. A variation of the electric dose by increasing the number of pulses showed that uptake of the dye became detectable from two pulses and was saturated at ten pulses [230].

A detailed time course of trypan blue permeability using five pulses revealed that the penetration of the dye initiated from the tip of the cells, whereas it was slower at the lateral flanks suggesting a strong impact of membrane curvature. This is to be expected from geometrical considerations of membrane charging: in a sphere, the local membrane voltage induced by a field depends on the radius, the field strength, and the cosines of the angle with the field vector [76].

Although the leakage of the dye became detectable already from the first minute after the five pulses, it required 6 min to become fully expressed [230]. In contrast, the cytoskeletal effects described above were already seen for a single pulse and earlier, which means that the response of the cytoskeleton was more sensitive and more rapid as compared to the permeabilization of the plasma membrane.

In the search for other cellular responses to nsPEFs, we had to decrease the stringency to a range, where cells still were able to survive for a sustained period. A mapping of prolonged viability over electrical energy density revealed that the cellular response followed an all-or-none pattern: below a certain threshold, all cells remained viable; above this threshold, all cells died [231]. For a treatment above the threshold, we observed a stratification of cytoplasmic strands, a block of cytoplasmic streaming, and a loss of nuclear positioning within 3–5 h after the treatment. The auxin efflux carrier PIN that was strictly localized to the plasma membrane in unpulsed controls partially detached from the membrane, such that its localization became diffuse. Since this loss of membrane localization of PIN should impair auxin flow through the cell file, this should also impinge on the synchronization of cell division within a file, a phenomenon, which can be scored as a reduction in the frequency of a diagnostic peak for hexacellular files and an increase of quadricellular files [232]. In fact, this very specific readout was observed following nsPEF treatment, indicative of an impaired auxin flow, corroborating the observed delocalization of the PIN protein. It should be mentioned that both, this division synchrony and the localization of the PIN protein, depend on actin filaments (reviewed in [217]).

In the next step, a subthreshold treatment of 20 pulses of 25-ns duration and 10 $kV.cm^{-1}$ was used to detect more subtle changes of cellular physiology. In fact,

two phenomena could be observed: A delay of mitotic activity by 1 day and a delay of premitotic nuclear migration by 1 day.

The (rapid) response of the submembranous cytoskeleton [229–231] is thus followed by (slower) increases of membrane permeability, impaired localization of auxin efflux carriers, delayed premitotic nuclear migration, and delayed onset of mitosis, and all these responses are intimately linked with the cytoskeleton. Although these correlations are consistent with a model, where the response of the membrane-associated cytoskeleton might be the cause of all these slower cellular responses to nsPEFs, they remain correlations and are no proof for a causal link. The question of causality will be investigated in the next section.

4.6.5 Plant Actin Controls the Response to nsPEFs

To state that a phenomenon A (nsPEF response of the actin cytoskeleton) is causative for a different phenomenon B (membrane permeability and cell death), three conditions have to be met: (1) A must precede B in time, (2) A must be necessary for B, and (3) A must be sufficient for B.

The first condition has already been discussed in the previous section: the cytoskeletal responses, especially the response of actin filaments, are observed earlier than the leakage of trypan blue into the cell [229, 230].

To test the second condition, it is necessary to manipulate the actin cytoskeleton before challenging the cell by nsPEFs. In addition to pharmacological manipulation, it is possible to use genetic engineering. Both strategies have been employed to probe for changes in the response to nsPEFs: In fact, a mild pretreatment by the actin-stabilizing drug phalloidin was able to efficiently suppress the penetration of trypan blue, indicative of a stabilization of membrane integrity [229]. In an alternative approach, actin-binding proteins that confer different degrees of actin stabilization were constitutively overexpressed under the control of a strong viral promoter (cauliflower mosaic virus 35S) in tobacco BY-2 and then trypan blue uptake recorded over increasing pulse numbers [230]. These curves were dampened correlated with the degree of actin stabilization—whereas the Lifeact probe (an -actin-binding peptide currently used as state-of-the-art marker for actin, because it is reported not to interfere with actin dynamics) yielded a dose–response curve that was identical to that recorded for non-transformed cells, the FABD2 marker (conferring a very mild stabilization of actin), already caused conspicuous dampening of the amplitude and a shift toward higher pulse numbers. The mouse talin probe, producing the strongest stabilization of actin, suppressed trypan blue uptake almost completely. To drive the assay to the highest possible stringency, we generated a transgenic line, where the actin-stabilizing LIM domain is under control of a glucocorticoid-inducible promoter. By addition of the artificial glucocorticoid dexamethasone, actin can be stabilized and compared to a non-treated aliquot of the same cell line as negative control, such that any effect of potential genetic differences can be ruled out. Doing so, the induced cell line showed a

strongly reduced uptake of trypan blue even for the highest pulse numbers tested. Thus, the second condition holds true as well: actin dynamics are necessary for membrane leakage. Although it cannot be excluded that there is also some impact of the transvacuolar actin cables and/or the perinuclear actin cage, this impact is estimated of minor importance, because these structures are already quite stable even in non-treated or non-transformed cells, whereas it is the dynamics of the cortical actin meshwork that are affected most.

To test the third condition, it is necessary to cause depletion of cortical actin filaments and contraction of transvacuolar cables in the absence of nsPEFs and to verify whether this will result in cell death. This experiment has become possible by using specific bacterial elicitors that produce a rapid actin response that down to the details of subcellular structure and timing matches the actin responses observed after nsPEFs. In fact, treatment of cell cultures of grapevine with the elicitor HrpN from the phytopathogenic bacterium *Erwinia amylovora* [220], of tobacco BY-2 with the elicitor HrpZ from *Pseudomonas syringae* [222], or simply with the plant defense compound resveratrol [221] was able to trigger rapid breakdown of cortical actin and contraction of transvacuolar actin cables, and these responses were followed by cell death. Thus, to induce a breakdown of cortical actin is sufficient to trigger cell death in the absence of nsPEF challenge.

Thus, all three conditions have been experimentally verified and found to be valid. It is therefore feasible to assume a causal link between the actin response at the plasma membrane and subsequent cellular responses (membrane leakage and cell death).

However, the conclusion of a dynamic actin population underneath the plasma membrane as a primary target of electromanipulation through nsPEFs is prone to raise some controversy: Whereas longer pulses with lower field strength are thought to cause reversible pore formation in the plasma membrane and can induce membrane passage of macromolecules, shorter pulses with higher field strength are discussed to cause mainly intracellular electromanipulation [233, 234]. The reason for this prediction is that the charging of the cell membrane should be slower than the penetrance of the electric field into the cell interior. Thus, intracellular membranes or organelles should be targeted before the energy can be dissipated into the plasma membrane [19, 235–237]. In fact, rupture of intracellular granules or vacuoles without detectable electroporation to the outer membrane [20, 237] or calcium release [234, 238] has been reported for mammalian cells after exposure to nsPEFs. However, rapid changes of plasma membrane permeability explained by the formation of nanopores [236, 239, 240] even for pulse durations of 10–60 ns [121, 241, 242] challenge this idea even for animal cells. In addition, the distribution of electric fields is definitely different in a cell, where, in addition to the plasma membrane, a second extensive membrane system, the tonoplast lining the vacuole, is present.

Rather than following theoretical considerations, we addressed this topic experimentally. A good deal of the discrepancy is caused by the fact that experiments conducted in different systems under different conditions and with different scopes have been compared. It was therefore relevant to address this question in a single

experimental system, where the same molecular target is localized either in the cell interior or near the plasma membrane and where different cellular functions can be assigned to these two subpopulations of the target molecule. Through our investigation of the plant cytoskeleton, we attained access to such a candidate molecule: KCH, a plant-specific member of the kinesin-14 family, links microtubules and actin filaments [243] occurring in two subsets that confer two different cellular functions [156]—one subset is linked with the perinuclear actin basket and important for premitotic nuclear migration and mitosis [153]. The second subset is not linked to actin filaments and moves slowly with cortical microtubules and thus plays a role for cell expansion. To address the influence of KCH, we simply used a tobacco BY-2 cell line overexpressing this protein in fusion with GFP [231]:

As a cellular readout for the nuclear function of KCH, nuclear movement heralding the ensuing cell division was quantified [153] and found to be delayed by overexpression of KCH, as well as by a mild nsPEF treatment. A combination of both factors acted synergistically. Although this might indicate a site of action at the nucleus, i.e., in the cell interior, it should be kept in mind that the nucleus is tethered, through a radial network of actin filaments and microtubules, to the cell wall by means of transmembrane proteins [151]. A similar delay of nuclear migration might therefore be produced, when the connections of this radial network to the plasma membrane were disrupted by nsPEFs. Thus, the analysis of nuclear migration alone is not sufficient to decide on the site of action.

We therefore exploited cell expansion as a second cellular function that is unequivocally linked to the cortical microtubules subtending the plasma membrane. In fact, we observed that overexpression of KCH promoted cell expansion, and that this promotion was stimulated by nsPEFs in the KCH overexpressor but not in the non-transformed wild type, and that cell expansion responds more sensitively as compared to cell division. In other words, there is a strict synergy between KCH overexpression and nsPEFs with respect to a function that is clearly located in the cytoskeleton adjacent to the plasma membrane. In contrast to the hypothetical nsPEF target in the cell interior, the experimentally verified target site at the plasma membrane can explain all observations of this study supporting the cytoskeletal signaling hub at the membrane as primary target for nsPEFs in plant cells.

Although a functional model of this hub is still far from conceived, it is already possible to distil from our data and those of others a structural model as a conceptual framework to understand the cellular effect of electromanipulation.

Although the cortical cytoskeleton has been observed to be very close to the membrane, it is not clear, whether there is a direct connection or whether the link is rather indirect through third molecular partners. The resolution of light microscopy is limited to about 250 nm in xy and to about 500 nm in z, even for advanced confocal microscopy (for a review see [244]). However, it is possible to break the resolution barrier in z-direction by means of total internal reflection fluorescence (TIRF) microscopy. This novel technique uses an evanescent wave from a totally reflected excitation beam. This wave can only penetrate 50–100 nm into the specimen, such that the fluorescence observed under these conditions must come from the very periphery of the cell. For walled plant cells, this technique is not

applicable, because the cell wall is by far thicker than the range for the evanescent wave. Several reports that had claimed TIRF imaging for plant cells have later been shown to be misled by an optical artifact called variable-angle epifluorescence (VAEF), which allows to view the uppermost few μm of a specimen without optical bleedthrough from the deeper layer [245]. In contrast, true TIRF records only the uppermost 50 nm and is, due to the curved topology of the specimen, confined to a narrow field of observation. To see whether the cytoskeleton is localized in close proximity to the plasma membrane, protoplasts were generated from cells expressing either the actin marker ATFABD or the microtubule marker AtTuB6 in fusion with GFP and viewed by TIRF microscopy. We observed that actin filaments were organized in starlike plaques, from where finer filaments emanated. The crossings of filaments appeared as punctate structures. The pattern for microtubules appeared similar, but the starlike centers were much finer and the setup appeared to be more delicate as compared to the actin filaments. The distance between these structures and the membrane is estimated to be in the range of a single microtubule; otherwise they would not be imaged by TIRF. The field of observation was small (around 5 μm in diameter), which would be expected from a penetration depth of 50 nm and which is clear evidence that the recorded structures were imaged by true TIRF and not by VAEF. We think that the punctate centers of the starlike cytoskeletal structures are the structural manifestation of the signaling hub.

This signaling hub seems to be embedded into a complex topology of the plasma membrane that deviates from the straight surface underlying most theoretical models of membrane charging. This topology depends on the cytoskeleton. There are two lines of evidence for this idea.

Stabilization of the submembranous cytoskeleton caused an increase in the apparent thickness of the cell membrane. Since the elementary membrane cannot be resolved by light microscopy, these changes of apparent thickness must be caused by membrane topologies, leading to a model of tubulovesicular membrane folds or invaginations that increase membrane surface and might be structurally maintained by actin filaments [230].

Plant protoplasts can swell within seconds in response to hypoosmotic shock without bursting. Since intensive expansion ability of plasma membranes is confined to ~2 % [246], there must be membrane material released from internal stores during hypoosmotic swelling which is difficult to be reconciled with a model of a straight membrane surface.

To get more insight into the functional relevance of actin for membrane integrity, we used the regulatory volume control in protoplasts as model and used hydraulic conductivity (L_p) as readout [247]. This readout could be derived from the time course of protoplast swelling and was then manipulated by different factors to identify molecular components interfering with this response. We found that chelation of calcium, inhibition of calcium channels, or manipulation of membrane fluidity by benzyl alcohol did not significantly alter L_p. In contrast, direct manipulation of the cytoskeleton via specific compounds either destabilizing or stabilizing actin filaments (latrunculin B, phalloidin) or microtubules (oryzalin, Taxol)

modulated conductivity. In addition, the bacterial elicitor harpin or modulation of phospholipase D was effective.

We further used optochemical engineering of actin using a caged form of the phytohormone auxin to break the symmetry of actin organization [248] in a single protoplast and found that the transcellular gradient of actin rigidity resulted in a localized deformation of cell shape (nota bene: under isotonic conditions) indicative of a locally increased L_p.

Whereas auxin-triggered actin dynamics were promoting the swelling response, bundling of actin blocked expansion, probably through mechanic tethering of the microtubule constrained swelling, leading to a model where a dynamic population of microtubules impedes the integration of membrane material into the expanding membrane. This microtubule population could be controlled by specific pharmacological activation of phospholipase D, a central component of a membrane–cytoskeleton signaling hub. This should produce two consequences:

1. The activation of phospholipase D would produce phosphatidic acid, an important activator of the membrane-bound NADPH oxidase RboH culminating in an apoplastic oxidative burst (for a review see [209]) that provides a central input for plant stress signaling including activation of programmed cell death.
2. The detachment of the cytoskeleton from the membrane invaginations would release additional membrane material for resealing of nanopores and for release of mechanical tensions within the plasma membrane.

It should be emphasized that this cytoskeletal membrane hub is subject to numerous positive and negative feedback regulations. For instance, the apoplastic reactive oxygen species will penetrate through aquaporins into the cortical cytoplasm and interfere with the bundling state of actin creating a signal, where, due to cytoskeletal tensegrity, the actin will contract toward the nucleus, which seems to be an important trigger to activate programmed cell death. In contrast, the integration of vesicles into the resealing membrane will remove PIP2, a downstream product of phospholipase D sequestering actin depolymerization factor 2 [249], such that actin dynamics will be reinstalled and the dynamic filaments will relink to the membrane preventing actin contraction. Whether a cell challenged by electromanipulation will rescue membrane integrity by resealing or whether it will be doomed to programmed cell death leading to a long-term loss of membrane integrity does not only depend on the physics of membrane charging, but is crucially decided by the relative timing of these antagonistic feedback loops.

4.6.6 Consequences for Current Imaginations on nsPEF Interactions with Cells

The results discussed in previous sections demonstrate that the plant cytoskeleton has a major impact on cellular responses upon nsPEF administration. In particular,

in the short pulse range, below 100 ns, the cytoskeleton bears a strong influence on membrane permeabilization. This fact might have been overseen in the past, because in the long pulse exposition regime, the effects of pore formation dominate and nowadays still are considered as a basic principle of membrane permeabilization.

Despite the existing differences in cytoskeletal structure between mammalian and plant cells, a role of the cytoskeleton for the response to pulsed electric fields is also supported by experimental results obtained from mammalian cells. Consistently, it is reported that cortical actin filaments disintegrate, and microtubular structures depolymerize after PEF treatment [250–252] within some minutes and recover later in a time frame of an hour [252]. Already back in the 1990s, it was shown that the cytoskeleton is strongly involved in membrane resealing after permeabilization by pulsed electric fields [99, 253]. Treatment with compounds acting on the cytoskeleton prolonged resealing times from minutes to hours. PEF-induced disintegration of cortical cytoskeleton structures is reported to decrease the Young's modulus of the cell boundary by more than a factor of 2 [250, 254], underlining the importance of the tensegral properties of the cytoskeleton for mechanical stabilization and shaping of mammalian cells.

The findings on the plant cytoskeleton provide unambiguous evidence for a physical link between the cortical actin cytoskeleton and the plasma membrane at distinct points. Actin filaments emanate in a starlike manner from these interconnections. It also could be demonstrated that nsPEF-induced dissolution of the cortical actin meshwork provokes permeability of the plasma membrane for larger molecules, whereas chemical stabilization of the actin meshwork maintained membrane integrity when challenging the plant cells by the same pulse treatment [229, 230]. This demonstrates that membrane permeabilization is not solely caused by the formation of pores in the PL bilayer, which undoubtedly is one of the primary effects of membrane permeabilization, but also can be evoked via destabilization of the submembranous cytoskeleton, which obviously feeds back to membrane integrity. In addition, it could be demonstrated that cytoskeleton plays an active and necessary role in membrane permeabilization of plant cells.

Besides membrane site-associated responses, nsPEFs affect the cell cycle as evident from a delay of premitotic nuclear positioning. Also intercellular auxin transport is disturbed.

The causal sequence for the different cellular responses and the cytoskeletal response remains to be elucidated. Whether dissolution of the cytoskeleton is the cause of osmotic swelling as strongly suggested by the current work or whether it is the consequence of osmotic swelling as proposed for mammalian cells [255] has to be clarified for each system by functional analysis (including time-course studies). Also the biophysical trigger for cytoskeletal dissolution is pending so far. Forces due to dipole alignment of actin or tubulin monomers along the direction of the electric field direction appear to be feasible to evoke filament disruption. Alternatively, a complete loss of phospholipid ordered structure [101] around the cytoskeleton–membrane links in consequence of the pulsed electric field might also cause the subsequent loss of cytoskeletal structure.

Irrespective of the underlying biophysical mechanisms, the sensorial properties of cytoskeleton and in particular on the sensory feedback of stimulation by pulsed electric field stimulation will open promising new applications for electromanipulation of plant cells by pulsed electric fields.

4.7 Intracellular Trafficking of Plasmid and siRNA After Electroporation

David A. Dean

The fate of nucleic acids once translocated across the plasma membrane depends on the nucleic acids themselves. For example, while plasmids must make their way to the nucleus in order to be expressed, siRNA, miRNA, shRNAs, mRNA, and most RNaseH-dependent and independent DNAs and RNAs (such as DNAzymes or hammerhead ribozymes) function within the cytoplasm so they do not need to traffic to the nucleus. Although the biophysical and biological environment of the cytoplasm impacts movement of all types of nucleic acids, the greatest amount of information has been gathered for the movement of plasmids, and as such, unless noted, most of the following discussion will be directed at the productive and nonproductive movement of plasmids throughout the cell.

4.7.1 A Possible Role for Actin

Once the plasma membrane has been destabilized by electroporation allowing for nucleic acid entry, both DNA and RNAs are confronted by a number of barriers that must be overcome for their function, all of which are independent of the electric field (Fig. 4.16). Studies with fluorescently labeled plasmids and fluorescently labeled RNAs show that the translocated nucleic acids remain near the inner surface of the plasma membrane for a period of time, prior to movement toward the interior of the cell [102, 214]. Using fluorescence labeling and fluorescent protein techniques, it was shown that DNA and actin co-localized to the same spots at the permeabilized membrane facing the anode immediately following electroporation [214]. Moreover, when the actin network was destabilized with latrunculin B, reduced levels of DNA were present at the spots, suggesting that the actin may play a role in the internalization of the DNA itself. Cortical actin forms a meshwork beneath the plasma membrane to provide structure to the cell and to link the intracellular and extracellular environment for signaling. It is likely that this network acts to temporarily "trap" the molecules after they have crossed the plasma membrane. Similar findings have been reported for entry of a number of viral particles [256, 257]. It is currently not known how the DNA escapes this region

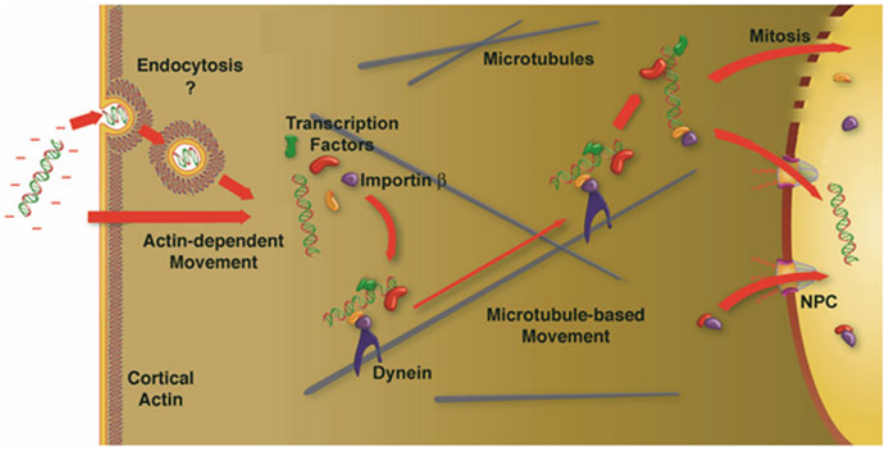

Fig. 4.16 Post-electroporation intracellular trafficking of plasmids. Following electropermeabilization of the membrane, plasmids may enter the cell by either endocytosis and/or direct entry into the cytosol at which point they must traverse the cortical actin layer, perhaps using actin-based movement [102, 214]. Once free in the cytoplasm, plasmids are rapidly complexed by a number of DNA-binding proteins in the cytoplasm which in turn bind to other proteins to form large protein–DNA complexes [259]. Transcription factors bound to the DNA interact with importinβ and other proteins that in turn link the complex to dynein for movement along microtubules to the nucleus where it falls apart at the nuclear periphery [264]. Nuclear entry is then mediated by importinβ in a sequence- and importin-dependent manner through the nuclear pore complex (NPC) in nondividing cells or independent of importins and any DNA sequence requirement during mitosis and the associated dissolution of the nuclear envelope (*top*)

or whether it is by directed movement or diffusion, but the nonuniform nature of the cortical actin meshwork may allow for localized diffusion of the nucleic acids at distinct sites or at "holes" out of this region of the cell and toward the interior.

Apart from the possible role of cortical actin in the internalization and trafficking of plasmids, several studies have also implicated a role for actin filaments in the cytoplasmic trafficking of plasmids in addition to that of the microtubule network [102, 214]. When actin dynamics were perturbed with drugs, both stabilization and destabilization of the networks resulted in slight decreases in the percent of fluorescently labeled plasmids showing active transport or the total distance traveled by the particles using single-molecule particle tracking [102, 214]. In contrast to these findings, earlier work showed that disruption of the actin cytoskeleton resulted in greatly enhanced diffusion of large DNA fragments within the cytoplasm of microinjected cells [258]. Proteomic studies from our laboratory have found that several actin-based motors (myosin 1B, 1C, and 9) are found in the protein–DNA complexes at early times after electroporation (15 min) along with a number of different microtubule-based motors [259], supporting a possible role for actin-based movement of DNA particles, at least at times between entry of the DNA into the cytosol and its binding to microtubules.

4.7.2 Microtubule-Based Movement of Plasmids

The cell cytoplasm has been described as early as the 1940s as resembling a reversible gel–sol system that is relatively stiff and does not allow for a great deal of free diffusion of large molecules [260]. It is a complex system composed of multiple cytoskeletal elements, including actin microfilaments, microtubules, and intermediate filaments, all of which are organized into a complex, crowded latticework that is constantly remodeling in response to a variety of internal and external stimuli. It has been shown that both double-stranded DNA fragments greater than 1000–2000 bp and macromolecule-sized solutes display almost no passive diffusion and are largely immobile in the cytoplasm of HeLa cells and fibroblasts [261, 262]. Thus, in order to traffic to the nucleus, plasmids must use directed movement, and it has been demonstrated that microtubules and their associated motor proteins are used to do so [102, 259, 263–267].

Several studies have shown that an intact microtubule network and motor proteins such as dynein are necessary for transfected naked DNA and some viruses to traverse the cytoplasm and reach the nucleus [102, 266, 268, 269]. When the microtubule network was disassembled by treatment with nocodazole, movement of DNA toward the nucleus was largely abolished [102, 266]. By contrast, modulation of the actin cytoskeleton had minor effects [266, 268]. Not only was movement of labeled DNA inhibited, but gene expression of reporter genes on the plasmids was also blocked [266, 268]. Inhibition of dynein, the major microtubule-based motor protein driving movement toward the nucleus, resulted in the same loss of plasmid movement and expression [102, 266]. Biochemical analysis has confirmed these findings. In one set of experiments, a spin-down assay in which plasmid DNA, cell extracts, and stabilized microtubules were incubated and then centrifuged to separate polymerized microtubules and any proteins or DNA interacting with them from the reaction was used to demonstrate that DNA interacted with microtubules [264]. In these studies, DNA interacted with microtubules only when cytoplasmic extracts were provided as a source of adapter proteins. By testing the ability of plasmids carrying different genes, transcriptional control elements, and DNA sequences to bind to the microtubules in this assay, it was found that plasmids interacted with microtubules in a sequence-specific manner. While the bacterial plasmid pBR322 failed to interact with microtubules in this spin-down assay, as did a number of plasmids containing various viral or cellular promoters, plasmids carrying the CMV promoter bound to the microtubules in the presence of cytoplasmic extracts [264]. Sequence analysis revealed that the only DNA element common to microtubule-binding promoters was the binding site for the cAMP response element-binding protein (CREB), and when a single CREB site was placed into pBR322, it interacted with microtubules. When the movement of individually fluorescently labeled plasmids was followed by particle tracking, this sequence specificity of movement was recapitulated in living cells: while pBR322 shows only marginal diffusive movement limited to small regions of the cytoplasm near its site of cytosolic entry, plasmids carrying CREB-binding sites or one of

several other eukaryotic promoters and enhancers showed active and directed movements at much faster rates [102, 259, 263, 264]. Real-time particle tracking of quantum dot-labeled plasmids has shown that the DNA moves along microtubules with kinetics and dynamics that are in line with those seen for microtubule-based movement of organelles, virus particles, and proteins [102, 259, 263, 264].

As the spin-down assays suggest, plasmids do not interact with microtubules directly, but require adapter proteins in the cytoplasm to act as intermediaries between the DNA and the microtubules. Once the DNA has entered the cytoplasm and moved beyond the cortical actin domain, it binds to a number of sequence-specific and nonspecific DNA-binding proteins as well as a number of other proteins to form large protein–DNA complexes [259, 270, 271]. The formation of these complexes is rapid: within 15 min of electroporation in adherent cells, plasmids can be detected to physically interact with transcription factors, including CREB, as well as a number of other proteins [264]. These additional proteins include a number of microtubule accessory proteins and the motors dynein and kinesin, as well as tubulin itself.

4.7.3 Composition of the Protein–DNA Complexes

Using a proteomic approach, the nature of cytoplasmic plasmid–protein complexes has been investigated by several groups. Two approaches have been taken, both of which have produced similar and complementary data. The first approach has relied on in vitro formation of protein–DNA complexes by either incubating free plasmids with cytosolic extracts and then purifying the plasmids with a pull-down assay prior to analysis by mass spectrometry [270] or by incubating cytoplasmic extracts with plasmids that have been immobilized on a chromatography support and then identifying proteins eluted from the columns by mass spectrometry [271]. A second approach has been to cross-link plasmids with proteins inside of living cells at various times after electroporation and then isolate the plasmid–protein complexes for proteomic analysis [259]. Results from the cell-free studies identified upward of 200 proteins present in the DNA complexes, but the proteins identified were likely those that bound most stringently to the DNA or within the higher-order structure. The precipitation studies in living cells were able to identify many more proteins ($>$500) and showed that these complexes were dynamic and showed changing composition over time. This is likely more representative of the real situation in transfected cells.

In addition to several transcription factors as seen in previous studies, a number of proteins that fell into specific categories were identified and shown to bind specifically to plasmids that displayed active movement through the cytoplasm, but not to DNAs that showed very little movement (e.g., pBR322). At all time points, more unique proteins were bound to transcriptionally active plasmids that move (e.g., DNAs containing the CMV promoter) than pBR322. For example, at the 30-min time point, 324 unique proteins were identified in CMV promoter-

containing plasmids but only 60 in pBR322 samples [259]. Specific proteins bound to moving plasmids (but not pBR322) included microtubule-based motor proteins (e.g., kinesin and dynein), proteins involved in protein nuclear import (e.g., importinβ-1, importin7, importin4, importinα, transportin, RAN, and several RAN-binding proteins), a number of hnRNP- and mRNA-binding proteins, heat shock proteins, chaperones, and transcription factors. Many of these were also identified in the cell-free binding studies [270, 271]. The significance of several of the proteins involved in protein nuclear localization and plasmid trafficking was determined by the monitoring movement of microinjected plasmids via live cell particle tracking in cells following protein knockdown by siRNA or through the use of specific inhibitors. Knockdown of importin7 had no effect on trafficking or nuclear import (see below), but knockdown of importinβ-1 inhibited trafficking and nuclear import down to the level of pBR322, a plasmid that neither traffics on microtubules nor is imported into the nucleus [259]. By contrast, knockdown of importinα had no effect on cytoplasmic movement but inhibited nuclear import by 50 %, suggesting that the different proteins involved in protein nuclear localization play distinct roles in intracellular DNA movement.

4.7.4 Nuclear Entry of Plasmids

Following trafficking of plasmids to the interior of the cell, they must enter the nucleus for productive gene expression to take place. As for microtubule-based movement, it is the proteins that bind to the plasmids that mediate entry into the nucleus in nondividing cells following electroporation or any transfection method. When plasmids carry certain DNA sequences termed DNA nuclear-targeting sequences (DTS), they form complexes with specific nuclear localization signal (NLS)-containing proteins that in turn bind to importins for entry of the complex through the nuclear pore complex into the nucleus (Fig. 4.17) [272–279]. The most common proteins that bind to these sequences are transcription factors (such as

Fig. 4.17 Model for DNA nuclear import in nondividing cells. If plasmids containing sequences that act as scaffolds for transcription factors and other DNA-binding proteins (termed DTS, or DNA nuclear-targeting sequences) are deposited into the cytoplasm during transfection, they can form complexes with these proteins, thereby attaching NLSs to the DNA. Some, but not all, of these NLSs may be in a conformation able to interact with importins for transport of the DNA–protein complex into the nucleus through nuclear pores

CREB) which are translated and many times retained in the cytoplasm in order to regulate their function [280]. Under normal circumstances, a typical transcription factor would be transported into the nucleus after synthesis or upon receiving an activation signal (e.g., TNFα-induced NF-kB translocation), bind to its DNA target sequence present in various promoters, and activate or repress transcription. However, if a plasmid containing the transcription factor binding site is present in the cytoplasm, the cytoplasmic transcription factor may bind to this site before nuclear import. The NLS import machinery (importins) will then bind to the DNA-bound transcription factors and translocate the DNA–protein complex into the nucleus [281, 282]. While it could be assumed that any eukaryotic promoter would act as a DTS, this appears not to be the case, since many strong viral and cellular promoters and enhancers have no DTS activity [272, 273, 277]. Alternatively, any plasmid, regardless of sequence, has the ability to enter into the nucleus during mitosis, once it reaches the area of the nuclear periphery. Either way, these trafficking events through the cytoplasm and into the nucleus are not unique to electroporation, but are those seen for all nonviral methods for gene delivery.

4.7.5 Plasmid Movement Within the Nucleus

Although it is well accepted that DNA must enter the nucleus in order for gene expression to occur during gene transfer, what happens to the DNA once inside the nucleus has not been extensively investigated. Numerous strategies to increase efficiency of gene transfer and transcription have been developed, but almost all have assumed that the end goal of DNA trafficking is to reach the nucleus and that transcription is independent of any other nuclear function. A number of studies using transfected and microinjected cells show that expressing plasmids do indeed display discreet staining patterns, suggesting movement and/or localization of the DNA once inside the nucleus [272, 273, 283–286]. This suggests that gene expression and subnuclear localization of transfected plasmids may be linked. Indeed, several reports have found that the transcriptional capability and transcribed sequence of a plasmid alters its intranuclear trafficking patterns [287–290]. For example, when plasmids carrying no eukaryotic promoter sequences were microinjected into the nuclei, they remained diffuse and evenly spread throughout the nucleus for at least 4 h postinjection [287]. By contrast, plasmids carrying RNA polymerase (RNAP) II promoter sequences and transcribable mRNA localized to discreet foci within the nucleus starting within minutes and by 4 h were mostly localized to a limited number of areas that co-localized with RNAP II and splicing machinery [287]. Similarly, when plasmids carrying an RNAP I promoter and rRNA sequences were injected into the nucleus, they localized to nucleoli with nucleolar transcription and processing factors [287, 288].

When cells were treated with transcription inhibitors, both RNAP I and RNAP II promoter plasmids failed to redistribute [287, 288]. Similarly when the RNAP II TATA box was mutated or the rDNA sequences were removed from the RNAP I

plasmid such that neither could produce RNA, the plasmids also failed to redistribute throughout the nucleus [288]. These results suggest that transcription is needed for the large-scale redistribution of plasmids throughout the nucleus, although how is not yet understood. It is possible that once in the nucleus, low-level transcription initiates from the plasmids and the nascent RNA chain, while still bound to the plasmid via RNAP, may interact with modifying and splicing enzymes and other nuclear proteins that mediate active movement of the DNA to transcription centers that engage in high-level expression. Further experimentation is needed to understand these dynamics and their implications.

4.8 Intracellular Signaling Pathways Activated by Nanosecond Pulsed Electric Fields

Ken-ichi Yano and Keiko Morotomi-Yano

Nanosecond pulsed electric fields (nsPEFs) are increasingly regarded as a novel means for life sciences. One of the prominent effects of nsPEFs is efficient induction of cell death, which has attracted considerable interest for their applications in cancer therapy. Recent studies have demonstrated that human cells respond to nsPEFs through activation of various intracellular events. These intracellular responses can even be induced by weak nsPEFs that are insufficient to induce cell death or visible morphological changes under the microscope. Exposure to nsPEFs elicits sequential protein phosphorylation involved in signaling pathways and leads to the induction of downstream events such as gene expression and suppression of protein synthesis. This section offers an overview of the current knowledge of the intracellular signaling pathways activated by nsPEFs. Effects of nsPEFs on cytoskeleton and mechanisms for cell death are described in other Sects. 4.6 and 4.10.

4.8.1 General Principles of Intracellular Signal Transduction Activated by External Stimuli

Cells have elaborate mechanisms to respond to physical and chemical stimuli from their outer environment. Cells can detect such external stimuli and rapidly transmit them by evoking sequential changes in cellular proteins, mainly via protein phosphorylation, which is a covalent addition of a phosphate group to a specific residue in a target protein. Phosphorylation alters protein conformation and can either increase or decrease the activity of the protein. Protein phosphorylation is mediated by protein kinases, and the catalytic activity of a protein kinase itself is commonly modulated by phosphorylation by other protein kinases. A cascade of protein

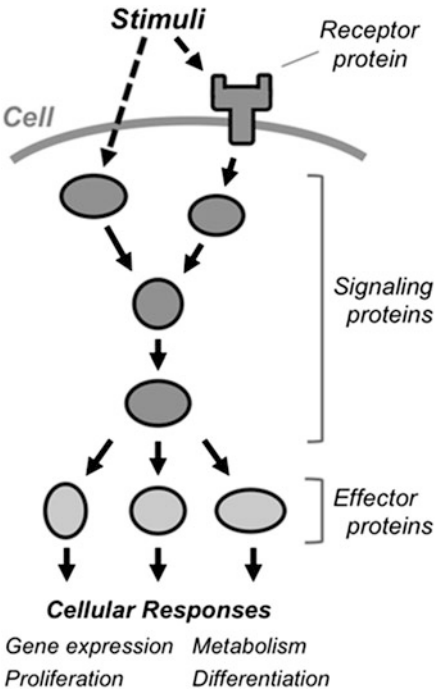

Fig. 4.18 Simplified diagram of signal transduction in human cells. External stimuli are perceived by the cell via surface receptor proteins or intracellular proteins and are transduced to downstream signaling proteins, many of which are protein kinases. Protein kinases in the signaling pathway phosphorylate downstream effector proteins that in turn affect various cellular activities

phosphorylation by protein kinases forms an intracellular signaling pathway. An intracellular signaling pathway can be activated by an external stimulus, relaying and amplifying it by phosphorylation of multiple downstream target proteins in the cell (Fig. 4.18). The effect of protein kinases is opposed by the activity of protein phosphatases that catalyze the dephosphorylation of proteins. When dephosphorylated, proteins return to their original conformation and functional states. The combined activities of protein kinases and protein phosphatases ensure the tight control of intracellular signaling pathways in response to external stimuli [291].

Activation of an intracellular signaling pathway results in the phosphorylation of downstream effector proteins that are involved in various cellular activities such as metabolism, proliferation, differentiation, and motility (Fig. 4.18). Thus, intracellular signaling pathways serve as a means for the control of various cellular activities. Furthermore, many transcription factors are located downstream of signaling pathways, and their functions are positively or negatively regulated via protein phosphorylation. Hence, the activation of a signaling pathway often leads to altered gene expression and consequent increase or decrease in specific proteins, which ultimately affect the nature and behavior of the cell. For these reasons, intracellular signal pathways play critical roles in proper responses to external stimuli, and their aberrant control is frequently associated with cellular dysfunctions such as malignant transformation [291].

4.8.2 Activation of Intracellular Signaling Pathways by nsPEFs

4.8.2.1 MAPK Pathways

The mitogen-activated protein kinase (MAPK) pathways are intracellular signaling pathways that are activated by extracellular stimuli and transduce them into cellular responses [292]. A typical MAPK pathway consists of three sequentially acting protein kinases, namely, MAPK, MAPK kinase (MAPKK), and MAPK kinase kinase (MAPKKK). Each MAPK pathway is named after its MAPK component. Activation of the MAPK pathway is initiated by the activation of MAPKKK that is triggered by an external stimulus. Activated MAPKKK phosphorylates its downstream MAPKK, and MAPKK in turn phosphorylates its downstream MAPK. This MAPKKK–MAPKK–MAPK module is well conserved among eukaryotes. Human cells have multiple MAPKs, and each MAPK functions in a distinct pathway and plays its physiological role. Among the multiple MAPK pathways in humans, three MAPK pathways are best characterized so far. The extracellular signal–regulated kinase (ERK) pathway is activated mainly in response to mitogens and growth factors. The c-jun N-terminal kinase (JNK) and p38 pathways are activated by environmental stress and inflammatory cytokines [292].

Activated MAPKs affect various intracellular processes by phosphorylating many downstream effector proteins, which include transcription factors. Phosphorylation of transcription factors by the activated MAPKs rapidly induces expression of a limited set of genes without de novo protein synthesis. These genes are called immediate-early genes and include *c-fos*, *c-jun*, and *Egr1*, which also encode transcription factors and further regulate the expression of many other genes. Thus, the activation of the MAPK pathways elicits complex changes in intracellular processes by changing protein activities and gene expression [292].

At the cellular level, the outcome of the MAPK activation is dependent on the cellular context, because different cell types contain different amounts of the MAPK pathway components. For example, relative activities of protein kinases and their counteracting phosphatases determine the magnitude and duration of the activation of the MAPK pathways. The amounts of downstream targets for a certain member of MAPKs vary among different cell types. Thus, a single external stimulus yields different outcomes in different cell types. Under physiological conditions, the MAPK pathways play critical roles in the control of proliferation, differentiation, migration, and apoptosis, depending on the cellular context. Furthermore, dysregulation of the MAPK pathways is frequently implicated in inflammation, obesity, malignant transformation, and tumor invasion.

Effects of nsPEFs on the MAPK pathways were demonstrated by experiments using the HeLa S3 cell line, which is one of the most common cell lines used in molecular biology [293]. The cells were exposed to shots of nsPEFs and subjected

to Western blot analyses of major protein components in three representative MAPK pathways, JNK, p38, and ERK. The obtained results are summarized in Fig. 4.19. Application of nsPEFs induces phosphorylation of JNK, p38, and ERK in different temporal patterns. Their upstream MAPKKs (MEK1/2, MKK3/6, and MKK4) are also phosphorylated after exposure to nsPEFs. Furthermore, multiple downstream factors in the MAPK pathways, including MSK1, Hsp27, ATF2, p90RSK, and c-Jun, are phosphorylated after nsPEF exposure. In addition to protein phosphorylation, expression of the immediate-early genes of the MAPK pathways is transiently activated. The expressions of *Egr1*, *c-jun*, and *c-fos* are increased by more than tenfold, whereas *c-myc* expression is not significantly affected in nsPEF-exposed cells. Specific inhibitors for the JNK, p38, and ERK pathways suppress the phosphorylation of distinct downstream proteins and gene expression, which validate the functional connection between an individual MAPK pathway and specific downstream events in nsPEF-exposed cells [293]. In these experiments, HeLa S3 cells were used as a model to understand the key aspects of MAPK activation by nsPEFs. As described above, different cell types have different amounts of components of the MAPK pathways, and the outcome at the cellular levels is determined depending on the cellular context. The observation of the nsPEF-induced MAPK activation raises the possibility that nsPEFs can be utilized to control MAPK-related cellular activities such as proliferation and differentiation.

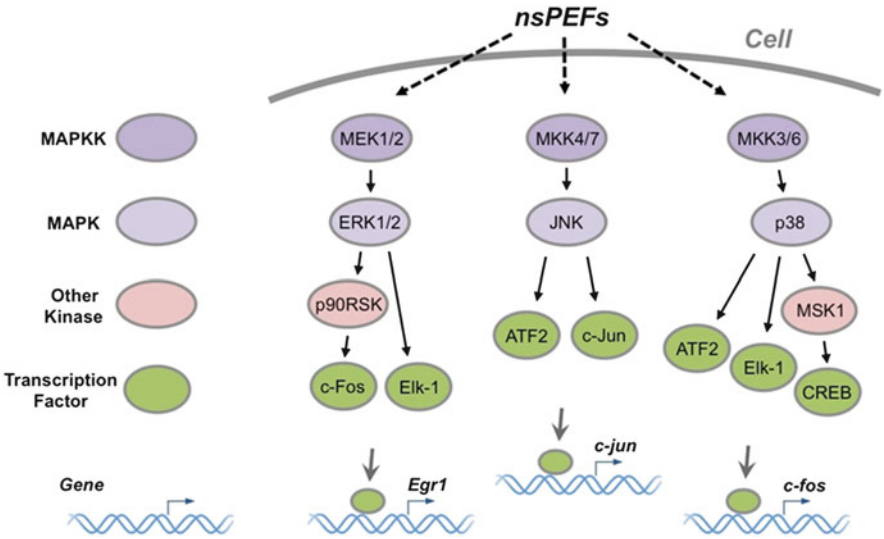

Fig. 4.19 Activation of the MAPK pathways by nsPEFs. Human cells possess multiple MAPK pathways that are differently activated by external stimuli. MAPKs phosphorylate various effector proteins, including transcription factors. Exposure of the cell to nsPEFs induces the phosphorylation of the proteins indicated in the figure. The three genes shown in the figure are transcriptionally activated after nsPEF exposure

4.8.2.2 AMPK Pathway

AMP-activated protein kinase (AMPK) plays a critical role in energy homeostasis [294]. AMPK is activated in response to decreased cellular energy that is represented by decreased ATP and increased AMP concentrations. Once activated, AMPK phosphorylates multiple metabolic enzymes and their regulators to modulate their activities, contributing to the restoration of energy balance. In human cells, two protein kinases are involved in the phosphorylation and consequent activation of AMPK (Fig. 4.20). LKB1 is a primary AMPK kinase and phosphorylates the AMP-bound form of AMPK that arises under low-energy conditions. Because LKB1 has cellular functions as a tumor suppressor, its gene is frequently lost in cells derived from malignant tumors such as HeLa S3 cells. Ca^{2+}/calmodulin-dependent protein kinase kinase (CaMKK) has a potential role as an alternative AMPK kinase and acts on the AMPK phosphorylation in LKB1-deficient cells. CaMKK requires increased intracellular Ca^{2+} for its enzymatic activity, whereas LKB1 is a Ca^{2+}-independent protein kinase.

Exposure of cultured human cells to nsPEFs activates AMPK in a cell type-dependent manner (Fig. 4.20) [295]. In Jurkat cells, LKB1 is a primary AMPK kinase, and nsPEFs induce AMPK activation. On the other hand, HeLa S3 cells lack functional LKB1, and CaMKK serves as an AMPK kinase. Accordingly, a CaMKK inhibitor suppresses AMPK activation by nsPEFs in HeLa S3 cells, but not in Jurkat

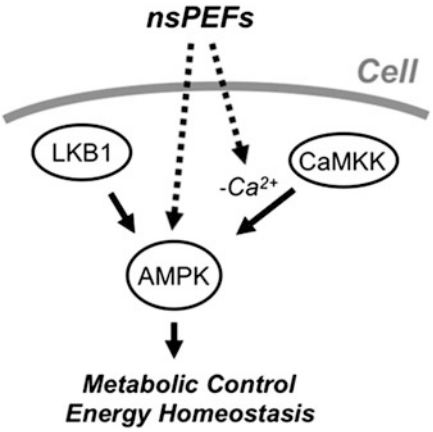

Fig. 4.20 Activation of the AMPK pathway by nsPEFs. AMPK is a critical regulator of cellular homeostasis and is activated via phosphorylation by two protein kinases. LKB1 is a major AMPK kinase. CaMKK is an alternative AMPK kinase that requires increased cytoplasmic Ca^{2+} for its enzymatic activity. Exposure of the cell to nsPEFs induces AMPK phosphorylation by LKB1. In LKB1-deficient cells, such as HeLa S3 cells, AMPK phosphorylation by nsPEFs is mediated by CaMKK and requires the presence of extracellular Ca^{2+}

cells. In both cell lines, AMPK phosphorylation quickly occurs within 1 min after nsPEF exposure.

Exposure to nsPEFs is known to increase cytosolic Ca^{2+} concentrations, mainly due to the influx of extracellular Ca^{2+}. The Ca^{2+} influx differently affects nsPEF-induced AMPK activation in Jurkat and HeLa S3 cells [295]. In Jurkat cells, AMPK activation is quickly induced by nsPEFs, irrespective of the presence or absence of extracellular Ca^{2+}. In HeLa S3 cells, the absence of extracellular Ca^{2+} causes a substantial reduction in the nsPEF-induced AMPK activation, indicating that Ca^{2+} influx is critical for the CaMKK-mediated AMPK activation in nsPEF-exposed HeLa S3 cells. These observations provide an example of a causal relationship between the cellular context and the Ca^{2+} dependency of nsPEF-induced intracellular responses.

4.8.2.3 Phosphoinositide Signaling Pathway

In addition to proteins, small molecules play important roles in intracellular signaling [291]. A small amount of phosphatidylinositol 4,5-bisphosphate (PIP2) exists in the inner layer of the plasma membrane. The hydrolysis of PIP2 yields two compounds, inositol 1,4,5-triphosphate (IP3) and diacylglycerol (DAG), both of which function as potent second messengers. IP3, which is water soluble, diffuses into the cytoplasm and binds to IP3 receptors in the ER to release Ca^{2+} from the ER. DAG remains tethered in the inner surface of the plasma membrane and activates protein kinase C (PKC) family members, many of which are Ca^{2+}-dependent kinases and further phosphorylate multiple proteins to induce various cellular responses (Fig. 4.21). PIP2 hydrolysis is catalyzed by phospholipase C (PLC), and the enzymatic activity of PLC is generally stimulated by external signals, such as hormones, via the activation of G-protein coupled receptors [291]. PIP2 binds to the inner layer of the plasma membrane. Exposure of the cell to nsPEFs yields two hydrolysis products of PIP2, namely, IP3 and DAG. IP3 elicits Ca^{2+} release from the ER, while DAG activates PKC.

Effects of nsPEFs on phosphoinositide signaling were investigated by using two sensor proteins for DAG and IP3, respectively [142, 143]. One sensor protein consists of a green fluorescent protein (GFP) fused to the PLCδ PH domain, which binds to both PIP2 and IP3. When exogenously expressed in cultured mammalian cells, this protein localizes in the plasma membrane and, after nsPEF exposure, rapidly diffuses into the cytoplasm, demonstrating the generation of IP3 in nsPEF-exposed cells. Another sensor protein contains GFP fused to the C1 domain of PKCγ, which binds to DAG. This sensor protein exists in the cytoplasm and translocates to the plasma membrane after nsPEF exposure, indicating DAG generation by nsPEFs. These observations clearly demonstrate that nsPEFs cause

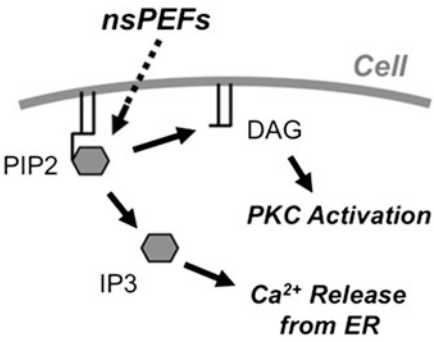

Fig. 4.21 Activation of the phosphoinositide signaling pathway by nsPEFs. PIP2 binds to the inner layer of the plasma membrane. Exposure of the cell to nsPEFs yields two hydrolysis products of PIP2, namely, IP3 and DAG. IP3 elicits Ca^{2+} release from the ER, while DAG activates PKC

increased levels of key molecules in the phosphoinositide signaling (Fig. 4.21). Future studies on the detailed mechanism for nsPEF-induced PIP2 hydrolysis as well as the effects on downstream events will provide important information for a better understanding of nsPEF actions.

4.8.3 Stress Response

4.8.3.1 Overview of Stress Responses

Cells often encounter various adverse circumstances and deleterious stimuli such as nutrient limitation, hypoxia, UV irradiation, heating, virus infection, and toxic agents. To withstand these conditions, cells activate multiple homeostatic mechanisms that are collectively called stress responses. Activation of stress responses frequently leads to transient suppression of general protein synthesis [297]. Because protein synthesis consumes large amounts of amino acids and energy, its transient suppression saves resources and serves as a protective mechanism to endure adverse conditions. The rate of protein synthesis is primarily regulated at the step of translation initiation, and the key event in the stress-induced translational suppression is the phosphorylation of the α-subunit of eukaryotic translation initiation factor 2 (eIF2α). This phosphorylation hinders the assembly of a protein complex required for translation initiation and thus results in the suppression of general protein synthesis.

The stress response involving eIF2α-phosphorylation is evolutionarily conserved among eukaryotic organisms from yeast to humans. In mammals, including humans, eIF2α-phosphorylation is mediated by four protein kinases that are activated in response to distinct forms of cellular stress (Fig. 4.22) [297]. Activation of PERK is induced by misfolded proteins in the ER. GCN2 is activated by amino acid deprivation and UV irradiation. PKR activation is triggered by double-stranded RNA produced during virus infection. HRI is activated by heme deprivation, heat shock, and oxidative stress in erythroid cells. At least one of these protein kinases is activated under adverse conditions, and eIF2α-phosphorylation acts as a

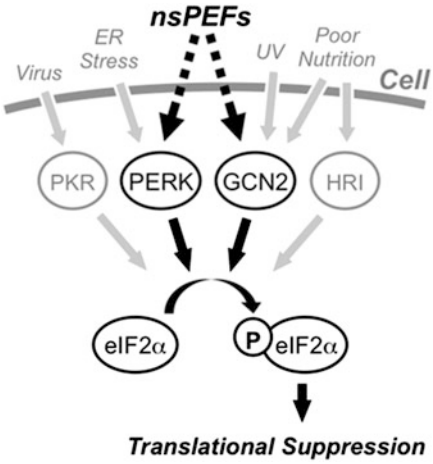

Fig. 4.22 Activation of stress responses by nsPEFs. Mammalian cells, including human cells, have four stress-responsive eIF2α-kinases, which are activated by different external stimuli. Among the four eIF2α-kinases, PERK and GCN2 are activated by nsPEFs and phosphorylate eIF2α, which further lead to translational suppression

convergence point for intracellular signaling activated by different forms of cellular stress. Furthermore, cells have a mechanism to recover from the translational suppression mediated by the phosphorylated eIF2α. GADD34 is a stress-inducible gene, and its transcript is translated by an alternative mechanism that is active even in the presence of the phosphorylated eIF2α. GADD34 protein forms a complex with protein phosphatase 1 and dephosphorylates eIF2α, leading to the restoration of protein synthesis [297].

4.8.3.2 Stress Responses Induced by nsPEFs

A recent study demonstrated that nsPEFs elicit stress responses in human and mouse cells [296]. Induction of stress responses requires relatively intense nsPEF conditions that cause growth retardation but not cell death. Under these conditions, eIF2α-phosphorylation is rapidly induced within a minute. In accordance with the induction of eIF2α-phosphorylation by nsPEFs, the rate of general protein synthesis is acutely decreased after nsPEF exposure. In addition to eIF2α-phosphorylation, the exposure to nsPEFs causes 4E-BP1 dephosphorylation, which is known to be a part of an eIF2-independent alternative mechanism for translational suppression [296]. The signaling pathway leading to 4E-BP1 dephosphorylation in nsPEF-exposed cells remains to be fully understood.

Concomitant with eIF2α-phosphorylation, PERK and GCN2, which are eIF2-α-kinases, are activated in nsPEF-exposed cells (Fig. 4.22). In double-knockout mouse embryonic fibroblasts that lack both *PERK* and *GCN2* genes, eIF2-α-phosphorylation by nsPEFs is significantly decreased, indicating that both kinases contribute to the nsPEF-induced eIF2α-phosphorylation. Single knockout of either *PERK* or *GCN2* has marginal effects on the nsPEF-induced eIF2-α-phosphorylation, suggesting the presence of functional compensation between PERK and GCN2 in nsPEF-induced stress responses [296].

PERK is known to be activated by ER stress, which is caused by unfolded proteins existing in the ER. GCN2 plays a critical role in the UV-induced stress response. The activation of PERK and GCN2 by nsPEFs raised the question whether nsPEFs activate the ER stress- and UV-induced pathways or whether nsPEFs act as a novel stress distinct from these cellular stresses. To clarify this point, activation of stress-specific gene expression was analyzed. ER stress generally leads to increased expression of specific genes, including *CHOP* and *BiP*. UV irradiation causes changes in gene expression, such as *GADD45β*. Increased expression of these stress-inducible genes is indicative of the activation of downstream events in the ER stress- and UV-induced pathways. However, quantitative RT-PCR analysis showed no increase in the expression of these genes after nsPEF exposure. Thus, despite the activation of PERK and GCN2, nsPEFs do not activate the canonical signaling pathways for ER stress and UV-induced stress and appear to act as a novel form of cellular stress [296].

4.8.4 Future Perspective

Recent studies have demonstrated that human cells respond to nsPEFs by activating multiple intracellular pathways, but important questions remain to be answered. First, the most upstream event(s) triggered by nsPEFs in each pathway is largely unclear, especially in the activation of MAPK pathways. Regarding the stress responses, nsPEFs seem to directly affect PERK and GCN2 molecules because there is no protein upstream of these eIF2α-kinases in their signaling pathways. However, molecular details of direct effects of nsPEFs on the PERK and GCN2 molecules should be understood. Second, how Ca^{2+} influx caused by nsPEFs is converted to intracellular signaling events remains unclear. Calmodulin (CaM) is a ubiquitous protein and universally serves as an intracellular Ca^{2+} receptor among eukaryotes. Ca^{2+}-bound CaM can activate many proteins, including Ca^{2+}/CaM kinases that further transduce Ca^{2+} signals. Similar to many Ca^{2+}-dependent cellular responses, Ca^{2+} signaling elicited by nsPEFs appears to be mediated by CaM and its associated proteins, which will be experimentally confirmed in future. Finally, contributions of activated intracellular signaling events to cell survival and death should be understood. For example, stress responses are generally protective reactions, but their excess activation promotes cell death. MAPK pathways are known to be differently involved in the initiation of cell death in a cell type-dependent manner. A better understanding of the physiological significance of nsPEF-induced intracellular signaling events will provide a mechanistic basis for the medical application of nsPEFs.

4.9 Cell- and Tissue-Level Response to Irreversible Electroporation: Implications for Treatment Planning and Outcome

Robert E. Neal II, Suyashree Bhonsle, and Rafael V. Davalos

The manipulation of cellular transmembrane potential and induction of the electroporation response for irreversible electroporation (IRE) and other electroporation-based therapies (EBTs) can be correlated to electric field exposure, as well as several secondary pulse parameters. However, there are a number of considerations that must be identified and accounted for when designing and implementing IRE therapies in vivo. These relate both to the identity and nature of the cells within an electroporated region, as well as the structural environment of the tissue containing the cells. This section of Chap. 4 identifies some of the complex environments, as well as cell- and tissue-level responses that can alter electric field distribution and the concurrent localized response to IRE electric pulses.

4.9.1 Specific Pulse Protocol Considerations for IRE Therapy

While much of this chapter focuses on general aspects of cellular electroporation from the molecular to cellular scale, this section considers aspects of particular importance to IRE. A key consideration in this regard relates to the overall energy of a pulse protocol and its ability to result in effective cell death regions. Reversible electroporation therapies, such as electrogene transfer and electrochemotherapy, aim to maintain an overall cell exposure energy to induce sufficient electroporation to facilitate transport of their targeted macromolecule without killing the cell, which results in typical protocols utilizing approximately eight pulses delivered at rates between 1 Hz and 5 kHz [298–300]. However, IRE pulse parameters are designed to kill the cells in a tissue region while confining thermal effects to those below which would induce morbidity and damage to the sensitive structures within and around the IRE ablation zone.

IRE feasibility for therapeutic targeted ablation first showed clinically relevant lesions were attainable with basic protocols while maintaining thermal effects below those known to cause thermal damage to the tissue [301, 302]. Subsequent studies further showed that guided adjustment of pulse parameters could manipulate the thermal implications from IRE therapy as well as reduce the effective electric field threshold required to ensure cell death. Such means for altering cumulative energy of a pulse protocol to change the effective lethal electric field threshold, thermal effects, and overall tumor response includes the strength of the

pulse, use of additional pulses, and manipulation of pulse length [304–306]. Further evidence suggests a nonlinear response for the lethality of a pulse protocol that does not require additional energy, whereby altering the timing of electric pulses with a modulated pulse delivery regime may increase ablation zone and improves tumor response [303, 306, 307].

The thermal effects during multi-pulse IRE protocols have been determined experimentally and via numerical modeling. The goal of these studies was to delineate IRE cell death from the thermal damage that occurs when tissues are exposed to temperatures higher than their physiological norm for extended periods of time. It has been suggested that when the period of exposure is long, thermal damage can occur at temperatures as low as 43 °C [308, 309]. Although 50 °C is typically chosen, what is considered instantaneous thermal damage occurs as high as 83.6 °C (prostate) or 74.7 °C (liver) [310]. In order to assess tissue temperature, numerical models employ a modified Pennes' bioheat equation that includes the effects of blood perfusion and metabolism and an additional Joule's heating term to account for resistive heating [311–313], as defined in the equation:

$$\nabla \cdot (k \nabla T) + w_{\mathrm{b}} c_{\mathrm{b}} (T_{\mathrm{a}} - T) + q''' + \sigma |\nabla \varphi|^2 = \rho c_{\mathrm{p}} \frac{\partial T}{\partial t} \tag{4.8}$$

where k is the thermal conductivity of the tissue, T is the temperature, ρ_{b} is the blood density, w_{b} is the blood perfusion rate, c_{b} is the heat capacity of the blood, T_{a} is the arterial temperature, q''' is the metabolic heat generation, ρ is the tissue density, c_{p} is the heat capacity of the tissue and $\sigma |\nabla \varphi|^2$ is the heat generated due to the electric field, where σ is the electrical conductivity of the tissue and σ is the electric potential.

In regard to determining the outcome from elevated temperature effects, recent models utilize an Arrhenius-type analysis to assess thermal damage from the temperature distribution [314–317]. Numerical models for IRE that predict temperature changes have been validated from actual data and can therefore serve as a reference for appropriate treatment parameter selection to minimize thermal effects while retaining sufficient IRE exposure [318, 319]. Experimental work performed that physically recorded measured temperatures during IRE treatments shows effective ablations without significant thermal effects [314, 320]. Importantly, in vivo and clinical studies show that IRE's nonthermal mechanism of death helps preserve surrounding critical structures [321, 322].

For larger tumors or while dealing with tissues with higher electric field thresholds for ablation, stronger pulse protocols may be necessary to ensure complete tumor coverage. This correlates with higher voltages, larger pulse widths, pulse numbers, and insertions. In such cases, particular care must be taken to avoid significant thermal damage. Such approaches include reducing the pulse delivery rate or delivering small sets of pulses in a "phased" delivery approach around all pairs, allowing more time for conductive tissue cooling between each particular pair of electrodes [306, 307]. Additionally, proactive thermal countermeasures have been suggested, including using actively cooled electrodes, cooling patient baseline temperature, or cooling the region surrounding the target organ with hydrodissection.

4.9.2 *Heterogeneous Systems: Static and Dynamic Conductivity Environments and Their Effect on IRE Ablation Zone Distribution and Therapy Outcome*

After considering manipulation and determining appropriate secondary pulse parameters in IRE and EBT protocols, IRE ablation zones can be correlated with an effective lethal electric field threshold, which is unique to the tissue and selection of secondary parameters. As a result, electric field distributions, and their accurate prediction and understanding, play an important role in designing and implementing successful IRE therapies. The electric field relates to the governing equation:

$$\nabla \cdot (\sigma \ \nabla \Phi) = 0 \tag{4.9}$$

where Φ indicates the electric potential and σ represents the electrical conductivity. While electrode geometries and applied voltages will partially affect the electric field that a volume of tissue is exposed to, the electrical conductivity will also alter the electric field distribution. Thus, when heterogeneous distributions of electrical conductivity exist in the targeted tissue, both within and between different tissue types, electric field exposure will be different from an isotropic distribution, thus altering ablation zone shape and volume.

4.9.2.1 Effects of Heterogeneous Conductivity

Early numerical investigation into the effect of heterogeneous tissue distributions showed that when the electrodes delivering the electric pulses are placed around a volume of higher electrical conductivity, the voltage drop within that region is reduced, and this region is thus subjected to a reduced electric field [323], while the opposite was found for a lower conductivity central region. Many varieties of tumor, a common ablation target for IRE therapy, contain a relatively high cellular density and higher conductivity than surrounding tissues with more extracellular constituents, such as the connective and fatty tissue components implicated adjacent to breast cancer tumors. However, it was shown that by placing the energy delivery electrodes within the outer boundary of the more conductive region, the effect of decreased electric field distribution within a more conductive region is eliminated, and thus effective treatment of more conductive tumors is possible while maintaining thermal effects below those which induce patient morbidity [312].

4.9.2.2 Heterogeneous Environments In Vivo

Because heterogeneous electrical conductivity distributions have been shown to significantly affect electric field distributions and treatment zones, it is important to understand and consider environments where these effects may be most relevant. There are two conditions where heterogeneous conductivities are relevant at the tissue level. These include inherent heterogeneities relating to tissue structure and composition and induced heterogeneities that result from manipulation of the targeted region environment.

4.9.2.2.1 Inherent, Static Conductivity Heterogeneities

Relevant inherent tissue heterogeneities include highly localized effects, such as those due to the presence of diverse interstitial constituents, including macro- and microvasculature, connective tissue, general cellularity, cellular morphology, and discrete functional organ units, such as the proximal convoluted tubules or glomerular capsules within the kidney. It is typically regarded as overly cumbersome to consider all of the subcellular to cellular-level variability within a targeted environment, and thus effective bulk tissue conductivity is used as a metric to approximate the overall conductivity for a particular tissue type. This bulk electrical conductivity variation for different tissue types may more readily be discretized and regarded separately in predictive EBT simulations. Certain tissues may contain stochastic or organized aspects that will have varying extents of an effect on electric field distributions, including the presence of randomly distributed calcifications, and structural tissue orientations that exhibit anisotropic effects to electric field distribution. While anisotropy will occur for several tissues, the strongest effect is clearly documented in muscle tissue, where the high conductivity along muscle fibers compared to perpendicular to muscle fibers imparts a strong effect on electric field distribution and ablation shape [324–326].

In addition to inherent variability in tissue conductivity distributions, there are numerous potential intervention-related changes to conductivity that may occur due to the presence of implanted materials or secondary therapy demands. Metallic objects will behave as high-conductivity spots within the tissue, which can serve as conduits for electric current, altering electric field distributions. In addition, greater electrical conductivity results in increased Joule heating from the electric pulses and will serve as localized regions of increased thermal effects. This effect correlates with the intervention type and tissue. It was shown that the presence of small metallic objects, such as brachytherapy seeds, may not induce significant alterations to bulk electrical conductivity, electric field distribution, and thermal effects [327]. However, the relative effect to the heterogeneous environment will increase with the total relative amount of metallic object, and caution should remain warranted for larger metallic objects in the vicinity of EBTs [324], such as stents, biomechanical correction hardware, or pacemakers. Nonmetallic implants and

devices will serve as low-conductivity regions in the tissue, overall likely evoking less significant alterations of EBT outcomes overall. Finally, intervention-related alterations to tissue properties may include the infusion of conductivity-altering fluids, such as saline or low-conductivity buffers. These solutions may be intentionally infused into the targeted or adjacent tissue or may occur as secondary means to delivering IRE therapy, such as hydrodissection. The alteration of osmolarity and conductivity of tissue from infused fluids should be carefully considered for their effect on EBTs. For example, high-conductivity saline within the targeted region will substantially increase bulk tissue conductivity, resulting in higher electric current and thermal effects.

4.9.2.2.2 Therapy-Induced Dynamic Electrical Conductivity Considerations

While inherent tissue heterogeneities will have a varying cumulative effect on electric field distributions and affected EBT volumes, it is also critical to consider dynamic changes to tissue properties that occur in response to the pulsed electric fields. This includes increases to electrical conductivity due to temperature rise from Joule heating. Further, it includes changes from electroporation-induced effects, where electroporated cells in a region no longer serve as dielectrics in the tissue, permitting improved electrolyte mobility within the environment and thus increased conductivity (Fig. 4.23). Such effects are pronounced, nonlinear, and highly dependent on local electric field intensity.

Thermal effects on mammalian tissue electrical conductivity are well documented and typically result in increases of 1–3 % per degree Celsius (known as temperature coefficient) [328]. Values of temperature coefficients for different tissues are given in Table 4.1. In an ex vivo study, it was shown for a typical clinical IRE pulse protocol that nearly all of the cumulative inter-pulse rise in electrical

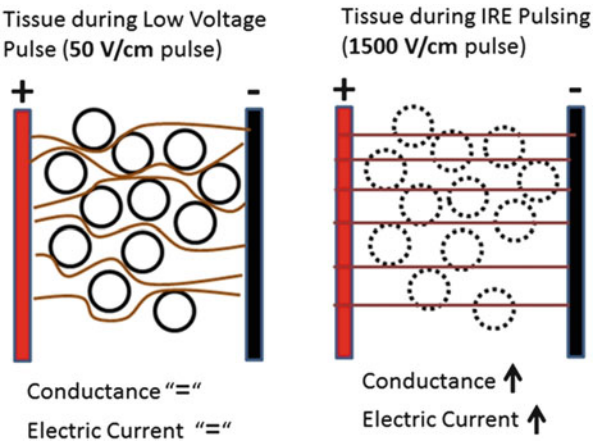

Fig. 4.23 Behavior of electric current pathway through cells in tissue without (*left*) and with (*right*) electroporation occurrence

Table 4.1 Change in electrical conductivity of soft tissue with temperature

Tissue	Temperature coefficient $\left(\frac{\Delta\sigma}{\sigma}\right)\left(\Delta T^{-1}\right)100\ \%^{\circ}C^{-1}$	Reference
Brain, cow, pig	3.2	[328, 330]
Kidney, cow, pig	1.7	[328]
Liver, cow, pig	1.5	[328]
Pancreas, cow, pig	1.4	[328]
Spleen, cow, pig	1.0	[328]
Breast tumor, rat	1.45	[331]

conductivity during pulse delivery may be accounted for by considering thermal effects [329]. For pulse protocols with modest temperature rise, thermally induced increases in electrical conductivity are relatively mild, and the dominant consideration is the electroporation-induced effects on electrical conductivity.

Electroporation-induced dynamic tissue conductivity plays a significant role in redistribution of electrical conductivity and thus the electric field and ablation zone. When cells become electroporated, their capacity to behave as a dielectric is compromised, thus facilitating improved electric current flow through cellular regions relative to non-electroporated tissues. It has been shown in several studies that tissue typically exhibits increases in effective bulk tissue conductance of two to five times and even up to 1000 times depending on the tissue type and protocol strength [332–334]. A study using ex vivo porcine renal cortex core samples pulsed with IRE using plate electrodes showed that the increase in electrical conductivity is directly correlated with intensity of electric field exposure, with the increase plateauing at approximately 2000 V/cm [329]. Such electroporation-induced increases in conductivity can be regarded as increasing from a baseline conductivity with no electroporation, σ_0, up to a maximum, σ_{max}. The maximum conductivity, σ_{max}, occurs when the cellular membranes no longer restrict the extent of interstitial electrolyte mobility. It was found that the increase in bulk tissue conductivity was best approximated with an asymmetrical sigmoid Gompertz function, calculated as

$$\sigma_G(|E|) = \sigma_0 + (\sigma_{max} - \sigma_0) \cdot \exp[-A \cdot \exp(-B \cdot E)] \tag{4.10}$$

where A and B are unitless coefficients that vary with pulse length, t(s). For a 100-μs long pulse, it was found $A = 3.053$ and $B = 0.00233$ [329]. The shape and behavior of this function can be found in Fig. 4.24.

The ex vivo study determined an equivalent circuit model representing cells and tissue undergoing electroporation can include a variable electroporation-based resistor, which varies with extent of electric field exposure. Additional examination of the equivalent circuit model suggests that the σ_{max} value for any particular tissue may be approximated by equating complete dielectric breakdown of all cell membranes in electroporated tissue to that of the membrane dielectric breakdown encountered when subjected to *β-dispersion* AC frequencies, which represent the range of frequencies where interfacial polarization of the lipid bilayer occurs.

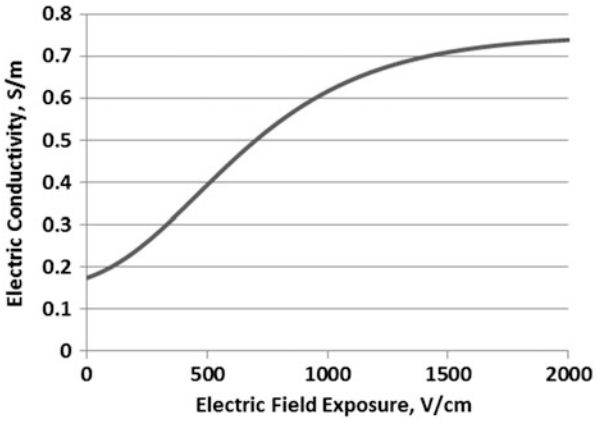

Fig. 4.24 Chart of $\sigma_G(|E|)$ function

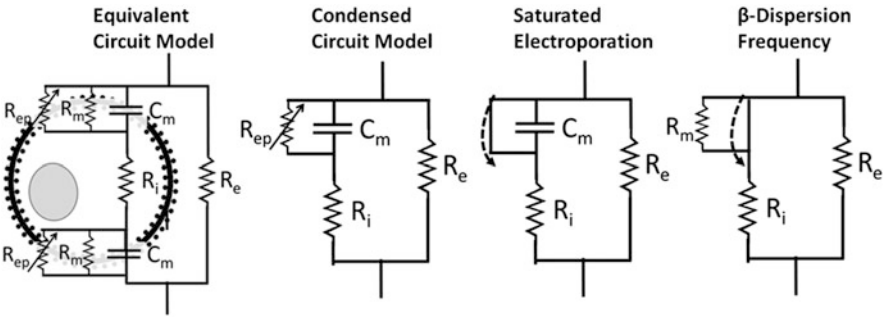

Fig. 4.25 Equivalent circuit model and response to varying electrical parameters. The lipid bilayer for a cell in suspension behaves as a membrane resistance, R_m; a variable electroporation-related resistance, R_{ep}; and a capacitor, C_m, in parallel relative to the extracellular resistance, R_e, and intracellular resistance, R_i. The high membrane resistance can be ignored, resulting in a condensed circuit model. When the electric field is of sufficient strength to induce a saturated amount of pores, the variable resistor behaves like a current shunt. Equivalently, when the frequency of an AC signal is in the β-dispersion range (200–500 MHz), the capacitive element behaves as a current shunt

In this range of frequency, the reactance of the membrane capacitance behaves as a short circuit to membrane resistance, thus providing an upper threshold for effective bulk tissue conductivity with fully saturated electroporation of the cells (Fig. 4.25).

4.9.2.2.3 Confirmation of Dynamic Conductivity Improved Numerical Simulation Accuracy

While it is well determined in the literature that electroporation-induced conductivity changes occur in tissue in response to electroporation pulses, it is further

detailed that accounting for these effects in numerical simulations of electric field distributions results in improved predictions of EBT procedure outcomes. Consideration of dynamic electrical conductivity from electroporation increases the tissue conductance and thus simulated electric current, matching experimental findings. It also preferentially grows the lesion height dimension perpendicular to electrode pair orientations relative to the width dimension between the electrodes. This change in shape offers a more accurate depiction of true lesion shapes found from in vivo IRE ablations. For instance, it was shown using potato tuber that electric current and affected volume shape were better approximated with numerical simulations that used dynamic conductivity [335]. It was also shown that dynamic electrical conductivity simulations resulted in improved predictions of electric current than static models in animal tissue [336]. In an additional study, the effect of numerical models with dynamic conductivity using the asymmetrical Gompertz function was compared with one using linear dynamic and static electrical conductivity. It was shown using in vivo canine renal ablations with clinically relevant pulse protocols that the Gompertz function produced the best approximations of lesion shape and electric current, while linear dynamic conductivity simulations also offered markedly improved correlations to ablation shape and electric current relative to static conductivity models [337].

4.9.3 Cell- and Tissue-Specific Susceptibility to IRE Electric Pulses

While extensive evidence exists indicating that alterations to secondary pulse parameters (pulse length, pulse number, modulated pulse delivery) may manipulate the effective electric field threshold required to induce IRE cell death, it should also be considered that different cell varieties and the structural arrangement of different parenchymal and pathologic tissues will exhibit unique susceptibilities to IRE electric pulses.

4.9.3.1 Cell-Specific Susceptibility

In regard to cell-level differences in IRE pulse susceptibility, heterogeneous cell and functional unit distributions have shown distinct lethal electric field thresholds. One consideration is the size of cells in a targeted region, since calculations show that larger cells will experience larger transmembrane voltage change for a given electric field exposure, and thus increased likelihood of electroporation induction [338]. In addition, a veterinary clinical study showed complete destruction of all tumor cells in a targeted region, while the immediately adjacent muscle cells were able to recover from the electroporation pulses [339].

Furthermore, two in vivo renal ablation studies showed a penumbra ablation zone of varying cell deaths outside the region of complete cell ablation, but proximal to the region where no IRE cell death was observed [337, 340]. This penumbra region contrasts with the sub-millimeter demarcation between completely dead and completely viable cell regions found in liver ablations [302]. This difference may be because liver tissue is a relatively isotropic and homogeneous distribution of functional units composed primarily of hepatocytes. The penumbra transition zone of heterogeneous cell death distributions in kidney indicated viability may directly relate to the tissue functional unit variety, where viability was found in progressively lower electric fields for blood vessels and glomeruli, distal convoluted tubules, and proximal convoluted tubules. Interestingly, the transition of viability with structure variety seemed to correlate with metabolic demands of the cells in each structure, suggesting that more metabolically active cells are less resilient to the electroporation-induced cellular stresses. Such a behavior may have implications in tumors, which contain neoplastic cells that are very metabolically active.

4.9.3.2 Organ-Specific Susceptibility

While different cells within an organ appear to show a variation in their effective lethal electric field threshold for a given pulse parameter algorithm, several studies have characterized the unique effective thresholds for different organs by simulating electric field distributions relative to in vivo ablation studies (Table 4.2). In [318], brain lesions were found to correlate with an electric field of 502 V/cm for 90 pulses, each 50-μs long, delivered at 4 pulses per second. This value is relatively similar to a threshold of 575 V/cm determined for renal cortex from a protocol of 100 pulses, each 100-μs long delivered at a rate of 1 pulse per second and simulated

Table 4.2 Electric field thresholds of cell death determined for different parameters and tissue types

Organ	Parameters	Electrical conductivity model (static vs. dynamic)	Average electric field threshold of cell death (V/cm)	Reference
Brain, dog	50-μs, 90 pulses, 4 Hz	Dynamic	502	[319]
Kidney, dog	100-μs, 100 pulses, 1 Hz	Dynamic	575	[337]
Liver, rabbit	100-μs, 8 pulses, 1 Hz	Static	637	[341]
Liver, rat	20 ms, 1 pulse	Static	400	[302]
Pancreas, pig	70-μs–100-μs, 70–90 pulses	Static	>650	[342]
Prostate, human, dog	70-μs–100-μs, 90–100 pulses, 1 Hz	Dynamic	1072	[322]
Mammary tumor, rat	100 μs, 100 pulses, 0.33 Hz	Static	1000	[325]

using the Gompertz sigmoid dynamic conductivity [337]. This is also similar to the threshold of 637 V/cm in the liver tissue using static conductivity simulations for a protocol of 8 pulses, each 100-μs long delivered at a rate of 1 Hz [341], since consideration of dynamic electrical conductivity facilitates reduced calibrated electric field thresholds. Similarly, pancreas simulation calibrations found an effective electric field threshold of below 650 V/cm [342]. A notable exception is the prostate, where an electric field threshold of 1072 V/cm was determined from healthy prostate ablations in canines 6 h post-IRE and human lesions 3–4 weeks post-IRE using protocols of 70–100 μs with 90–100 pulses delivered, delivered at an ECG synchronous rate [322].

When exhibited, variability in IRE threshold may depend on the cellular constituents within an organ and their unique metabolic demands. Further, it may result from differences in interstitial components in the tissue altering electrical conductivity and electric field distributions. For instance, tissues that are highly calcified, contain extensive fibrous components, or exhibit glandular organization with low-conductivity surrounding membranes may induce significant voltage drop across these low-conductivity regions, thus reducing electric field exposure to the cells.

4.9.4 Conclusion

Cellular response to pulsed electric fields includes the development of reversible and irreversible electroporation defects in the cell membrane. The type and extent of these effects will vary with secondary pulse parameters that alter the total effective strength of an electroporation pulse protocol. Several cellular- and tissue-level aspects must be considered in relation to accurately predicting outcomes for electroporation therapies, including cell variety and distribution, organ, tissue properties, and the explicit pulse parameters used. When all secondary parameters are reasonably consistent, the effect can be directly correlated to electric field exposure. Thus, electric field distribution is often used as a surrogate to predict and identify affected regions of tissue in EBTs. When planning and implementing therapeutic IRE ablation procedures and other EBTs, it is vital to consider the effects of complex environments, including heterogeneous systems, which will alter the conductivity and electric field distribution in the tissue. These aspects include inherent conductivity heterogeneities between different tissue types, the composition of tissue constituents, and any prior intervention-related implants or manipulations of tissue. In addition, electroporation procedure delivery will also alter tissue properties, via thermal effects as well as electroporation-induced changes to tissue conductivity. Consideration of these dynamic effects and general tissue heterogeneities are important for creating accurate predictive models and determining optimally effective electroporation procedure protocols.

4.10 Nanosecond Pulsed Electric Field-Induced Cell Death Responses and Mechanisms

Stephen J. Beebe

4.10.1 Introduction

Life is not possible without death; they go hand in hand, like a coin with two different sides. Cell death occurs by a number of different mechanisms during development and throughout life. Very generally, cell death can be divided into two general categories. Accidental cell death (ACD), caused by severe physical, chemical, or mechanical insults that result from immediate structural breakdown, is not compatible with life and cannot be prevented by genetic or pharmacologic intervention of any kind. This was often called necrosis, but as will be seen, this term for ACD is no longer adequate. The term necrosis was used by Virchow in 1858, when histological stains and microscopy were not available, to mean an advanced stage of tissue breakdown, similar to what we would now call gangrene [343]. In contrast, regulated cell death (RCD), be it apoptosis or necrosis, can be triggered by exogenous stimuli and is genetically coded molecular mechanisms and can be pharmacologically and genetically modulated. These regulated processes occur during microenvironmental distresses, pre- and postembryonic development, tissue homeostasis, and immune responses [344]. Events within these RCD mechanisms are those that are part of completely genetically coded physiological programs such as (post)-embryonic development or the protection of tissue homeostasis. These are referred to as programmed cell death (PCD) mechanisms. To be clear, these instances of PCD are by definition regulated, but RCD mechanisms are not necessarily PCD ones [345].

Kerr and colleagues recognized a stereotyped form of cell death and called it apoptosis taken from the Greek meaning “falling off” as autumn leaves from trees. It was strictly characterized morphologically by cytoplasmic shrinkage, chromatin condensation eventually involving the entire nucleus, nuclear fragmentation, cell blebbing or a “boiling-like” process, and formation of apoptotic bodies [346]. In *Caenorhabditis elegans*, apoptosis was the first form of PCD to be characterized and was found in mammals to be highly conserved, but during evolution had evolved much more complex mechanisms at each step along the pathway. This indicates the development of redundancy and specialization of apoptotic mechanisms in higher organisms [347, 348]. Evidence now indicates that cell death as necrosis and apoptosis is an oversimplification and that there are multiple RCD programs that overlap, but are mutually exclusive with apoptosis [347]. Within the

cellular morphological phenotypes described by Kerr and colleagues are diverse functional, biochemical, and immunological processes. Furthermore, morphological and biochemical markers are not necessarily linked [349].

Programmed cell death is well characterized during embryonic development as apoptosis, which plays important roles in shaping organisms. As examples, the tadpole loses cells in its tail by apoptosis as it morphs into a frog. Hands initially appear as tiny buds where apoptosis takes place in interdigital cells or "webs" between fingers in order to separate them from each other. Likewise, the lens of the eye is crafted by cell proliferation, migration, and processes that use the same regulators of those in apoptosis [350]. Apoptosis also provides a mechanism for the safe disposal of potentially destructive inflammatory cells such as neutrophils that are phagocytized by local macrophages when they are no longer needed. There are approximately 2.5×10^{10} neutrophils in the human body at any one time that live several hours to a few days, so the turnover of these potentially dangerous cells is significant. During development and homeostasis such as maintenance of neutrophil numbers, PCD occurs with conservation of plasma membrane integrity and without an immune response. This prevents the release of proinflammatory mediators and protects surrounding cells and tissues [351]. However, it is now clear that apoptosis does not always take place in the absence of inflammation or the absence of an immune response. This will be reiterated later.

A Nomenclature Committee on Cell Death (NCCD) was formulated to describe and evaluate distinct modalities of cell death, make recommendation on their definition, facilitate communication among scientists, and accelerate the pace of discovery [349]. That the 2012 committee formulated several previous rounds of recommendations [352–354] and published again in 2014 [344] indicates the need for a flexible, yet consistent process for nomenclature as our understanding of cell death mechanisms progresses. The 2012 NCCD described 13 regulated cell death mechanisms. Since even a brief description of these RCD mechanisms is beyond the scope of this chapter, the focus here will be on RCDs that are most common and especially those that have been described in response to electric fields. These will include caspase-dependent intrinsic and extrinsic apoptosis by death receptors and dependence receptors, caspase-independent intrinsic apoptosis, necroptosis, and parthanatos (PARP-mediated RCD) as well as roles for autophagy in cell death. Other cell death mechanisms can be reviewed in [349].

Regardless of external or internal stresses that induce RCD, cell responses are tightly regulated and coordinated. Generally, responses to threatening stimuli are aimed to avoid or remove the stimulus, initiate repair mechanisms, and reestablish homeostasis [355]. If these stress-adaptive approaches fail, cells initiate RCD. In this transition, RCD-inhibitory signals terminate and are replaced by RCD-promoting signals. Alternatively, these two signaling mechanisms coexist as RCD-inhibitory signals dissipate and RCD-promoting signals increase until they become predominant [345].

Before cell death mechanisms and their specific components are introduced, it may be useful to describe one of the first nomenclature systems used; it will be seen in some earlier literature and presenting them will introduce some important

distinctions about RCD and what we have learned about them over time. One of the earliest cell death classifications included type 1 cell death as apoptosis, showing the morphological features described by Kerr et al. [346]; type II cell death as autophagy (self-eating), featuring cytoplasmic vacuolization for recycling cellular organelles; and type III cell death as necrosis, exhibiting neither apoptotic nor autophagic characteristics [356]. In practice, morphological characterizations of apoptosis are less valuable than initially appreciated. First, this classification system considered apoptosis as the only RCD mechanism known and necrotic cell death was defined as an ACD type, which is now known to be programmed. In addition, autophagy as a cell death mechanism has been considerably debated, but it is now considered as a cell death subroutine as opposed to a cell death mechanism on its own. Autophagy is a highly conserved, genetically programmed, integrated stress response whereby cells form intracellular membrane vesicles that engulf and degrade cytoplasmic organelles providing a survival advantage as cells undergo nutrient deprivation and other cellular stresses [357]. It is now also known that apoptosis and autophagy are not mutually exclusive pathways, but share some molecular regulators and can act in synergy or counter to each other [358]. Finally, pharmacological and genetic manipulations of cell death mechanisms can shift morphological markers from one morphologically defined cell death classification to another. Thus, *classification of cell death based on morphology has generally been abandoned in favor of classifications based on quantifiable biochemical parameters*. The NCCD defined molecular subroutines that characterize specific cell death mechanisms as well as pharmacological/genetic interventions that can be used to discriminate among them [349].

4.10.2 Regulated Cell Death (RCD) by Caspase-Dependent Mechanisms

Caspase 3-dependent cell death is generally considered to be apoptotic in nature and most generally exhibits classic apoptotic morphology defined by Kerr and colleagues [346]. This can occur by intrinsic apoptosis, which is initiated by intracellular stresses, or extrinsic apoptosis, which is initiated by extracellular death receptor signaling (FAS/CD95, tumor necrosis factor α (TNFα), and TNF-related apoptosis-inducing ligand, TRAIL) or dependence receptor signaling [netrin receptors such as patched, deleted in colorectal carcinoma (DCC) and UNC5A-D]. Increasing death receptor signaling increases cell death. In contrast, dependence receptors are only lethal when concentrations of their cognate ligands fall below a threshold level. Extrinsic apoptosis by dependence receptors expresses caspase 3 and caspase 9 through patched and DCC receptors or caspase 3 and activated protein phosphatase 2A (PP2A) and death-associated protein kinase 1 (DAPK1) through UNC5B receptors. Anoikis (ancient Greek for “the state of being homeless”) exhibits caspase 3 activation, but is executed by the molecular

mechanisms for intrinsic apoptosis as a response from cells that have lost cell-to-matrix interactions and β-1-integrin signaling and also express other distinguishing markers including downregulation of EGFR and inhibition of ERK1 signaling.

As mentioned earlier, genetic studies in *C. elegans* defines apoptosis as an evolutionarily conserved PCD pathway that is as fundamental to life as proliferation and differentiation. Studies in *C. elegans* provide the basis for understanding PCD in higher organisms that are referred to as apoptosis [359]. *C. elegans* is an excellent model for these studies because the history of every cell in the organism has been detailed. The male exhibits 1179 somatic nuclei and during development 148 undergo PCD. By using methods of genetics, developmental biology, molecular biology, and biochemistry, 13 genes have been identified that regulated PCD in *C. elegans*. All of these genes have several homologues in mammals. Mutations in many of these mammalian gene homologues cause diseases in humans [359]. This enhances the importance of understanding apoptosis mechanisms in humans.

The general strategy for regulation of PCD by apoptosis occurs when an antagonist (EGL-1, BH3-only protein) relieves inhibition of a repressor (CED-9, BCL-2/xl) that blocks a proapoptotic protein (BAX, BAK); in other words inhibition of an inhibitor induces activation (Fig. 4.26). This is analogous to releasing the cell death "breaks". In *C. elegans* this occurs when an apoptotic stimulus upregulates the transcription factor *egl-1*, a proapoptotic mammalian homologue BCL-2 homologue 3, called a BH3-only protein. EGL-1 binds to antiapoptotic CED-9, a mammalian BCL-2 homologue, which releases inhibition that CED-9 exerts on the adaptor protein CED-4, a mammalian homologue of apoptosis peptidase-activating factor 1 (APAF-1). This allows proapoptotic CED-4 to bind the cysteine protease CED-3, a mammalian caspase homologue. CED-3 cleaves multiple substrates and executes cell death.

In mammalian cells, the process is more evolved and complex in several ways, yet fundamentally the same. During evolution, genes were duplicated and selected to function in more complex multicellular organisms based on their environmental needs. A major outcome of gene duplication is specialization of function. This replication and complexity provides selective mechanisms to regulate apoptosis [347]. In mammals, there are several isoforms for all of the *C. elegans* apoptosis-related proteins at every step. These include three classes of BCL-2 family proteins that regulate outer mitochondrial membrane (OMM) integrity. Two classes include proapoptotic proteins BAX and BAK and antiapoptotic proteins BCL-2, BCLxl, BCLw, MCL1, and A1. Antiapoptotic proteins protect the integrity of the OMM by binding to proapoptotic proteins, which prevents them from permeabilizing the OMM that leads to caspase activation and apoptosis. The third class of BCL-2 family proteins includes proapoptotic BH3 only proteins that are subdivided into two groups based on their interactions with the other two classes of BCL-2 family members. Direct activators can bind to and inhibit antiapoptotic BCL-2 proteins as well as directly activate proapoptotic proteins (indicated in dotted line in Fig. 4.26). These include BID, BIM, and maybe PUMA. The other subgroup of proteins is sensitizers or derepressors that cannot directly activate the proapoptotic group, but bind to and inhibit the antiapoptotic proteins. These BH3-only proteins include

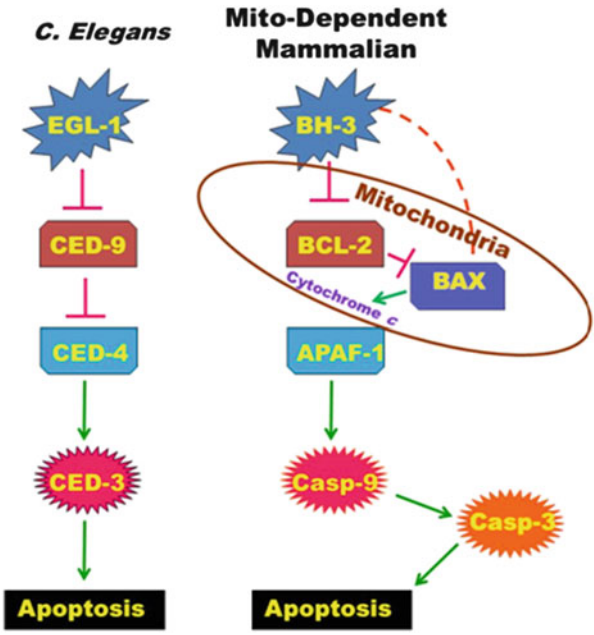

Fig. 4.26 A comparison of the primordial apoptosis pathways in C elegans (*left*) and more complex eukaryote/mammalian mitochondria-mediated apoptosis (*right*)

BAD, BIK, BMF, NOXA, and maybe PUMA. Some BH3-only proteins are further regulated by phosphorylation (BAD, BIK, BIM, BMF). Mammalian cells also express multiple caspase isozymes including initiator (caspase 8, 9, 10) and executioner (caspase 3, 6, 7) caspases as well as inflammatory caspases (caspase 1, 4, 5 in humans; caspase 1, 11, 12 in mice).

In mammalian cells, extrinsic apoptosis is induced by death receptor ligands or agonistic antibodies binding to their cognate death receptors, shown here with FAS ligand (FAS-L) and its receptor (FAS-R) (Fig. 4.27). After FAS ligand binding, intracellular signals are initiated by recruiting and anchoring FAS-associated protein with death domain FADD and caspase 8 to the cytoplasmic side of the transmembrane death receptor forming the death-induced signaling complex or DISC, which activates initiator caspase 8. Caspase 8 can now take either of two different pathways to activate executioner caspases depending on the cell type [360]. In type I cells such as thymocytes, the mitochondria-mediated intrinsic pathway is not used and caspase 8 directly activates caspase 3 (or other executioner caspases). In these cells there is ample formation of the DISC and enough caspase 8 is activated to directly activate caspase 3. This cascade cannot be inhibited by antiapoptotic proteins from the B-cell CLL/lymphoma 2 (BCL-2) family. An explanation for the efficient activation of caspase 3 in type I cells is the presence of FAS in membrane microdomains rich in cholesterol and glycosphingolipids called lipid rafts [361]. It is possible that lipid rafts form of a platform that allows efficient formation of the DISC and caspase 8 activation.

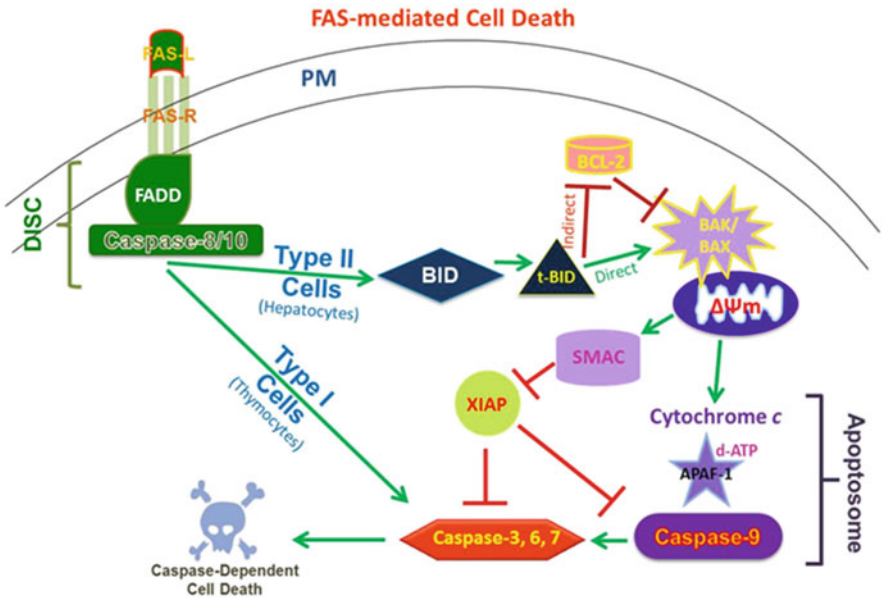

Fig. 4.27 FAS-mediated cell death in mammal. Cell death in higher organisms includes extrinsic apoptosis that is independent of mitochondria (type I cells) and signal amplification through mitochondrial mechanisms involved in intrinsic apoptosis (type II cells). *Green arrows* indicate activation. *Red* perpendicular lines indicate inhibitions. See the text for presentation and discussion

In contrast, for type II cells such as hepatocytes and pancreatic β-cells, activation of the DISC is insufficient to produce enough caspase 8 to activate caspase 3 and it is essential that the apoptotic signal is amplified through the mitochondria-mediated intrinsic pathway by caspase 8-mediated cleavage and activation of BH3-only protein BH3-interacting domain death agonist (BID) to form truncated BID or t-BID, which leads to cytochrome c release. These steps lead to creation of proteolipid pores that permeabilize outer mitochondrial membrane integrity by pore-forming proapoptotic proteins BCL-2-associated X protein (BAX) and BCL-2-agonist/killer (BAK). This cascade can be inhibited the by antiapoptotic BCL-2 family. Pore-forming activities of BAX and BAK are physically inhibited by interaction with antiapoptotic proteins BCL-2, BCL-2-like 1 (BCLxl), and myeloid cell leukemia (MCL1). In turn, the interactions of pro- and antiapoptotic proteins are under control of BH3-only proteins such as BCL-2-binding protein (PUMA), BCL-2-like 11 (BIM), and BID. Pore-forming proapoptotic proteins lead to the release of cytochrome c from mitochondria. Cytochrome c binds with APAF-1, deoxy-ATP, and caspase 9 to form the apoptosome to activate initiator caspase 9. Active caspase 9 then activates executioner caspase 3 to execute apoptosis and cell death [362]. Also released from mitochondria is second mitochondria activator of caspase (SMAC) (also called DIABLO), which facilitates apoptosis by inhibiting X chromosome-linked inhibitor of apoptosis (XIAP) and other IAPs that block

activation of caspase 3, 6, 7, and 9. Another explanation for the difference between type I and type II cells is levels of XIAP in FAS death receptor-stimulated cells, such that type II cells require amplification through t-BID to overcome XIAP inhibition by way of the mitochondrial pathway for caspase activation, while type I cells do not [363]. t-BID functions to amplify this response by directly activating BAK/BAX by oligomerization and/or indirectly activating it by relieving BCL-2 mediated inhibition of BAK/BAX. Figure 4.27 shows three activation mechanisms for caspases: direct cleavage as in caspase 8 and caspase 9 cleavage of caspase 3, induced proximity activation of caspase 8 at the DISC, and holoenzyme formation for activating caspase 9 at the apoptosome. Caspases carry out specialized function and distinct roles based on subcellular localization and protein–protein interaction with substrate specificity playing a lesser important role. This division of labor permits multicellular organisms to sense and differentially respond to diverse environmental stimuli [347]. For example, caspase 8 is localized near and binds to the cytoplasmic side of death receptors and upon death receptor ligand binding with FADD to form the death-induced signaling complex (DISC) initiating extrinsic apoptosis. In contrast, caspase 9 binds to APAF-1 to form the apoptosome with cytochrome c initiating intrinsic apoptosis. Intrinsic apoptosis is activated by a number of intracellular stresses such as DNA or organelle damage, Ca^{2+} overload, hypoxia, oxidative stress, intracellular pathogens, increases in unfolded proteins, and excitotoxicity in neurons, among others. All of these diverse stimuli are connected to mitochondrial mechanisms. So, intrinsic apoptosis is initiated through mitochondria-mediated events that include cytochrome c release, APAF1-dependent activation of caspase 9 and caspase 3. Classification of initiator and executioner caspases is important to differentiate initiation of RCD (in this case apoptosis) and its actual execution [345, 364, 365]. In response to these same apoptosis initiators, caspase-independent processes also occur when apoptosis-inducing factor (AIF) and endonuclease G are released from mitochondria and translocated to the nucleus to degrade DNA.

Other complexities in RCD occur because FADD has multiple functions through its death effector domain (DED) and its death domain (DD) [366]. In addition to forming the DISC using its DD to bind to the cytoplasmic domains of the FAS receptor and using its DED to bind pro-caspase 8/10, FADD can also form complex II, which does not include the FAS receptor, but includes FADD, pro-caspase 8, and c-FLIP, which appear to amplify caspase activation. c-FLIP binding to the FADD DED signals proliferation and survival. FADD also forms complexes in TNF-R1 signaling that promotes either survival or apoptosis. The DD of FADD also binds Atg5 that promotes autophagy and RIP1 that induces necroptosis, another type of RCD (discussed later). Thus, the FADD DED and DD domains regulate many essential cell processes at the crossroads of survival and death by apoptosis or programmed necrosis.

Until recently, necrosis was considered accidental cell death with morphological characteristics that were neither defined as apoptosis nor autophagy, called type III cell death. As indicated earlier, apoptosis is not the only mechanism of cell suicide or RCD. It is now known that necrosis can also be regulated and occurs without

caspase activation. Programmed necrosis is distinctly different than apoptosis and may operate as a backup system when apoptosis mechanisms collapse such as with viral infections that express caspase inhibitors or when apoptosis programs are inhibited in cancer. Necrosis exhibits morphological characteristics and has been defined in several pathological conditions. As opposed to apoptosis, in regulated necrosis, cells and organelles swell, nuclei remain intact, the nuclear membrane dilates, chromatin condenses into small, irregular blotches, DNA is randomly degraded, and cells do not fragment to form apoptotic bodies.

Regulated necrosis is not one signaling cascade, but appears to be interactions among multiple molecular events from more than one signaling pathway. However, it is difficult to define and characterize these mechanisms and pathways without knowing the initiators, propagators, and executioners in the processes. Analyzing the final characteristics does not does not indicate which pathways were executed. Nevertheless, significant progress has been made to delineate some of these events and has demonstrated their importance in both physiological and pathological processes. Programmed necrosis is responsible for negative selection of lymphocytes, termination of immune responses, regulation of bone growth, ovulation, cellular turnover in the intestine, or post-lactational regression of the mammary gland. It also has pathological correlates in neurodegeneration, excitotoxicity, stroke and ischemia–reperfusion, infection, and oxidative stress [367, 368]. However, there is more to learn about these mechanisms and in time they will be as well defined as apoptosis mechanisms and pathways.

4.10.3 RCD by Necroptosis

One subroutine of programmed necrosis that is well characterized through death receptors is necroptosis [344, 345, 347, 369]. Necroptosis can be induced by death receptors (FAS, TNFR, TRAIL) and pathogen recognition receptors (PRRs) on their plasma membranes that respond to molecules with pathogen-associated molecular patterns (PAMPs) such as viral or bacterial nucleotides, lipopolysaccharides, and lipoproteins that induce inflammation. Biochemical markers for necroptosis are best categorized from responses produced by tumor necrosis factor receptor (TNFR) when caspases are inhibited. Complexes in response to TNFR can induce survival, apoptosis, or necroptosis. Upon TNF ligand binding, an intracellular assembly called complex I is formed at the cytoplasmic side of the receptor by TNFR-associated death domain (TRADD), receptor-interacting protein kinase 1 (RIP1), cellular inhibitor of apoptosis protein (cIAP), and TNFR-associated factor 2 (TRAF2) and TRAF5. If cIAP-mediated ubiquitylation of RIP1 predominates over de-ubiquitylation by cylindromatosis, ubiquitinated RIP1 recruits transforming growth factor β–activated kinase (TAK1) and TAK1-binding protein 2 (TAB2) and TAB3 and Nf-kB is activated to promote inflammation and survival. If de-ubiquitylation predominates, cell death is induced by one of two different assembles called complex II. One complex II induces apoptosis by activating

caspase-8 in the DISC. The other is similar to that shown in Fig. 4.27 for the DISC, except TRADD, RIPK1 and RIPK3 are present with FADD and caspase 8 cleaves and inactivates RIP1 and RIP3 to induce caspase-dependent apoptosis. If caspase 8 is inhibited, RIP1 and RIP3 become auto- or cross-phosphorylated (or by an unidentified kinase) and induce necroptosis. Necroptosis can be considered to be RIP3 dependent. This assembled complex II is called the necrosome, and it activates several bioenergetic changes, elevates reactive oxygen and nitrogen species, produces ceramide, induces lipid peroxidation, opens the mitochondria permeability pore complex, elevates intracellular calcium, and causes DNA damage and PARP-1 activation, ATP and NAD depletion, activation of calpains and cathepsins, and feedforward signaling loops that cause an energy crisis and cell death. The switch that modulates the apoptosis/necroptosis cell death scenarios is regulated by initiator caspase 8 and the ubiquitylation system. Necroptosis is pathologically relevant in defense of pathological organisms and conditions causing excessive loss of cell viability including ischemia–reperfusion injury, chronic neurodegenerative diseases, acute neurotoxicity, sepsis, and pancreatitis [345].

4.10.4 RCD by Parthanatos (PARP-1-Mediated RCD)

It has been debated whether there is one core program for regulated necrotic cell death or if there are distinct individual programs. Recent studies suggest that the necroptosis program described above is actually two separate pathways that can be activated independently. In this model, PARP-mediated cell death appears to occur with excessive DNA damage and overactivation of poly (ADP ribose) polymerase-1 (PARP-1). While PARP-1 is a molecular sensor of DNA strand breaks under normal conditions and is cleaved and inactivated by caspase 3 during apoptosis, hyperactivation leads to oversynthesize branched, long poly (ADP ribose) (PAR) chains attached to glutamate or aspartate residues of acceptor proteins. This leads to genotoxicity and mitochondriotoxicity causing irreversible loss of $\Delta\Psi_m$ and AIF release from mitochondria. This leads to excessive hydrolysis of NAD+ into nicotinamide and PAR and ATP hydrolysis causing a dramatic energy crisis and caspase-independent cell death. PAR is a common marker for PARP-mediated cell necrosis, which is also called parthanatos. H_2O_2 and DNA-alkylating agents induce cell death by PARP-1. RIP1 and TRAF appear to be downstream mediators required for JNK activation that leads to activation of calpains and cathepsins and compromise outer mitochondrial membrane integrity and release of AIF. It is likely that the ROS generated by necroptosis causes DNA damage and activation of PARP-1 and downstream processes that are characterized as PARP-mediated programmed necrosis. Thus the PARP-mediated pathway can be considered part of the TNF necroptosis pathway, but can function independently of it.

PARP-1-dependent cell death induces inflammation in cells in the nervous, cardiovascular, and immune systems. Inhibition of necroptosis by blocking RIP1 and inhibiting PARP-1 lowered ischemia–reperfusion damage after stroke. PARP-1

inhibitors have also been effective in treating tissue injury in response to septic and hemorrhagic shock, as well as acute lung inflammation, peritonitis, and acute forms of cardiomyopathies and heart failure. Inhibiting PARP-1 may also be effective in autoimmune diseases such as type I diabetes and rheumatoid arthritis [369].

4.10.5 Nanosecond Pulsed Electric Fields Activate RCD

Some initial studies investigating nsPEF effects on mammalian cells were basically extensions of studies using pulse power to decontaminate or kill bacteria [370]. Given that nsPEFs could kill bacteria, it was likely that they could induce cell death in cancer cells, perhaps by RCD. In the mid-to-late 1990s, mechanisms for regulated or programmed cell death, commonly referred to as apoptosis, were being defined at a rapid pace and disease-causing mutations in apoptotic proteins had been defined. At this time, apoptosis was the only known form of RCD. Thus, nsPEF-treated cells and tumors were analyzed for apoptotic characteristics in cells in vitro and tumor tissue in vivo. Essentially all studies with nsPEF demonstrated RCD mechanisms because cell death was delayed and ACD was not observed or not reported. Also of interest was defining cellular targets that were sensitive to nsPEFs. Generally, these included the plasma membrane, nucleus, DNA, mitochondria, and cytoskeleton.

4.10.6 In Vitro Studies Showing nsPEF-Induced RCD

Caspase activation and other markers for apoptosis have been shown in vitro in human Jurkat and HL60 cells [147, 233, 238, 371], Jurkat and rat glioma cells [372], HCT-116 cells with and without p53 [373], B16f10 cells [374], E4 squamous cell carcinoma cells [375], and several hepatocellular carcinoma cell lines [376], among others.

NsPEF-induced alterations in asymmetrically located plasma membrane lipids have also been used as an apoptosis marker, but there are some special considerations using this as a cell death marker. Phosphatidylcholine and sphingomyelin are predominantly located in the outer (luminal) leaflet. Phosphatidylethanolamine and phosphatidylinositol reside mainly in the inner (cytoplasmic) leaflet, while phosphatidylserine (PS) is located almost exclusively in the inner leaflet [377]. Externalization of PS to the outer leaflet of the plasma membrane is generally considered to be an apoptosis marker. Although externalization of PS can be context dependent, it does require caspase-mediated cleavage and inactivation of cell flippase(s), which transports PS from the outer to the inner leaflet [378]. It was shown that nsPEF-induced PS externalization was at least partially caspase dependent [390]. Factors released from mitochondria have also been implicated in the activation of lipid scramblases resulting in bidirectional lipid scrambling that

disrupts the asymmetric distribution of PS [377]. Finally, the transmembrane protein Xkr8 promotes caspase-dependent PS exposure during apoptosis, probably acting at a late step in PS exposure, possibly in phospholipid scrambling [379]. This is sufficient to serve as an "eat-me" signal and engulfment by macrophages. However, electric fields can "pull" PS by electrophoretic migration from the inner leaflet to the outer leaflet of the plasma membrane through nanometer-sized electropores induced by pulses as short as 3 ns [380]. Furthermore, these cells can be phagocytized as apoptotic mimicry [381]. In this context, PS externalization is not an apoptosis marker and is reversible. Also parthanatos, which will be presented later, also shows externalization of PS [382]. Thus, using PS externalization as an apoptotic marker in response to nsPEFs requires caution and should only be used at times significantly after pulse application and supported by other apoptosis markers. For example, the demonstration that caspases are activated and that nsPEF-induced PS externalization is attenuated by the caspase inhibitor z-VAD-fmk satisfies this criterion for using PS externalization as an apoptosis marker [390].

Detection of DNA fragments using terminal deoxyribonucleotidyl transferase (TDT)-mediated dUTP-digoxigenin nick end labeling (TUNEL) assay has often been used as an indicator of apoptosis. However, a number of studies indicate that TUNEL-positive cells can occur in other forms of nonapoptotic cell death. For example, TUNEL-positive cells have been identified in a number of pathological conditions that cause necrosis [383–385]. The TUNEL assay does not discriminate among apoptosis, necrosis, or autolytic cell death [386] and therefore should not be used alone as an apoptotic marker. In general, multiple markers should be used to identify cell death by apoptosis.

Other nsPEF-induced indicators apoptosis include morphological changes such as cell shrinkage, membrane blebbing and DNA fragmentation, but more recent data indicate that these may not be specific to apoptosis [344]. Other markers such as changes in BCL-2 family proteins can be suggestive of apoptosis, but are not indicative. In addition to caspase activation, PARP cleavage and cytochrome c release into the cytoplasm have been used as a valid apoptosis marker.

After the initial studies by Beebe [233, 238] and Vernier [372] and colleagues, several other studies provided additional evidence for nsPEF-induced apoptosis; however, based on other observations, it appeared that that other RCD mechanisms were likely present. In $p53^{-/-}$ and $p53^{+/+}$ human HCT-116 colon carcinoma cells treated with lethal, square wave nsPEFs (50 pulses, 1 Hz, 60 ns 60 kV/cm or 5–30 pulses, 1 Hz, 60 kV/cm) [373], cell shrinkage was observed in cells with the presence of active caspases occurring before increases in BAX and cytochrome c release. Caspase activation could have occurred without mitochondrial involvement, which would implicate the extrinsic pathway like that in type I cells. Since no major differences in cell death mechanisms were observed in cells that did or did not express p53, cell death by nsPEF does not require p53.

Murine B16f10 melanoma cells treated with nsPEF (1–10 pulses, 1 Hz, 300 ns, 12–60 kV/cm) also expressed some apoptosis indicators in an electric field-dependent manner, cell shrinkage, membrane blebbing, and active caspases, but

other apoptosis markers were absent [374]. Increasing numbers of cells exhibited loss of $\Delta\Psi_m$ and increases in ADP/ATP ratio were observed, which would cause mitochondria to swell, rupture, and cytochrome c, AIF, or SMAC release, which were not observed. Interestingly, dying cells did not exhibit PS externalization. Degradation of the actin cytoskeleton indicated the cells were undergoing disassembly. While apoptosis appeared to be present, it is likely that other RCD mechanisms were operating.

In E4 squamous cell carcinoma cells treated with lethal nsPEFs (10 pulses, 1 Hz, 300 ns 10–60 kV/cm) [375], electric field-dependent appearances of RCD indicators provided insight into death mechanisms. Caspase activation and PS externalization could be seen at lower electric fields than decreases in $\Delta\Psi_m$ and release of cytochrome c, suggesting an extrinsic mechanism for caspase activation without mitochondrial involvement. Consistent with this was the finding that decreases in BID, increases in t-BID, and release of cytochrome c were caspase dependent. Calcium-sensitive calpain(s), which can be stimulated in some apoptosis pathways [387], was also shown to be activated. BID cleavage was sensitive to a calpain inhibitor (and a caspase inhibitor) [390] and also sensitive to intracellular and extracellular calcium, implicating calpain(s) as part of apoptosis in E4 cell death.

As indicated above, data from several cell types suggested possible activation of multiple cell death pathways, but activation of caspases through non-mitochondrial pathways and involvement of extrinsic apoptosis regulators. In agreement with these observations, using a simple, bistable rate-equation-based model that is used to predict trends of cellular apoptosis following electric pulsing, it was predicted that an extrinsic mechanism would be more sensitive than the mitochondrial intrinsic pathway for electric pulse-induced cell apoptosis [388].

The importance of extrinsic apoptosis cell regulators was demonstrated as an explanation for inherent differences in sensitivities of Jurkat cells (more) and U937 cells (less) to nsPEFs to 100, 10 ns, 50 or 150 kV/cm pulses [389]. Measurement of basal expression levels indicated that U937 cells had a higher expression of c-FLIP, an extrinsic apoptosis inhibitor, while Jurkat cells had a higher expression of FasL, an extrinsic apoptosis agonist. When cells were exposed to lethal nsPEF (150 kV/cm) and siRNA was used to knockdown c-FLIP protein expression in U937 cells or knockdown FasL in Jurkat cells, U937 survival was reduced nearly 60 % while Jurkat survival improved by 40 %. This provided the first explanation for inherent cell type survival difference to nsPEFs as differences in expression levels of apoptosis-related proteins as opposed to physical cell characteristic, such as membrane or cytoskeletal structure. This is reminiscent of differences between type I and type II cells, where the later require amplification through mitochondria to activate caspases by overcome high levels of IAP, an intrinsic apoptosis antagonist [363]. This same study demonstrated extrinsic apoptosis in Jurkat cells showing caspase 8 activation without BID cleavage, cytochrome c release, or caspase 9 activation, which is typical of type I cells. This is noteworthy, since Jurkat cells are type II cells, which require amplification of apoptosis signals through the intrinsic mitochondrial pathway. Perhaps, nsPEFs play a role in formation of lipid rafts that allow efficient formation of DISC and activation of caspase 8.

The above results are in contrast to previous work in Jurkat cells demonstrating cytochrome c release and caspase 9- and caspase 3-dependent cell death, typical of intrinsic apoptosis [147, 390]. In this study using 10, 1 Hz, 60 ns, 10–60 kV/cm pulses with Jurkat cell clones that either did not express FADD, caspase 8, or APAF-1 [147], it was demonstrated that cytochrome *c* release was not caspase dependent, suggesting that its release was not due to caspase 8 activation through the DISC or FADD-mediated mechanisms. Furthermore, electric field-dependent cell death was identical for wild type, FADD-deficient, and caspase 8-deficient cells, indicating that nsPEF-induced cell death under these conditions did not require any FADD complex or caspase 8. It was shown in an APAF-deficient Jurkat clone, which did not respond to nsPEF with caspase 9 or caspase 3 activation, that cell death was caspase- and AFAF-1 dependent at lower electric fields, mimicking an intrinsic apoptosis mechanism, and caspase independent at higher electric fields demonstrating that nsPEF-induced cell death did not necessarily require active caspases under most intense conditions. It is highly likely that both regulated apoptosis (caspase dependent) and regulated necrosis (caspase independent) coexist during nsPEF-induced cell death in Jurkat cells. Based on findings from HCT-116 colon carcinoma, B16f10 melanoma, E4 squamous cell carcinoma, and Jurkat cells, as well as from other studies (see below), it also seems highly likely that nsPEF-induced RCD is dependent on nsPEF conditions as well as the cell type.

Using U937 cells, Pakhomova and colleagues [149] defined two modes of cell death after treatment with nsPEFs depending on the media for cell incubation. These studies either used trapezoidal waveforms with 600 pulses, 200 Hz, 300 ns, 7 kV/cm, or square waveforms at 50 pulses, 1 Hz, 60 ns 30–40 kV/cm. In the presence of cell culture media, cell death appeared to be due to plasma membrane permeabilization, water uptake, cell swelling, and membrane rupture by 40 min after pulsing, typical of signs of "necrosis." In contrast, when media contained sucrose, cell swelling was prevented and cell death was delayed. Compared to conditions without sucrose, the presence of sucrose facilitated caspase 3/7 activation, which was evident at 1 h and peaked at 3–6 h, and facilitated PARP cleavage, which increased by 2 h and peaked by 4 h. These findings were characteristic for both diverse types of pulse waveforms. These results indicated that under standard cell culture conditions, U937 cells died without significant caspase activation by osmotic stress-related cell death defined here as necrosis. This form of cell death has been called oncosis (Greek ónkos for swelling) [343]. However, it is not accidental cell death (ACD), because it was not immediate and was transiently rescued or modulated by sucrose, which led to apoptotic cell death. Thus, the predominant early "necrotic" cell death prevented or obscured the observation of apoptotic cell death. It is possible that both types of cell death mechanisms were operative, but one was faster than the other, and blunting the osmotic stress with sucrose allowed the slower apoptotic mechanism to fully develop.

In subsequent studies by this group, similar experiments were done with several cell types adhered to indium tin oxide (ITO)-coated glass slides that fit into cuvettes for nsPEF treatment [148]. Since ITO is biologically inert and exhibits high conductance with optical transparency, it provides a means to treat cells with

nanosecond pulses and readily change media without potential artifacts due to cell damage by centrifugation. NsPEF treatment on ITO slides was highly efficient requiring about 20-fold fewer pulses. Treating cells with 20 pulses, 20 Hz, 300 ns 600–700 kV/cm, the author found that the mode of nsPEF-induced cell death (necrosis vs. apoptosis) was determined by the extracellular concentration of Ca^{2+}. There was a newly identified high Ca^{2+}-dependent necrotic cell death that was affected by a delayed, sudden, osmotic-independent pore expansion (or new pore formation); however, cell death was not caused by membrane rupture. This cell death mechanism is distinctly different than the osmotic-induced cell death characterized by swelling, but is not apoptotic cell death since caspase 3/7 activity was greatly reduced in the presence of high extracellular calcium. These studies demonstrate that there are multiple forms of cell death depending on the composition of the media and the levels of extracellular levels.

Other studies showed more directly that not all cell types died by apoptosis when exposed to nsPEFs. Unlike Jurkat cells, which readily exhibited apoptotic features in response to nsPEFs, nsPEF-treated HeLa S3 cells did not show caspase 3 activation or DNA ladder formation, both molecular signs of apoptotic cell death [146]. In contrast, these cells readily showed PARP-1-mediated PAR formation, a sign of regulated necrosis. When PARP-1 [poly(ADP ribose) (PAR) polymerase-1 becomes hyperactivated, it begins to oversynthesize branched, long poly (ADP ribose) (PAR). While PARP-1 is cleaved and inactivated by caspase 3 during apoptosis, hyperactivation and PAR formation lead to genotoxic and mitochondriotoxic stress causing loss of irreversible loss $\Delta\Psi_m$ and AIF release, overconsumption of NAD+ and ATP, and a dramatic energy crisis, leading to necrotic cell death. In these HeLa S3 cells, UV radiation-induced inactivation of PARP-1 and activation of caspase 3 indicate that apoptosis is functional program in these cells, but not activated by nsPEFs. In other studies these authors demonstrated that Ca^{2+} was required for nsPEF-induced PAR-mediated cell death, which was enhanced by the presence of the Ca^{2+} ionophore, ionomycin. They further showed that in the absence of Ca^{2+}, HeLa S3 cells were less susceptible to nsPEFs but could be forced to exhibit apoptotic signs of caspase 3 activation and PARP-1 cleavage with increasing pulse numbers [391]. Furthermore, nsPEF-induced regulated necrosis was not limited to HeLa cells but also occurred in K562 and HEK293 cells, with only limited signs of apoptosis markers (caspase 3 and PARP-1 cleavage). These studies demonstrate that nsPEF-induced cell death is cell type specific, but can be manipulated by altering conditions Ca^{2+} availability in HeLa S3 cells, demonstrating a characteristic of regulated cell death. PAR formation has been shown to be observed in parthanatos, a type of regulated necrosis.

A comparison of monopolar (MP) and bipolar (BP) pulses (polarity shift half way through pulse duration) with 600 ns pulse durations clearly demonstrated that BP pulses were less effective for membrane damage, permeability to ions, and cell lethality in three different cell types [392]. It took ten times more BPs to induce cell death than with MPs. This is in contract to conventional electroporation pulses (micro- and millisecond) where BPs are more effective for plasma membrane permeabilization [393] and DNA transfection while reducing cell death

[394]. Kotnik and colleagues also showed that BPs (500 + 500 μs and 1000 + 1000 μs) increased permeabilization of cells to bleomycin and Lucifer yellow without increased cell death [393]. It is reasoned that BPs reduce the holding time (passband) that would otherwise cause pore expansion, so BPs are less effective at causing pores to expand. These studies make clear that nsPEF-induced effects on the plasma membrane are critical for cell death induction.

4.10.7 Cellular Targets for nsPEF-Induced Regulated Cell Death

4.10.7.1 Plasma Membrane, Cell Ca^{2+}, and Mitochondria

The hypothesis that nsPEF have effects on intracellular structures prompted studies to investigate effects on cell organelles as targets for nsPEFs. It is generally agreed that plasma membrane permeabilization and influxes of Ca^{2+} and subsequent mitochondria Ca^{2+} overloading appear to be important determinants of cell death. Studies in N1-S1 hepatocellular carcinoma cells [233, 371] suggested that increases in intracellular Ca^{2+} were necessary, but not sufficient for cell death, unless there was a decrease in the $\Delta\Psi_m$, which was coincident with cell demise. This is similar to the "two-hit" hypothesis for cell death induced by ischemia reperfusion (Ca^{2+} and ROS) [395, 396], except the second hit, which is on mitochondria, is not likely due to generation of ROS [397]. Nevertheless, Ca^{2+} plays an important role in the nsPEF-triggered increase in ROS in BxPC-3 human pancreatic cells [145], and ROS appears to be required for formation of the apoptosome [398], the apoptotic assembly "station" for caspase 9 activation with cytochrome c, APAF-1, and dATP.

4.10.7.2 The Nucleus and DNA Have Been the Focus of a Number of Studies

Many studies have shown that nsPEFs induce DNA damage determined by TUNEL, comet assays, fragmentation by flow cytometry, and histone-2AX phosphorylation. The earliest and perhaps the most thorough study analyzing effects of nsPEF on DNA demonstrated that nsPEF-induced genotoxicity was cell type dependent, with nonadherent cells being more sensitive than adherent cells [399]. After a single 60 ns, 60 kV/cm pulse, unlike all but one of seven adherent cell types, nonadherent cells exhibited 10 % survival, induction of DNA damage, and a decrease in the number of cells reaching mitosis. Comet assays immediately after nsPEF treatment of Jurkat cells increased comet tail lengths 1.3- and 2.6-fold with one and ten pulses, respectively, with the same conditions indicated above, indicating that DNA damage was a direct effect of electric fields. HL60 cells also showed similar effects, albeit less striking. When DNA was isolated immediately after pulsing and analyzed by electrophoresis on agarose gels, a smear of DNA

occurred in cells exposed to five pulses with conditions above while DNA from unexposed cells was present as a tight band, again indicating direct nsPEF-induced DNA damage. Examining lymphoblastoid cell line (LCL) from a homozygous patient with ataxia telangiectasia (AT), who are unable to repair DNA damage in response to radiation, chromatid aberrations were identified in 78 % of cells exposed to a single 600-ns, 60-kV/cm pulse, while only 22 % were observed in control cells. In all, 41 types of damage were observed in exposed cells including more chromatin gaps, breaks, and fragments than in control cells.

Another study demonstrated disruption of the actin cytoskeleton and nuclear membrane and damage to telomeres that appeared to decrease Jurkat cell survival exposed to single 60-ns 60-kV/cm pulses [251]. It is hypothesized that no nuclear damage was done to adherent cells under these conditions, presumably because their cytoskeletons absorb some of the impact of the electric field effects. In another study with Jurkat cells under "milder," nonlethal nsPEF conditions (single 60 ns, 10–25 kV/cm), there was a transient electric field-dependent decrease in the comet assay DNA migration. The authors suggested that their results were due to pulse-induced transient conformational change in the living cell nucleoprotein [400]. Others observed transiently disrupted cytoskeleton and transient increase in nuclear size in adherent HCT-116 cells exposed to three 60- or 300-ns, 60-kV/cm pulses [373].

4.10.8 In Vivo Studies Showing nsPEF-Induced Regulated Cell Death

Early studies with tumor tissues demonstrated that nsPEFs induced DNA fragmentation (TUNEL) and reduced fibrosarcoma tumor growth in a mouse model [233, 238, 371]. Using 10-ns or 300-ns pulses with electric field intensities of 280 and 30 kV/cm, respectively (near-equal energy densities), greater increases in DNA fragmentation were seen with the 300-ns condition, indicating that this effect, like effects in vitro, was independent of energy density. Fibrosarcoma tumors treated with three 10-ns pulses at 260 kV/cm exhibited twice as many TUNEL-positive tumor cells as sham-treated tumors. Tumors treated with 300-ns pulses and 75 kV/cm were 60 % smaller than sham-treated tumors, indicating that nsPEFs could likely be used for tumor treatment.

In a murine B16f10 melanoma model (hairless SKH-1 mice), Nuccitelli and coworkers [401] later showed that pulsed electric fields greater than 20 kV/cm, with risetimes of 30 ns and durations of 300 ns, caused tumor cell nuclei to rapidly shrink and tumor blood flow to stop in a temperature-independent manner (3 °C increase). Within 2 weeks, B16f10 tumors shrank by 90 % and a second treatment resulted in complete remission. In a later study [402], it was shown that after nsPEF ablation (300–600 pulses, 300 ns, 40–50 kV/cm 0.5 Hz), none of the melanomas recurred during a 4-month period. For complete remission, 24 % melanomas were

eliminated after one treatment, 59 % required a second treatment, and 18 % required a third treatment. A microvessel density marker (CD31) was decreased significantly after treatment, agreeing with the decreased blood flow to treated tumors. The possible presence of apoptosis was suggested by a decrease in the antiapoptotic protein BCL-2.

It was later shown in this same model that after treatment with one hundred 300-ns pulses at 40 kV/cm, transient increases in histone 2AX phosphorylation (early DNA damage repair marker) coinciding with TUNEL-positive cells and pyknotic nuclei were observed. Caspase-positive cells were not observed until 6 h after pulsing, suggesting caspase-independent effects on DNA. Large DNA fragments, but not 180-bp fragmentation ladders, were observed, suggesting that apoptosis was incomplete. Anti-angiogenesis or anti-vascular effects were demonstrated by decreases in markers for vascular endothelial cells (CD31, CD35, and CD105) and growth factors (VEGF and PD-ECGF).

A study by X Chen et al. [403] showed that nsPEF effectively eliminated (75 %) and activated RCD in a mouse Hepa1-6 ectopic hepatocellular carcinoma (HCC) model with 100-ns, 65-kV/cm pulses (one treatment, 900 pulses, or three treatments 300 pulses each on alternate days), but not effectively with 100-ns, 33- or 50-kV/cm (37 %), or with 30-ns, $\leq$ 65-kV/cm pulses ($<$ 35 %). Under optimal conditions, nuclei rapidly shrunk (1–2 h) and became transiently TUNEL positive peaking at 3 h. Caspase 3/6/7 was transiently activated peaking at 3 h, but no more than 50 % of cells were caspase positive at that peak time. Phospho-BAD, which would be unavailable to promoting cytochrome c release, remained low. Anti-angiogenesis or anti-vascular effects were also demonstrated with CD34 and VEGF in this model.

Efficacy of nsPEF ablation was also shown in an orthotopic rat N1-S1 HCC model [404]. Data demonstrate 80–90 % when elimination with 1000, 100 ns, 50 kV/cm pulses were delivered at 1 Hz. Transient increases in active caspase 3 (6 h) and caspase 9 (2–6 h), but not in active caspase 8, indicating an intrinsic apoptosis mechanism(s) as well as caspase-independent mechanisms (cells negative for active caspase), which is in agreement with in vitro data. Interestingly, after ablation rats were resistant to challenge injections of the same cells, showing a vaccine-like effect that may be due to activation of an active immune response. Infiltration of immune cells and the presence of granzyme B expressing cells within days of treatment suggest an antitumor adaptive immune response. In other studies [405] nsPEF cleared UV-induced murine melanomas and was superior to tumor excision for accelerating secondary tumor rejection in immune-competent mice. An immune response was suggested by the presence of CD4+ T cells within treated tumors.

NsPEF treatment of basal cell carcinoma has shown promise in the first clinical trial of nsPEF ablation [406].

References

1. Cortese, B., Palamà, I.E., D'Amone, S., Gigli, G.: Influence of electrotaxis on cell behaviour. Integr. Biol. **6**, 817–830 (2014). doi:10.1039/C4IB00142G
2. Levin, M., Stevenson, C.G.: Regulation of cell behavior and tissue patterning by bioelectrical signals: challenges and opportunities for biomedical engineering. Annu. Rev. Biomed. Eng. **14**, 295–323 (2012). doi:10.1146/annurev-bioeng-071811-150114
3. Kotnik, T., Kramar, P., Pucihar, G., et al.: Cell membrane electroporation- part 1: the phenomenon. IEEE Electr. Insul. Mag. **28**, 14–23 (2012). doi:10.1109/MEI.2012.6268438
4. Klösgen, B., Reichle, C., Kohlsmann, S., Kramer, K.D.: Dielectric spectroscopy as a sensor of membrane headgroup mobility and hydration. Biophys. J. **71**, 3251–3260 (1996)
5. Tielrooij, K.J., Paparo, D., Piatkowski, L., et al.: Dielectric relaxation dynamics of water in model membranes probed by terahertz spectroscopy. Biophys. J. **97**, 2484–2492 (2009). doi:10.1016/j.bpj.2009.08.024
6. Feldman, Y., Ermolina, I., Hayashi, Y.: Time domain dielectric spectroscopy study of biological systems. IEEE Trans. Dielectr. Electr. Insul. **10**, 728–753 (2003). doi:10.1109/TDEI.2003.1237324
7. Vernier, P.T., Ziegler, M.J.: Nanosecond field alignment of head group and water dipoles in electroporating phospholipid bilayers. J. Phys. Chem. B **111**, 12993–12996 (2007). doi:10.1021/jp077148q
8. Kotnik, T., Bobanović, F., Miklavčič: Sensitivity of transmembrane voltage induced by applied electric fields—a theoretical analysis. Bioelectrochem. Bioenerg. **43**, 285–291 (1997). doi:10.1016/S0302-4598(97)00023-8
9. Kotnik, T., Miklavčič, D., Slivnik, T.: Time course of transmembrane voltage induced by time-varying electric fields—a method for theoretical analysis and its application. Bioelectrochem. Bioenerg. **45**, 3–16 (1998). doi:10.1016/S0302-4598(97)00093-7
10. Kotnik, T., Miklavčič, D.: Second-order model of membrane electric field induced by alternating external electric fields. IEEE Trans. Biomed. Eng. **47**, 1074–1081 (2000). doi:10.1109/10.855935
11. Hibino, M., Shigemori, M., Itoh, H., et al.: Membrane conductance of an electroporated cell analyzed by submicrosecond imaging of transmembrane potential. Biophys. J. **59**, 209–220 (1991)
12. Hibino, M., Itoh, H., Kinosita, K.: Time courses of cell electroporation as revealed by submicrosecond imaging of transmembrane potential. Biophys. J. **64**, 1789–1800 (1993)
13. Smith, K.C., Weaver, J.C.: Active mechanisms are needed to describe cell responses to submicrosecond, megavolt-per-meter pulses: cell models for ultrashort pulses. Biophys. J. **95**, 1547–1563 (2008). doi:10.1529/biophysj.107.121921
14. Kotnik, T., Miklavčič, D.: Theoretical evaluation of voltage inducement on internal membranes of biological cells exposed to electric fields. Biophys. J. **90**, 480–491 (2006). doi:10.1529/biophysj.105.070771
15. Kotnik, T., Pucihar, G.: Induced transmembrane voltage—theory, modeling, and experiments. In: Miklavčič, D., Markov, M.S., Pakhomov, A.G. (eds.) Advanced Electroporation Techniques in Biology and Medicine, pp. 51–70. CRC Press, Boca Raton (2010)
16. Asami, K., Takahashi, Y., Takashima, S.: Dielectric properties of mouse lymphocytes and erythrocytes. Biochim. Biophys. Acta. BBA – Mol. Cell Res. **1010**, 49–55 (1989). doi:10.1016/0167-4889(89)90183-3
17. Yao, C., Mo, D., Li, C., et al.: Study of transmembrane potentials of inner and outer membranes induced by pulsed-electric-field model and simulation. IEEE Trans. Plasma. Sci. **35**, 1541–1549 (2007). doi:10.1109/TPS.2007.905110
18. Retelj, L., Pucihar, G., Miklavčič, D.: Electroporation of intracellular liposomes using nanosecond electric pulses-a theoretical study. IEEE Trans. Biomed. Eng. **60**, 2624–2635 (2013). doi:10.1109/TBME.2013.2262177

19. Schoenbach, K.H., Beebe, S.J., Buescher, E.S.: Intracellular effect of ultrashort electrical pulses. Bioelectromagnetics **22**, 440–448 (2001). doi:10.1002/bem.71
20. Tekle, E., Oubrahim, H., Dzekunov, S.M., et al.: Selective field effects on intracellular vacuoles and vesicle membranes with nanosecond electric pulses. Biophys. J. **89**, 274–284 (2005). doi:10.1529/biophysj.104.054494
21. White, J.A., Blackmore, P.F., Schoenbach, K.H., Beebe, S.J.: Stimulation of capacitative calcium entry in HL-60 cells by nanosecond pulsed electric fields. J. Biol. Chem. **279**, 22964–22972 (2004). doi:10.1074/jbc.M311135200
22. Batista Napotnik, T., Reberšek, M., Kotnik, T., et al.: Electropermeabilization of endocytotic vesicles in B16 F1 mouse melanoma cells. Med. Biol. Eng. Comput. **48**, 407–413 (2010). doi:10.1007/s11517-010-0599-9
23. Krassowska, W., Filev, P.D.: Modeling electroporation in a single cell. Biophys. J. **92**, 404–417 (2007). doi:10.1529/biophysj.106.094235
24. Li, J., Tan, W., Yu, M., Lin, H.: The effect of extracellular conductivity on electroporation-mediated molecular delivery. Biochim. Biophys. Acta **1828**, 461–470 (2013). doi:10.1016/j.bbamem.2012.08.014
25. Pucihar, G., Kotnik, T., Valič, B., Miklavčič, D.: Numerical determination of transmembrane voltage induced on irregularly shaped cells. Ann. Biomed. Eng. **34**, 642–652 (2006). doi:10.1007/s10439-005-9076-2
26. Hu, Q., Viswanadham, S., Joshi, R.P., et al.: Simulations of transient membrane behavior in cells subjected to a high-intensity ultrashort electric pulse. Phys. Rev. E **71**, 031914 (2005). doi:10.1103/PhysRevE.71.031914
27. Gowrishankar, T.R., Smith, K.C., Weaver, J.C.: Transport-based biophysical system models of cells for quantitatively describing responses to electric fields. Proc. IEEE **101**, 505–517 (2013). doi:10.1109/JPROC.2012.2200289
28. Pucihar, G., Miklavčič, D., Kotnik, T.: A time-dependent numerical model of transmembrane voltage inducement and electroporation of irregularly shaped cells. IEEE Trans. Biomed. Eng. **56**, 1491–1501 (2009). doi:10.1109/TBME.2009.2014244
29. Susil, R., Semrov, D., Miklavčič, D.: Electric field induced transmembrane potential depends on cell density and organization. Electro. Magnetobiol. **17**, 391–399 (1998)
30. Pavlin, M., Pavselj, N., Miklavčič, D.: Dependence of induced transmembrane potential on cell density, arrangement, and cell position inside a cell system. IEEE Trans. Biomed. Eng. **49**, 605–612 (2002)
31. Pucihar, G., Kotnik, T., Teissié, J., Miklavčič, D.: Electropermeabilization of dense cell suspensions. Eur. Biophys. J. **36**, 173–185 (2007). doi:10.1007/s00249-006-0115-1
32. Ling, G., Gerard, R.W.: The normal membrane potential of frog sartorius fibers. J. Cell. Comp. Physiol. **34**, 383–396 (1949). doi:10.1002/jcp.1030340304
33. Neher, E., Sakmann, B.: Single-channel currents recorded from membrane of denervated frog muscle fibres. Nature **260**, 799–802 (1976). doi:10.1038/260799a0
34. Fluhler, E., Burnham, V.G., Loew, L.M.: Spectra, membrane binding, and potentiometric responses of new charge shift probes. Biochemistry (Mosc.) **24**, 5749–5755 (1985). doi:10.1021/bi00342a010
35. Gross, D., Loew, L.M., Webb, W.W.: Optical imaging of cell membrane potential changes induced by applied electric fields. Biophys. J. **50**, 339–348 (1986)
36. Pucihar, G., Kotnik, T., Miklavčič, D.: Measuring the induced membrane voltage with Di-8-ANEPPS. J. Vis. Exp. JoVE. (2009). doi:10.3791/1659
37. Frey, W., White, J.A., Price, R.O., et al.: Plasma membrane voltage changes during nanosecond pulsed electric field exposure. Biophys. J. **90**, 3608–3615 (2006). doi:10.1529/biophysj.105.072777
38. White, J.A., Pliquett, U., Blackmore, P.F., et al.: Plasma membrane charging of Jurkat cells by nanosecond pulsed electric fields. Eur. Biophys. J. **40**, 947–957 (2011). doi:10.1007/s00249-011-0710-7

39. Towhidi, L., Kotnik, T., Pucihar, G., et al.: Variability of the minimal transmembrane voltage resulting in detectable membrane electroporation. Electromagn. Biol. Med. **27**, 372–385 (2008). doi:10.1080/15368370802394644
40. Gabriel, B., Teissie, J.: Time courses of mammalian cell electropermeabilization observed by millisecond imaging of membrane property changes during the pulse. Biophys. J. **76**, 2158–2165 (1999)
41. Pucihar, G., Kotnik, T., Miklavčič, D., Teissié, J.: Kinetics of transmembrane transport of small molecules into electropermeabilized cells. Biophys. J. **95**, 2837–2848 (2008). doi:10.1529/biophysj.108.135541
42. He, H., Chang, D.C., Lee, Y.-K.: Using a micro electroporation chip to determine the optimal physical parameters in the uptake of biomolecules in HeLa cells. Bioelectrochem. Amst. Neth. **70**, 363–368 (2007). doi:10.1016/j.bioelechem.2006.05.008
43. Pakhomov, A.G., Gianulis, E., Vernier, P.T., et al.: Multiple nanosecond electric pulses increase the number but not the size of long-lived nanopores in the cell membrane. Biochim. Biophys. Acta. BBA – Biomembr. **1848**, 958–966 (2015). doi:10.1016/j.bbamem.2014.12.026
44. Vasilkoski, Z., Esser, A.T., Gowrishankar, T.R., Weaver, J.C.: Membrane electroporation: the absolute rate equation and nanosecond time scale pore creation. Phys. Rev. E **74**, 021904 (2006). doi:10.1103/PhysRevE.74.021904
45. Kotnik, T., Pucihar, G., Miklavčič, D.: Induced transmembrane voltage and its correlation with electroporation-mediated molecular transport. J. Membr. Biol. **236**, 3–13 (2010). doi:10.1007/s00232-010-9279-9
46. Smith, K.C.: A unified model of electroporation and molecular transport. Massachusetts Institute of Technology, http://dspace.mit.edu/bitstream/handle/1721.1/63085/725958797.pdf
47. Son, R.S., Smith, K.C., Gowrishankar, T.R., Vernier, P.T., Weaver, J.C.: J. Membr. Biol. **247**, 1209 (2014)
48. Pauly, H., Schwan, H.P.: Z Naturforsch **14B**, 125 (1959)
49. Gowrishankar, T.R., Weaver, J.C.: Proc. Natl. Acad. Sci. U. S. A. **100**, 3203 (2003)
50. Smith, K.C., Weaver, J.C.: IEEE Trans. Biomed. Eng. **59**, 1514 (2012)
51. Kinosita, K., Ashikawa, I., Saita, N., Yoshimura, H., Itoh, H., Nagayma, K., Ikegami, A.: Biophys. J. **53**, 1015 (1988)
52. Singer, S.J., Nicolson, G.L.: The fluid mosaic model of the structure of cell membranes. Science **175**, 720–731 (1972)
53. Abidor, I.G., Arakelyan, V.B., Chernomordik, L.V., Chizmadzhev, Y.A., Pastushenko, V.F., Tarasevich, M.R.: Electric breakdown of bilayer lipid membranes I. Main experimental facts and their qualitative discussion. Bioelectrochem. Bioenerg. **6**, 37–52 (1979)
54. Sugar, I.P.: The effects of external fields on the structure of lipid bilayers. J. Physiol. Paris **77**, 1035–1042 (1981)
55. Zimmermann, U., Scheurich, P., Pilwat, G., Benz, R.: Cells with manipulated functions: new perspectives for cell biology, medicine, and technology. Angew. Chem. Int. Ed. Engl. **20**, 325–344 (1981)
56. Neumann, E., Schaefer-Ridder, M., Wang, Y., Hofschneider, P.H.: Gene transfer into mouse lyoma cells by electroporation in high electric fields. EMBO J. **1**, 841–845 (1982)
57. Sugar, I.P., Neumann, E.: Stochastic model for electric field-induced membrane pores. Electroporation. Biophys. Chem. **19**, 211–225 (1984)
58. Bockmann, R.A., de Groot, B.L., Kakorin, S., Neumann, E., Grubmuller, H.: Kinetics, statistics, and energetics of lipid membrane electroporation studied by molecular dynamics simulations. Biophys. J. **95**, 1837–1850 (2008)
59. Levine, Z.A., Vernier, P.T.: Life cycle of an electropore: field-dependent and field-independent steps in pore creation and annihilation. J. Membr. Biol. **236**, 27–36 (2010)

60. Marracino, P., Amadei, A., Apollonio, F., D'Inzeo, G., Liberti, M., di Crescenzo, A., Fontana, A., Zappacosta, R., Aschi, M.: Modeling of chemical reactions in micelle: water-mediated keto-enol interconversion as a case study. J. Phys. Chem. B **115**, 8102–8111 (2011)
61. van der Ploeg, P., Berendsen, H.J.C.: Molecular dynamics simulation of a bilayer membrane. J. Chem. Phys. **76**, 3271–3276 (1982)
62. Egberts, E., Marrink, S.J., Berendsen, H.J.: Molecular dynamics simulation of a phospholipid membrane. Eur. Biophys. J. **22**, 423–436 (1994)
63. Tieleman, D.P., Leontiadou, H., Mark, A.E., Marrink, S.J.: Simulation of pore formation in lipid bilayers by mechanical stress and electric fields. J. Am. Chem. Soc. **125**, 6382–6383 (2003)
64. Gurtovenko, A.A., Vattulainen, I.: Pore formation coupled to ion transport through lipid membranes as induced by transmembrane ionic charge imbalance: atomistic molecular dynamics study. J. Am. Chem. Soc. **127**, 17570–17571 (2005)
65. Tarek, M.: Membrane electroporation: a molecular dynamics simulation. Biophys. J. **88**, 4045–4053 (2005)
66. Tieleman, D.P.: The molecular basis of electroporation. BMC Biochem. **5**, 10 (2004)
67. Ho, M.C., Levine, Z.A., Vernier, P.T.: Nanoscale, electric field-driven water bridges in vacuum gaps and lipid bilayers. J. Membr. Biol. **246**, 793–801 (2013)
68. Tokman, M., Lee, J.H., Levine, Z.A., Ho, M.C., Colvin, M.E., Vernier, P.T.: Electric field-driven water dipoles: nanoscale architecture of electroporation. PLoS One **8**, e61111 (2013)
69. Neumann, E., Rosenheck, K.: Permeability changes induced by electric impulses in vesicular membranes. J. Membr. Biol. **10**, 279–290 (1972)
70. Weaver, J.C.: Electroporation theory. Concepts and mechanisms. Methods Mol. Biol. **48**, 3–28 (1995)
71. Bernhardt, J., Pauly, H.: On the generation of potential differences across the membranes of ellipsoidal cells in an alternating electrical field. Biophysik **10**, 89–98 (1973)
72. Teissie, J., Golzio, M., Rols, M.P.: Mechanisms of cell membrane electropermeabilization: a minireview of our present (lack of ?) knowledge. Biochim. Biophys. Acta **1724**, 270–280 (2005)
73. Robello, M., Gliozzi, A.: Conductance transition induced by an electric field in lipid bilayers. Biochim. Biophys. Acta **982**, 173–176 (1989)
74. Teissie, J., Rols, M.P.: An experimental evaluation of the critical potential difference inducing cell-membrane electropermeabilization. Biophys. J. **65**, 409–413 (1993)
75. Rols, M.P., Teissie, J.: Electropermeabilization of mammalian cells. Quantitative analysis of the phenomenon. Biophys. J. **58**, 1089–1098 (1990)
76. Kotnik, T., Miklavcic, D.: Analytical description of transmembrane voltage induced by electric fields on spheroidal cells. Biophys. J. **79**, 670–679 (2000)
77. Kotnik, T., Pucihar, G., Rebersek, M., Miklavcic, D., Mir, L.M.: Role of pulse shape in cell membrane electropermeabilization. Biochim. Biophys. Acta **1614**, 193–200 (2003)
78. Gehl, J.: Electroporation: theory and methods, perspectives for drug delivery, gene therapy and research. Acta Physiol. Scand. **177**, 437–447 (2003)
79. Staal, L., Gilbert, R.: Generators and applicators: equipment for electroporation. In: Kee, S. T., Gehl, J., Lee, E.W. (eds.) Clinical Aspects of Electroporation. Springer, New York (2011)
80. Gothelf, A., Gehl, J.: Electroporation-based DNA delivery technology: methods for gene electrotransfer to skin. In: Rinaldi, M., Fioretti, D., Iurescia, S. (eds.) DNA Vaccines. Springer, New York (2014)
81. Tamzali, Y., Borde, L., Rols, M.P., Golzio, M., Lyazrhi, F., Teissie, J.: Successful treatment of equine sarcoids with cisplatin electrochemotherapy: a retrospective study of 48 cases. Equine Vet. J. **44**, 214–220 (2012)
82. Rols, M.P., Delteil, C., Serin, G., Teissie, J.: Temperature effects on electrotransfection of mammalian cells. Nucleic Acids Res. **22**, 540 (1994)
83. Rols, M.P., Golzio, M., Gabriel, B., Teissie, J.: Factors controlling electropermeabilisation of cell membranes. Technol. Cancer Res. Treat. **1**, 319–328 (2002)

84. Kinosita Jr., K., Tsong, T.Y.: Formation and resealing of pores of controlled sizes in human erythrocyte membrane. Nature **268**, 438–441 (1977)
85. Kinosita Jr., K., Tsong, T.Y.: Voltage-induced conductance in human erythrocyte membranes. Biochim. Biophys. Acta **554**, 479–497 (1979)
86. Rols, M.P., Teissie, J.: Electropermeabilization of mammalian cells to macromolecules: control by pulse duration. Biophys. J. **75**, 1415–1423 (1998)
87. Pucihar, G., Mir, L.M., Miklavcic, D.: The effect of pulse repetition frequency on the uptake into electropermeabilized cells in vitro with possible applications in electrochemotherapy. Bioelectrochemistry **57**, 167–172 (2002)
88. Rols, M.P., Teissie, J.: Flow cytometry quantification of electropermeabilization. Methods Mol. Biol. **91**, 141–147 (1998)
89. Escoffre, J.M., Portet, T., Favard, C., Teissie, J., Dean, D.S., Rols, M.P.: Electromediated formation of DNA complexes with cell membranes and its consequences for gene delivery. Biochim. Biophys. Acta **1808**, 1538–1543 (2011)
90. Orlowski, S., Belehradek Jr., J., Paoletti, C., Mir, L.M.: Transient electropermeabilization of cells in culture. Increase of the cytotoxicity of anticancer drugs. Biochem. Pharmacol. **37**, 4727–4733 (1988)
91. Portet, T., Camps I Febrer, F., Escoffre, J.M., Favard, C., Rols, M.P., Dean, D.S.: Visualization of membrane loss during the shrinkage of giant vesicles under electropulsation. Biophys. J. **96**, 4109–4121 (2009)
92. Chopinet, L., Roduit, C., Rols, M.P., Dague, E.: Destabilization induced by electropermeabilization analyzed by atomic force microscopy. Biochim. Biophys. Acta **1828**, 2223–2229 (2013)
93. Chernysh, A.M., Kozlova, E.K., Moroz, V.V., Borshagovskaya, P.Y., Bliznuk, U.A., Rysaeva, R.M.: Erythrocyte membrane surface after calibrated electroporation: visualization by atomic force microscopy. Bull. Exp. Biol. Med. **148**, 455–460 (2009)
94. Lopez, A., Rols, M.P., Teissie, J.: ^{31}P NMR analysis of membrane phospholipid organization in viable, reversibly electropermeabilized Chinese hamster ovary cells. Biochemistry **27**, 1222–1228 (1988)
95. Stulen, G.: Electric field effects on lipid membrane structure. Biochim. Biophys. Acta **640**, 621–627 (1981)
96. Mauroy, C., Portet, T., Winterhalder, M., Bellard, E., Blache, M.C., Teissie, J., Zumbusch, A., Rols, M.P.: Giant lipid vesicles under electric field pulses assessed by non invasive imaging. Bioelectrochemistry **87**, 253–259 (2012)
97. Silve, A., Leray, I., Mir, L.M.: Demonstration of cell membrane permeabilization to medium-sized molecules caused by a single 10 ns electric pulse. Bioelectrochemistry **87**, 260–264 (2012)
98. Golzio, M., Teissie, J., Rols, M.P.: Direct visualization at the single-cell level of electrically mediated gene delivery. Proc. Natl. Acad. Sci. U. S. A. **99**, 1292–1297 (2002)
99. Rols, M.P., Teissie, J.: Experimental evidence for the involvement of the cytoskeleton in mammalian cell electropermeabilization. Biochim. Biophys. Acta **1111**, 45–50 (1992)
100. Rols, M.P., Delteil, C., Golzio, M., Teissie, J.: Control by ATP and ADP of voltage-induced mammalian-cell-membrane permeabilization, gene transfer and resulting expression. Eur. J. Biochem. **254**, 382–388 (1998)
101. Escoffre, J.M., Bellard, E., Faurie, C., Sebai, S.C., Golzio, M., Teissie, J., Rols, M.P.: Membrane disorder and phospholipid scrambling in electropermeabilized and viable cells. Biochim. Biophys. Acta **1838**, 1701–1709 (2014)
102. Rosazza, C., Buntz, A., Riess, T., Woll, D., Zumbusch, A., Rols, M.P.: Intracellular tracking of single plasmid DNA-particles after delivery by electroporation. Mol. Ther. **21**, 2217–2226 (2013)
103. Mahrour, N., Pologea-Moraru, R., Moisescu, M.G., Orlowski, S., Leveque, P., Mir, L.M.: In vitro increase of the fluid-phase endocytosis induced by pulsed radiofrequency

electromagnetic fields: importance of the electric field component. Biochim. Biophys. Acta **1668**, 126–137 (2005)
104. Antov, Y., Barbul, A., Mantsur, H., Korenstein, R.: Electroendocytosis: exposure of cells to pulsed low electric fields enhances adsorption and uptake of macromolecules. Biophys. J. **88**, 2206–2223 (2005)
105. Teissie, J., Knutson, V.P., Tsong, T.Y., Lane, M.D.: Electric pulse-induced fusion of 3T3 cells in monolayer culture. Science **216**, 537–538 (1982)
106. Teissie, J., Rols, M.P.: Fusion of mammalian cells in culture is obtained by creating the contact between cells after their electropermeabilization. Biochem. Biophys. Res. Commun. **140**, 258–266 (1986)
107. Mekid, H., Mir, L.M.: In vivo cell electrofusion. Biochim. Biophys. Acta **1524**, 118–130 (2000)
108. Marrero, B., Heller, R.: The use of an in vitro 3D melanoma model to predict in vivo plasmid transfection using electroporation. Biomaterials **33**, 3036–3046 (2012)
109. Gibot, L., Wasungu, L., Teissie, J., Rols, M.P.: Antitumor drug delivery in multicellular spheroids by electropermeabilization. J. Control. Release **167**, 138–147 (2013)
110. Canatella, P.J., Black, M.M., Bonnichsen, D.M., McKenna, C., Prausnitz, M.R.: Tissue electroporation: quantification and analysis of heterogeneous transport in multicellular environments. Biophys. J. **86**, 3260–3268 (2004)
111. Chopinet, L., Wasungu, L., Rols, M.P.: First explanations for differences in electrotransfection efficiency in vitro and in vivo using spheroid model. Int. J. Pharm. **423**, 7–15 (2012)
112. Rols, M.P., Delteil, C., Golzio, M., Dumond, P., Cros, S., Teissie, J.: In vivo electrically mediated protein and gene transfer in murine melanoma. Nat. Biotechnol. **16**, 168–171 (1998)
113. Gibot, L., Rols, M.P.: Progress and prospects: the use of 3D spheroid model as a relevant way to study and optimize DNA electrotransfer. Curr. Gene Ther. **13**, 175–181 (2013)
114. Madi, M., Rols, M.P., Gibot, L.: Efficient in vitro electropermeabilization of reconstructed human dermal tissue. J. Membr. Biol. **248**, 903–908 (2015)
115. Neumann, E., Sowers, A.E., Jordan, C.A.: Electroporation and Electrofusion in Cell Biology. Plenum, New York (1989)
116. Saulis, G.: Kinetics of pore disappearance in a cell after electroporation. Biomed. Sci. Instrum. **35**, 409–414 (1999)
117. Saulis, G., Venslauskas, M.S., Naktinis, J.: Kinetics of pore resealing in cell membranes after electroporation. Bioelectrochem. Bioenerg. **26**, 1–13 (1991)
118. Smith, K.C., Gowrishankar, T.R., Esser, A.T., Stewart, D.A., Weaver, J.C.: Spatially distributed, dynamic transmembrane voltages of organelle and cell membranes due to 10 ns pulses: predictions of meshed and unmeshed transport network models. IEEE Trans. Plasma Sci. **34**, 1394–1404 (2006)
119. Gowrishankar, T.R., Weaver, J.C.: Electrical behavior and pore accumulation in a multicellular model for conventional and supra-electroporation. Biochem. Biophys. Res. Commun. **349**, 643–653 (2006)
120. Hu, Q., Joshi, R.P., Schoenbach, K.H.: Simulations of nanopore formation and phosphatidylserine externalization in lipid membranes subjected to a high-intensity, ultrashort electric pulse. Phys. Rev. E Stat. Nonlin. Soft Matter Phys. **72**, 031902 (2005)
121. Nesin, O.M., Pakhomova, O.N., Xiao, S., Pakhomov, A.G.: Manipulation of cell volume and membrane pore comparison following single cell permeabilization with 60- and 600-ns electric pulses. Biochim. Biophys. Acta **1808**, 792–801 (2011)
122. Pakhomov, A.G., Pakhomova, O.N.: Nanopores: a distinct transmembrane passageway in electroporated cells. In: Pakhomov, A.G., Miklavčič, D., Markov, M.S. (eds.) Advanced Electroporation Techniques in Biology and Medicine, pp. 178–194. CRC Press, Boca Raton (2010)

123. Bowman, A.M., Nesin, O.M., Pakhomova, O.N., Pakhomov, A.G.: Analysis of plasma membrane integrity by fluorescent detection of Tl(+) uptake. J. Membr. Biol. **236**, 15–26 (2010)
124. Glaser, R.W., Leikin, S.L., Chernomordik, L.V., Pastushenko, V.F., Sokirko, A.I.: Reversible electrical breakdown of lipid bilayers: formation and evolution of pores. Biochim. Biophys. Acta **940**, 275–287 (1988)
125. Gabai, V.L., Meriin, A.B., Mosser, D.D., Caron, A.W., Rits, S., Shifrin, V.I., Sherman, M.Y.: Hsp70 prevents activation of stress kinases. A novel pathway of cellular thermotolerance. J. Biol. Chem. **272**, 18033–18037 (1997)
126. Barros, L.F., Hermosilla, T., Castro, J.: Necrotic volume increase and the early physiology of necrosis. Comp. Biochem. Physiol. A Mol. Integr. Physiol. **130**, 401–409 (2001)
127. Barros, L.F., Stutzin, A., Calixto, A., Catalan, M., Castro, J., Hetz, C., Hermosilla, T.: Nonselective cation channels as effectors of free radical-induced rat liver cell necrosis. Hepatology **33**, 114–122 (2001)
128. Dyachok, O., Zhabyeyev, P., McDonald, T.F.: Electroporation-induced inward current in voltage-clamped guinea pig ventricular myocytes. J. Membr. Biol. **238**, 69–80 (2010)
129. Pakhomov, A.G., Bowman, A.M., Ibey, B.L., Andre, F.M., Pakhomova, O.N., Schoenbach, K.H.: Lipid nanopores can form a stable, ion channel-like conduction pathway in cell membrane. Biochem. Biophys. Res. Commun. **385**, 181–186 (2009)
130. Semenov, I., Xiao, S., Pakhomova, O.N., Pakhomov, A.G.: Recruitment of the intracellular Ca by ultrashort electric stimuli: The impact of pulse duration. Cell Calcium **54**, 145–150 (2013)
131. Semenov, I., Xiao, S., Pakhomov, A.G.: Primary pathways of intracellular Ca(2+) mobilization by nanosecond pulsed electric field. Biochim. Biophys. Acta **1828**, 981–989 (2013)
132. Okada, Y.: Ion channels and transporters involved in cell volume regulation and sensor mechanisms. Cell Biochem. Biophys. **41**, 233–258 (2004)
133. Okada, Y., Shimizu, T., Maeno, E., Tanabe, S., Wang, X., Takahashi, N.: Volume-sensitive chloride channels involved in apoptotic volume decrease and cell death. J. Membr. Biol. **V209**, 21–29 (2006)
134. Molleman, A.: Patch Clamping: An Introductory Guide to Patch Clamp Electrophysiology. Wiley, Padstow (2002)
135. Ibey, B.L., Xiao, S., Schoenbach, K.H., Murphy, M.R., Pakhomov, A.G.: Plasma membrane permeabilization by 60- and 600-ns electric pulses is determined by the absorbed dose. Bioelectromagnetics **30**, 92–99 (2009)
136. Varghese, A., Tenbroek, E.M., Coles Jr., J., Sigg, D.C.: Endogenous channels in HEK cells and potential roles in HCN ionic current measurements. Prog. Biophys. Mol. Biol. **90**, 26–37 (2006)
137. Ghamari-Langroudi, M., Bourque, C.W.: Ionic basis of the caesium-induced depolarisation in rat supraoptic nucleus neurones. J. Physiol. **536**, 797–808 (2001)
138. Pakhomov, A.G., Kolb, J.F., White, J.A., Joshi, R.P., Xiao, S., Schoenbach, K.H.: Long-lasting plasma membrane permeabilization in mammalian cells by nanosecond pulsed electric field (nsPEF). Bioelectromagnetics **28**, 655–663 (2007)
139. Andre, F.M., Rassokhin, M.A., Bowman, A.M., Pakhomov, A.G.: Gadolinium blocks membrane permeabilization induced by nanosecond electric pulses and reduces cell death. Bioelectrochemistry **79**, 95–100 (2010)
140. Pakhomov, A.G., Shevin, R., White, J.A., Kolb, J.F., Pakhomova, O.N., Joshi, R.P., Schoenbach, K.H.: Membrane permeabilization and cell damage by ultrashort electric field shocks. Arch. Biochem. Biophys. **465**, 109–118 (2007)
141. Berridge, M.J., Lipp, P., Bootman, M.D.: The versatility and universality of calcium signalling. Nat. Rev. Mol. Cell Biol. **1**, 11–21 (2000)
142. Tolstykh, G.P., Beier, H.T., Roth, C.C., Thompson, G.L., Ibey, B.L.: 600ns pulse electric field-induced phosphatidylinositol-bisphosphate depletion. Bioelectrochemistry **100**, 80–87 (2014)

143. Tolstykh, G.P., Beier, H.T., Roth, C.C., Thompson, G.L., Payne, J.A., Kuipers, M.A., Ibey, B. L.: Activation of intracellular phosphoinositide signaling after a single 600 nanosecond electric pulse. Bioelectrochemistry **94**, 23–29 (2013)
144. Zhivotovsky, B., Orrenius, S.: Calcium and cell death mechanisms: a perspective from the cell death community. Cell Calcium **50**, 211–221 (2011)
145. Nuccitelli, R., Lui, K., Kreis, M., Athos, B., Nuccitelli, P.: Nanosecond pulsed electric field stimulation of reactive oxygen species in human pancreatic cancer cells is Ca(2+)-dependent. Biochem. Biophys. Res. Commun. **435**, 580–585 (2013)
146. Morotomi-Yano, K., Akiyama, H., Yano, K.: Nanosecond pulsed electric fields induce poly (ADP-ribose) formation and non-apoptotic cell death in HeLa S3 cells. Biochem. Biophys. Res. Commun. **438**, 557–562 (2013)
147. Ren, W., Sain, N.M., Beebe, S.J.: Nanosecond pulsed electric fields (nsPEFs) activate intrinsic caspase-dependent and caspase-independent cell death in Jurkat cells. Biochem. Biophys. Res. Commun. **421**, 808–812 (2012)
148. Pakhomova, O.N., Gregory, B., Semenov, I., Pakhomov, A.G.: Calcium-mediated pore expansion and cell death following nanoelectroporation. Biochim. Biophys. Acta **1838**, 2547–2554 (2014)
149. Pakhomova, O.N., Gregory, B.W., Semenov, I., Pakhomov, A.G.: Two modes of cell death caused by exposure to nanosecond pulsed electric field. PLoS One **8**, e70278 (2013)
150. Ibey, B.L., Pakhomov, A.G., Gregory, B.W., Khorokhorina, V.A., Roth, C.C., Rassokhin, M. A., Bernhard, J.A., Wilmink, G.J., Pakhomova, O.N.: Selective cytotoxicity of intense nanosecond-duration electric pulses in mammalian cells. Biochim. Biophys. Acta **1800**, 1210–1219 (2010)
151. Pickard, B.G.: "second extrinsic organizational mechanism" for orienting cellulose: modelling a role for the plasmalemmal reticulum. Protoplasma **233**, 1–29 (2008)
152. Nick, P.: Microtubules and the tax payer. Protoplasma **249** (Special Issue Applied Plant Cell Biology), 81–94 (2012)
153. Frey, N., Klotz, J., Nick, P.: A kinesin with calponin-homology domain is involved in premitotic nuclear migration. J. Exp. Bot. **61**, 3423–3437 (2010)
154. Murata, T., Wada, M.: Effects of centrifugation on preprophase-band formation in Adiantum (1991)
155. Nick, P.: Signalling to the microtubular cytoskeleton in plants. Int. Rev. Cytol. **184**, 33–80 (1998)
156. Klotz, J., Nick, P.: A novel actin-microtubule cross-linking kinesin, NtKCH, functions in cell expansion and division. New Phytol. **193**, 576–589 (2012)
157. Parthasarathy, M.V.: F-actin architecture in coleoptile epidermal cells. Eur. J. Cell Biol. **39**, 1–12 (1985)
158. Grabski, S., Schindler, M.: Auxins and cytokinins as antipodal modulators of elasticity within the actin network of plant cells. Plant Physiol. **110**, 965–970 (1996)
159. Grabski, S., Arnoys, E., Busch, B., Schindler, M.: Regulation of actin tension in plant cells by kinases and phosphatases. Plant Physiol. **116**, 279–290 (1998)
160. Waller, F., Nick, P.: Response of actin microfilaments during phytochrome-controlled growth of maize seedlings. Protoplasma **200**, 154–162 (1997)
161. Sonobe, S., Shibaoka, H.: Cortical fine actin filaments in higher plant cells visualized by rhodamine-phalloidin after pretreatment with m-maleimidobenzoyl-N-hydroxysuccinimide ester. Protoplasma **48**, 80–86 (1989)
162. Thimann, K.V., Reese, K., Nachmikas, V.T.: Actin and the elongation of plant cells. Protoplasma **171**, 151–166 (1992)
163. Wang, Q.Y., Nick, P.: The auxin response of actin is altered in the rice mutant Yin-Yang. Protoplasma **204**, 22–33 (1998)
164. Sano, T., Higaki, T., Oda, Y., Hayashi, T., Hasezawa, S.: Appearance of actin microfilament 'twin peaks' in mitosis and their function in cell plate formation, as visualized in tobacco BY-2 cells expressing GFP–fimbrin. Plant J. **44**, 595–605 (2005)

165. Maisch, J., Nick, P.: Actin is involved in auxin-dependent patterning. Plant Physiol. **143**, 1695–1704 (2007)
166. Traas, J.A., Doonan, J.H., Rawlins, D.J., Shaw, P.J., Watts, J., Lloyd, C.W.: An actin network is present in the cytoplasm throughout the cell cycle of carrot cells and associates with the dividing (1987)
167. Durst, S., Hedde, P.N., Brochhausen, L., Nick, P., Nienhaus, G.U., Maisch, J.: Organization of perinuclear actin in live tobacco cells observed by PALM with optical sectioning. J. Plant Physiol. **141**, 97–108 (2014)
168. Fosket, D.E., Morejohn, L.C.: Structural and functional organization of tubulin. Annu. Rev. Plant. Physiol. Plant. Mol. Biol. **43**, 201–240 (1992)
169. Meagher, R.B., Mckinney, E.C., Vitale, A.V.: The evolution of new structures: clues from plant cytoskeletal genes. Trends Genet. **15**, 278–284 (1999)
170. Meagher, R.B.: Divergence and differential expression of actin gene families in higher plants. Int. Rev. Cytol. **125**, 139–163 (1991)
171. Silflow, C.D., Oppenheimer, D.G., Kopczak, S.D., Ploense, S.E., Ludwig, S.R., Haas, N., Snustad, D.P.: Plant tubulin genes: structure and differential expression during development. Dev. Genet. **8**, 435–460 (1987)
172. Vantard, M., Levilliers, N., Hill, A.M., Adoutte, A., Lambert, A.M.: Incorporation of Paramecium axonemal tubulin into higher plant cells reveals functional sites of microtubule assembly. Proc. Natl. Acad. Sci. U. S. A. **87**, 8825–8829 (1990)
173. Zhang, D., Waldsworth, P., Hepler, P.K.: Microtubule dynamics in living dividing plant cells: confocal imaging of microinjected fluorescent brain tubulin. Proc. Natl. Acad. Sci. U. S. A. **87**, 8820–8824 (1990)
174. Yuan, M., Shaw, P.J., Warn, R.M., Lloyd, C.W.: Dynamic reorientation of cortical microtubules from transverse to longitudinal, in living cells. Proc. Natl. Acad. Sci. U. S. A. **91**, 6050–6053 (1994)
175. Himmelspach, R., Wymer, C.L., Lloyd, C.W., Nick, P.: Gravity-induced reorientation of cortical microtubules observed in vivo. Plant J. **18**, 449–453 (1999)
176. Staiger, C.J., Poulter, N.S., Henty, J.L., Franklin-Tong, V.E., Blanchoin, L.: Regulation of actin dynamics by actin-binding proteins in pollen. J. Exp. Bot. **61**, 1969–1986 (2010)
177. Struk, S., Dhonukshe, P.: MAPs: cellular navigators for microtubule array orientations in Arabidopsis. Plant Cell Rep. **33**, 1–21 (2014)
178. Cai, G., Cresti, M.: Are kinesins required for organelle trafficking in plant cells? Front. Plant Sci. **3**, 170 (2012)
179. Sparkes, I.: Recent advances in understanding plant myosin function: life in the fast lane. Mol. Plant **4**, 805–812 (2011)
180. Geiger, B., Bershadsky, A.: Assembly and mechanosensory function of focal contacts. Curr. Opin. Cell Biol. **l3**, 584–592 (2001)
181. Giancotti, G., Ruoslahti, E.: Integrin signalling. Science **285**, 1028–1032 (1999)
182. Canut, H., Carrasco, A., Galaud, J.-P., Cassan, C., Bouyssou, H., Vita, N., Ferrara, P., Pont-Lezica, R.: High affinity RGD-binding sites at the plasma membrane of Arabidopsis thaliana links the cell wall. Plant J. **16**, 63–71 (1998)
183. Wang, X., Zhua, L., Liu, B., Wang, J., Zhao, L., Yuan, M.: Arabidopsis microtubule associated protein 18 functions in directional cell growth by destabilizing cortical microtubules. Plant Cell **19**, 877–839 (2007)
184. Zaban, B., Maisch, J., Nick, P.: Dynamic actin controls polarity induction de novo in protoplasts. J. Int. Plant Biol. **55**, 142–159 (2013)
185. Baluška, F., Šamaj, J., Wojtaszek, P., Volkmann, D., Menzel, D.: Cytoskeleton-plasma membrane-cell wall continuum in plants. Emerging links revisited. Plant Physiol. **133**, 482–419 (2003)
186. Gittes, F., Mickey, B., Nettleton, J., Howard, J.: Flexural rigidity of microtubules and actin filaments measured from thermal fluctuations in shape. J. Cell Biol. **120**, 923–934 (1993)

187. Ingber, D.E.: Tensegrity l: cell structure and hierarchical systems biology. J. Cell Sci. **116**, 1157–1173 (2003)
188. Ingber, D.E.: Tensegrity II: how structural networks influence cellular information processing networks. J. Cell Sci. **116**, 1397–1403 (2003)
189. Green, P.B.: Organogenesis—a biophysical view. Annu. Rev. Plant. Physiol. Plant. Mol. Biol. **3**, 51–82 (1980)
190. Green, P.B.: Mechanism for plant cellular morphogenesis. Science **138**, 1401–1405 (1962)
191. Ledbetter, M.C., Porter, K.R.: A microtubule in plant cell fine structure. J. Cell Biol. **12**, 239–250 (1963)
192. Geitmann, A., Ortega, J.K.: Mechanics and modeling of plant cell growth. Trends Plant Sci. **14**, 467–478 (2009)
193. Nick, P.: Control of cell axis. In: Nick, P. (ed.) Plant Microtubules. Plant cell monogr, vol. 143, pp. 3–46. (2008)
194. Heath, I.B.: A unified hypothesis for the role of membrane bound enzyme complexes and microtubules in plant cell wall synthesis. J. Theor. Biol. **48**, 445–449 (1974)
195. Bichet, A., Desnos, T., Turner, S., Grandjean, O., Höfte, H.: BOTERO1 is required for normal orientation of cortical microtubules and anisotropic cell expansion in Arabidopsis. Plant J. **25**, 137–148 (2001)
196. Zhong, R., Burk, D.H., Morrison, W.H., Ye, Z.H.: A kinesin-like protein is essential for oriented deposition of cellulose microfibrils and cell wall strength. Plant Cell **14**, 3101–3117 (2002)
197. Paredez, A.R., Somerville, C.R., Ehrhardt, D.W.: Visualization of cellulose synthase demonstrates functional association with microtubules. Science **312**, 1491–1495 (2006)
198. Li, S., Lei, L., Somerville, C.R., Gua, Y.: Cellulose synthase interactive protein 1 (CSI1) links microtubules and cellulose synthase complexes. Proc. Natl. Acad. Sci. U. S. A. **109**, 185–190 (2012)
199. Los, D.A., Murata, N.: Membrane fluidity and its roles in the perception of environmental signals. Biochim. Biophys. Acta **1666**, 142–157 (2004)
200. Fischer, K., Schopfer, P.: Physical strain-mediated microtubule reorientation in the epidermis of gravitropically or phototropically stimulated maize coleoptiles. Plant J. **15**, 119–123 (1998)
201. Turing, A.M.: The chemical basis of morphogenesis. Philos. Trans. R. Soc. Lond. B Biol. **237**, 37–72 (1952)
202. Akhmanova, A., Steinmetz, M.O.: Tracking the ends: a dynamic protein network controls the fate of microtubule tips. Nat. Rev. Mol. Cell Biol. **9**, 309–322 (2008)
203. Savage, C., Hamelin, M., Culotti, J.G., Coulson, A., Albertson, D.G., Chalfie, M.: mec-7 is a β-tubulin gene required for the production of 15-protofilament microtubules in Caenorhabditis elegans. Genes Dev. **3**, 870–881 (1989)
204. Ding, J.P., Pickard, B.G.: Mechanosensory calcium-selective cation channels in epidermal cells. Plant J. **3**, 83–110 (1993)
205. Mazars, C., Thion, L., Thuleau, P., Graziana, A., Knight, M.R., Moreau, M., Ranjeva, R.: Organization of cytoskeleton controls the changes in cytosolic calcium of cold-shocked Nicotiana plumbaginifolia protoplasts. Cell Calcium **22**, 413–420 (1997)
206. Komis, G., Apostolakos, P., Galatis, B.: Hyperosmotic stress induces formation of tubulin macrotubules in root-tip cells of Triticum turgidum: their probable involvement in protoplast volume control. Plant Cell Physiol. **43**, 911–922 (2002)
207. Wang, S., Kurepa, J., Hashimoto, T., Smalle, J.A.: Salt stress induced disassembly of Arabidopsis cortical microtubule arrays involves 26S proteasome-dependent degradation of SPIRAL1. Plant Cell **23**, 3412–3427 (2011)
208. Guo, L., Devaiah, S.P., Narasimhan, R., Pan, X., Zhang, Y., Zhang, W., Wang, X.: Cytosolic glyceraldehyde-3-phosphate dehydrogenases interact with phospholipase Dδ to transduce hydrogen peroxide signals in the Arabidopsis response to stress. Plant Cell **24**, 2200–2212 (2012)

209. Nick, P.: Microtubules, and signalling in abiotic stress. Plant J. **75**, 309–323 (2013)
210. Mathur, J., Mathur, N., Hülskamp, M.: Simultaneous visualization of peroxisomes and cytoskeletal elements reveals actin and not microtubule-based peroxisome motility in plants. Plant Physiol. **128**, 1031–1045 (2002)
211. Kadota, A., Yamada, N., Suetsugu, N., Hirose, M., Saito, S., Shoda, K.: Short actin-based mechanism for light-directed chloroplast movement in Arabidopsis. Proc. Natl. Acad. Sci. U. S. A. **106**, 13106–13111 (2009)
212. Van Gestel, K., Kohler, R.H., Verbelen, J.P.: Plant mitochondria move on F-actin, but their positioning in the cortical cytoplasm depends on both F-actin and microtubules. J. Exp. Bot. **53**, 659–667 (2002)
213. Boevink, P., Oparka, K., Santa Cruz, S., Martin, B., Betteridge, A., Hawes, C.: Stacks on tracks: the plant Golgi apparatus traffics on an actin/ER network. Plant J. **15**, 441–447 (2002)
214. Rosazza, C., Escoffre, J.M., Zumbusch, A., Rols, M.P.: The actin cytoskeleton has an active role in the electrotransfer of plasmid DNA in mammalian cells. Mol. Ther. **19**, 913–921 (2011)
215. Sheahan, M.B., Rose, R.J., McCurdy, D.W.: Actin-filament-dependent remodeling of the vacuole in cultured mesophyll protoplasts. Protoplasma **230**, 141–152 (2007)
216. Waller, F., Riemann, M., Nick, P.: A role for actin-driven secretion in auxin-induced growth. Protoplasma **219**, 72–81 (2002)
217. Nick, P.: Probing the actin-auxin oscillator. Plant Signal. Behav. **5**, 4–9 (2010)
218. Nick, P., Han, M., An, G.: Auxin stimulates its own transport by actin reorganization. Plant Physiol. **151**, 155–167 (2009)
219. Jones, J.D., Dangl, J.L.: The plant immune system. Nature **444**, 323–329 (2006)
220. Qiao, F., Chang, X.L., Nick, P.: The cytoskeleton enhances gene expression in the response to the Harpin elicitor in grapevine. J. Exp. Bot. **61**, 4021–4031 (2010)
221. Chang, X., Heene, E., Qiao, F., Nick, P.: The phytoalexin resveratrol regulates the initiation of hypersensitive cell death in Vitis cells. PLoS One **6**, e26405 (2011)
222. Guan, X., Buchholz, G., Nick, P.: The cytoskeleton is disrupted by the bacterial effector HrpZ, but not by the bacterial PAMP flg22, in tobacco BY-2 cells. J. Exp. Bot. **64**, 1805–1816 (2013)
223. Gourlay, C.W., Ayscough, K.R.: The actin cytoskeleton: a key regulator of apoptosis and ageing? Nat. Rev. Mol. Cell Biol. **6**, 583–589 (2005)
224. Franklin-Tong, V.E., Gourlay, C.W.: A role for actin in regulating apoptosis/programmed cell death: evidence spanning yeast, plants and animals. Biochem. J. **413**, 389–404 (2008)
225. Smertenko, A., Franklin-Tong, V.E.: Organisation and regulation of the cytoskeleton in plant programmed cell death. Cell Death Diff. **18**, 1263–1270 (2011)
226. Smertenko, A., Bozhkov, P.: The life and death signalling underlying cell fate determination during somatic embryogenesis. Plant Cell Monogr. **22**, 131–178 (2014)
227. Mathur, J., Radhamony, R., Sinclair, A.M., Donoso, A., Dunn, N., Roach, E.: mEosFP-based green-to-red photoconvertible subcellular probes for plants. Plant Physiol. **154**, 1573–1587 (2010)
228. Opatrný, Z., Nick, P., Petrášek, J.: Plant Cell Strains in Fundamental Research and Applications Plant Cell Monographs, vol. 22, pp. 455–481. Springer, Heidelberg (2014)
229. Berghöfer, T., Eing, C., Flickinger, B., Hohenberger, P., Wegner, L., Frey, W., Nick, P.: Nanosecond electric pulses trigger actin responses in plant cells. Biochem. Biophys. Res. Commun. **387**, 590–595 (2009)
230. Hohenberger, P., Eing, C., Straessner, R., Durst, S., Frey, W., Nick, P.: Plant actin controls membrane permeability. BBA Membr. **1808**, 2304–2312 (2011)
231. Kühn, S., Liu, Q., Eing, C., Wüstner, R., Nick, P.: Nanosecond electric pulses target to a plant-specific kinesin at the plasma membrane. J. Membr. Biol. **246**, 927–938 (2013)
232. Campanoni, P., Blasius, B., Nick, P.: Auxin transport synchronizes the pattern of cell division in a tobacco cell line. Plant Physiol. **133**, 1251–1260 (2003)

233. Beebe, S.J., Fox, P.M., Rec, L.J., Somers, K., Stark, R.H., Schoenbach, K.H.: Nanosecond pulsed electric field (nsPEF) effects on cells and tissues: apoptosis induction and tumor growth inhibition. IEEE Trans. Plasma Sci. **30**, 286–292 (2002)
234. Buescher, E.S., Schoenbach, K.H.: Effects of submicrosecond, high intensity pulsed electric fields on living cells—intracellular electromanipulation. IEEE Trans. Dielectr. Electr. Insul. **10**, 5788–5794 (2003)
235. Chen, C., Smye, S.W., Robinson, M.P., Evans, J.A.: Membrane electroporation theories: a review. Med. Biol. Eng. Comput. **44**, 5–14 (2006)
236. Gowrishankar, T.R., Esser, A.T., Vasilkoski, Z.V., Smith, K.C., Weaver, J.C.: Microdosimetry for conventional and supra-electroporation in cells with organelles. Biochem. Biophys. Res. Commun. **310**, 1266–1276 (2006)
237. Schoenbach, K.H., Joshi, R.P., Chen, C., Kolb, J.F., Chen, N., Stacye, M., Blackmore, P., Buescher, E.S., Beebe, S.J.: Ultrashort electrical pulses open a new gateway into biological cells. Proc. IEEE **92**, 1122–1137 (2004)
238. Beebe, S.J., Fox, P.M., Rec, L.J., Willis, E.L., Schoenbach, K.H.: Nanosecond high-intensity pulsed electric fields induce apoptosis in human cells. FASEB J. **17**, 1493–1495 (2003)
239. Hu, Q., Joshi, P.R., Schoenbach, K.H.: Simulation of nanopore formation and phosphatidylserine externalization in lipid membranes subjected to a high-intensity, ultrashort electric pulses. Phys. Rev. E. **72**, 031902 (2005)
240. Flickinger, B., Berghöfer, T., Hohenberger, P., Eing, C., Frey, W.: Transmembrane potential measurements on plant cells using the voltage-sensitive dye ANNINE-6. Protoplasma **247**, 3–12 (2010)
241. Ibey, B.L., Roth, C.C., Pakhomov, A.G., Bernhard, J.A., Wilmink, G.J., Pakhomova, O.N.: Dose-dependent thresholds of 10-ns electric pulse induced plasma membrane disruption and cytotoxicity in multiple cell lines. PLoS One **6**, e15642 (2011)
242. Breton, M., Delemotte, L., Silve, A., Mir, L.M., Tarek, M.: Transport of siRNA through lipid membranes driven by nanosecond electric pulses: an experimental and computational study. J. Am. Chem. Soc. **134**, 13938–13941 (2012)
243. Preuss, M.L., Kovar, D.R., Lee, Y.R., Staiger, C.J., Delmer, D.P., Liu, B.: A plant-specific kinesin binds to actin microfilaments and interacts with cortical microtubules in cotton fibers. Plant Physiol. **136**, 945–3955 (2004)
244. Huang, B., Babcock, H., Zhuang, X.: Breaking the diffraction barrier: super-resolution imaging of cells. Cell **143**, 1047–1058 (2010)
245. Sparkes, I.A., Graumann, K., Martinière, A., Schoberer, J., Wang, P., Osterrieder, A.: Bleach it, switch it, bounce it, pull it: using lasers to reveal plant cell dynamics. J. Exp. Bot. **62**, 1–7 (2011)
246. Wolfe, J., Dowgert, M.F., Steponkus, P.L.: Dynamics of membrane exchange of the plasma membrane and the lysis of isolated protoplasts during rapid expansions in area. J. Membr. Biol. **86**, 127–138 (1985)
247. Liu, Q., Qiao, F., Ismail, A., Chang, X., Nick, P.: The plant cytoskeleton controls regulatory volume increase. BBA Membr. **1828**, 2111–2120 (2013)
248. Kusaka, N., Maisch, J., Nick, P., Hayashi, K.I., Nozaki, H.: Manipulation of intercellular auxin in a single cell by light with esterase-resistant caged auxins. Chembiochem **10**, 2195–2202 (2009)
249. Durst, S., Nick, P., Maisch, J.: Actin-depolymerizing factor 2 is involved in auxin dependent patterning. J. Plant Physiol. **170**, 1057–1066 (2013)
250. Thompson, G.L., Roth, C., Tolstykh, G., Kuipers, M., Ibey, B.L.: Disruption of the actin cortex contributes to susceptibility of mammalian cells to nanosecond pulsed electric fields. Bioelectromagnetics **35**, 262–272 (2014)
251. Stacey, M., Fox, P., Buescher, S., Kolb, J.: Nanosecond pulsed electric field induced cytoskeleton, nuclear membrane and telomere damage adversely impact cell survival. Bioelectrochemistry **82**, 131–134 (2011)

252. Kanthou, C., Kranjc, S., Sersa, G., Tozer, G., Zupanic, A., Cemazar, M.: The endothelial cytoskeleton as a target of electroporation-based therapies. Mol. Cancer Ther. **5**, 3145–3152 (2006)
253. Teissie, J., Rols, M.P.: Manipulation of cell cytoskeleton affects the lifetime of cell membrane electropermeabilization. Ann. N. Y. Acad. Sci. **720**, 98–110 (1994)
254. Chopinet, L., Batista-Napotnik, T., Montigny, A.: Nanosecond electric pulse effects on gene expression. J. Membr. Biol. **246**, 851–859 (2013)
255. Pakhomov, A.G., Xiao, S., Pakhomova, O.N., Semenov, I., Kuipers, M.A., Ibey, B.L.: Disassembly of actin structures by nanosecond pulsed electric field is a downstream effect of cell swelling. Bioelectrochemistry **100**, 88–95 (2014)
256. Gruenheid, S., Finlay, B.B.: Microbial pathogenesis and cytoskeletal function. Nature **422**, 775–781 (2003)
257. Marsh, M., Bron, R.: SFV infection in CHO cells: cell-type specific restrictions to productive virus entry at the cell surface. J. Cell Sci. **110**(Pt 1), 95–103 (1997)
258. Dauty, E., Verkman, A.S.: Actin cytoskeleton as the principal determinant of size-dependent DNA mobility in cytoplasm: a new barrier for non-viral gene delivery. J. Biol. Chem. **280**, 7823–7828 (2005)
259. Badding, M.A., Lapek, J.D., Friedman, A.E., Dean, D.A.: Proteomic and functional analyses of protein-DNA complexes during gene transfer. Mol. Ther. **21**, 775–785 (2013)
260. Chambers, R.: The micromanipulation of living cells. In: Moulton, F.R. (ed.) The Cell and Protoplasm, pp. 20–30. Science press, Washington, DC (1940)
261. Lukacs, G.L., Haggie, P., Seksek, O., Lechardeur, D., Freedman, N., Verkman, A.S.: Size-dependent DNA mobility in cytoplasm and nucleus. J. Biol. Chem. **275**, 1625–1629 (2000)
262. Seksek, O., Biwersi, J., Verkman, A.S.: Translational diffusion of macromolecule-sized solutes in cytoplasm and nucleus. J. Cell Biol. **138**, 131–142 (1997)
263. Badding, M.A., Dean, D.A.: Highly acetylated tubulin permits enhanced interactions with and trafficking of plasmids along microtubules. Gene Ther. **20**, 616–624 (2013)
264. Badding, M.A., Vaughan, E.E., Dean, D.A.: Transcription factor plasmid binding modulates microtubule interactions and intracellular trafficking during gene transfer. Gene Ther. **19**, 338–346 (2012)
265. Geiger, R.C., Taylor, W., Glucksberg, M.R., Dean, D.A.: Cyclic stretch-induced reorganization of the cytoskeleton and its role in enhanced gene transfer. Gene Ther. **13**, 725–731 (2006)
266. Vaughan, E.E., Dean, D.A.: Intracellular trafficking of plasmids during transfection is mediated by microtubules. Mol. Ther. **13**, 422–428 (2006)
267. Vaughan, E.E., Geiger, R.C., Miller, A.M., Loh-Marley, P.L., Suzuki, T., Miyata, N., Dean, D.A.: Microtubule acetylation through HDAC6 inhibition results in increased transfection efficiency. Mol. Ther. **16**, 1841–1847 (2008)
268. Mesika, A., Kiss, V., Brumfeld, V., Ghosh, G., Reich, Z.: Enhanced intracellular mobility and nuclear accumulation of DNA plasmids associated with a karyophilic protein. Hum. Gene Ther. **16**, 200–208 (2005)
269. Leopold, P.L., Kreitzer, G., Miyazawa, N., Rempel, S., Pfister, K.K., Rodriguez-Boulan, E., Crystal, R.G.: Dynein- and microtubule-mediated translocation of adenovirus serotype 5 occurs after endosomal lysis. Hum. Gene Ther. **11**, 151–165 (2000)
270. Miller, A.M., Munkonge, F.M., Alton, E.W., Dean, D.A.: Identification of protein cofactors necessary for sequence-specific plasmid DNA nuclear import. Mol. Ther. **17**, 1897–1903 (2009)
271. Munkonge, F.M., Amin, V., Hyde, S.C., Green, A.M., Pringle, I.A., Gill, D.R., Smith, J.W., Hooley, R.P., Xenariou, S., Ward, M.A., Leeds, N., Leung, K.Y., Chan, M., Hillery, E., Geddes, D.M., Griesenbach, U., Postel, E.H., Dean, D.A., Dunn, M.J., Alton, E.W.: Identification and functional characterization of cytoplasmic determinants of plasmid DNA nuclear import. J. Biol. Chem. **284**, 26978–26987 (2009)
272. Dean, D.A.: Import of plasmid DNA into the nucleus is sequence specific. Exp. Cell Res. **230**, 293–302 (1997)

273. Dean, D.A., Dean, B.S., Muller, S., Smith, L.C.: Sequence requirements for plasmid nuclear entry. Exp. Cell Res. **253**, 713–722 (1999)
274. Vacik, J., Dean, B.S., Zimmer, W.E., Dean, D.A.: Cell-specific nuclear import of plasmid DNA. Gene Ther. **6**, 1006–1014 (1999)
275. Langle-Rouault, F., Patzel, V., Benavente, A., Taillez, M., Silvestre, N., Bompard, A., Sczakiel, G., Jacobs, E., Rittner, K.: Up to 100-fold increase of apparent gene expression in the presence of Epstein-Barr virus oriP sequences and EBNA1: implications of the nuclear import of plasmids. J. Virol. **72**, 6181–6185 (1998)
276. Mesika, A., Grigoreva, I., Zohar, M., Reich, Z.: A regulated, NFkappaB-assisted import of plasmid DNA into mammalian cell nuclei. Mol. Ther. **3**, 653–657 (2001)
277. Degiulio, J.V., Kaufman, C.D., Dean, D.A.: The SP-C promoter facilitates alveolar type II epithelial cell-specific plasmid nuclear import and gene expression. Gene Ther. **17**, 541–549 (2010)
278. Sacramento, C.B., Moraes, J.Z., Denapolis, P.M., Han, S.W.: Gene expression promoted by the SV40 DNA targeting sequence and the hypoxia-responsive element under normoxia and hypoxia. Braz. J. Med. Biol. Res. **43**, 722–727 (2010)
279. Cramer, F., Christensen, C.L., Poulsen, T.T., Badding, M.A., Dean, D.A., Poulsen, H.S.: Insertion of a nuclear factor kappa B DNA nuclear-targeting sequence potentiates suicide gene therapy efficacy in lung cancer cell lines. Cancer Gene Ther. **19**, 675–683 (2012)
280. Wente, S.R., Rout, M.P.: The nuclear pore complex and nuclear transport. Cold Spring Harb. Perspect. Biol. **2**, a000562 (2010)
281. Wilson, G.L., Dean, B.S., Wang, G., Dean, D.A.: Nuclear import of plasmid DNA in digitonin-permeabilized cells requires both cytoplasmic factors and specific DNA sequences. J. Biol. Chem. **274**, 22025–22032 (1999)
282. Colin, M., Moritz, S., Fontanges, P., Kornprobst, M., Delouis, C., Keller, M., Miller, A.D., Capeau, J., Coutelle, C., Brahimi-Horn, M.C.: The nuclear pore complex is involved in nuclear transfer of plasmid DNA condensed with an oligolysine-RGD peptide containing nuclear localisation properties. Gene Ther. **8**, 1643–1653 (2001)
283. Sebestyén, M.G., Ludtke, J.L., Bassik, M.C., Zhang, G., Budker, V., Lukhtanov, E.A., Hagstrom, J.E., Wolff, J.A.: DNA vector chemistry: the covalent attachment of signal peptides to plasmid DNA. Nat. Biotechnol. **16**, 80–85 (1998)
284. Swindle, C.S., Zou, N., Van Tine, B.A., Shaw, G.M., Engler, J.A., Chow, L.T.: Human papillomavirus DNA replication compartments in a transient DNA replication system. J. Virol. **73**, 1001–1009 (1999)
285. Tang, Q., Bell, P., Tegtmeyer, P., Maul, G.G.: Replication but not transcription of simian virus 40 DNA is dependent on nuclear domain 10. J. Virol. **74**, 9694–9700 (2000)
286. Ondrej, V., Kozubek, S., Lukasova, E., Falk, M., Matula, P., Matula, P., Kozubek, M.: Directional motion of foreign plasmid DNA to nuclear HP1 foci. Chromosome Res. **14**, 505–514 (2006)
287. Gasiorowski, J.Z., Dean, D.A.: Intranuclear trafficking of episomal DNA is transcription-dependent. Mol. Ther. **15**, 2132–2139 (2007)
288. Kopp, K., Gasiorowski, J.Z., Chen, D., Gilmore, R., Norton, J.T., Wang, C., Leary, D.J., Chan, E.K., Dean, D.A., Huang, S.: Pol I transcription and pre-rRNA processing are coordinated in a transcription-dependent manner in mammalian cells. Mol. Biol. Cell **18**, 394–403 (2007)
289. Xu, M., Cook, P.R.: Similar active genes cluster in specialized transcription factories. J. Cell Biol. **181**, 615–623 (2008)
290. Larkin, J.D., Papantonis, A., Cook, P.R.: Promoter type influences transcriptional topography by targeting genes to distinct nucleoplasmic sites. J. Cell Sci. **126**, 2052–2059 (2013)
291. Alberts, B., Johnson, A., Lewis, J., Morgan, D., Raff, M., Roberts, K., Walter, P.: Molecular Biology of the Cell, 6th edn. Garland Publishing, New York (2014)
292. Kyriakis, J.M., Avruch, J.: Mammalian mitogen-activated protein kinase signal transduction pathways activated by stress and inflammation. Physiol. Rev. **81**, 807–869 (2001)

293. Morotomi-Yano, K., Akiyama, H., Yano, K.: Nanosecond pulsed electric fields activate MAPK pathways in human cells. Arch. Biochem. Biophys. **515**, 99–106 (2011)
294. Hardie, D.G.: AMP-activated protein kinase: an energy sensor that regulates all aspects of cell function. Genes Dev. **25**, 1895–1908 (2011)
295. Morotomi-Yano, K., Akiyama, H., Yano, K.: Nanosecond pulsed electric fields activate AMP-activated protein kinase: implications for calcium-mediated activation of cellular signaling. Biochem. Biophys. Res. Commun. **428**, 371–375 (2012)
296. Morotomi-Yano, K., Oyadomari, S., Akiyama, H., Yano, K.: Nanosecond pulsed electric fields act as a novel cellular stress that induces translational suppression accompanied by eIF2alpha phosphorylation and 4E-BP1 dephosphorylation. Exp. Cell Res. **318**, 1733–1744 (2012)
297. Wek, R.C., Jiang, H.Y., Anthony, T.G.: Coping with stress: eIF2 kinases and translational control. Biochem. Soc. Trans. **34**, 7–11 (2006)
298. Mir, L.M., Glass, L.F., Sersa, G., Teissie, J., Domenge, C., Miklavčič, D., Jaroszeski, M.J., Orlowski, S., Reintgen, D.S., Rudolf, Z., et al.: Effective treatment of cutaneous and subcutaneous malignant tumours by electrochemotherapy. Br. J. Cancer **77**(12), 2336–2342 (1998)
299. Mir, L.M., Bureau, M.F., Gehl, J., Rangara, R., Rouy, D., Caillaud, J.-M., Delaere, P., Branellec, D., Schwartz, B., Scherman, D.: High-efficiency gene transfer into skeletal muscle mediated by electric pulses. Proc. Natl. Acad. Sci. **96**(8), 4262–4267 (1999)
300. Larkin, J.O., Collins, C.G., Aarons, S., Tangney, M., Whelan, M., O'Reily, S., Breathnach, O., Soden, D.M., O'Sullivan, G.C.: Electrochemotherapy: aspects of preclinical development and early clinical experience. Ann. Surg. **245**(3), 469 (2007)
301. Davalos, R.V., Mir, L.M., Rubinsky, B.: Tissue ablation with irreversible electroporation. Ann. Biomed. Eng. **33**(2), 223–231 (2005)
302. Edd, J.F., Horowitz, L., Davalos, R.V., Mir, L.M., Rubinsky, B.: In vivo results of a new focal tissue ablation technique: irreversible electroporation. IEEE Trans. Biomed. Eng. **53**(7), 1409–1415 (2006)
303. Al-Sakere, B., Andre, F., Bernat, C., Connault, E., Opolon, P., Davalos, R.V., Rubinsky, B., Mir, L.M.: Tumor ablation with irreversible electroporation. PLoS One **2**(11), e1135 (2007)
304. Pucihar, G., Krmelj, J., Rebersek, M., Napotnik, T.B., Miklavčič, D.: Equivalent pulse parameters for electroporation. IEEE Trans. Biomed. Eng. **58**(11), 3279–3288 (2011). doi: 3210.1109/TBME.2011.2167232. Epub 2162011 Sep 2167236
305. Rubinsky, J., Onik, G., Mikus, P., Rubinsky, B.: Optimal parameters for the destruction of prostate cancer using irreversible electroporation. J. Urol. **180**(6), 2668–2674 (2008). Epub 2008 Oct 2631
306. Jiang, C., Shao, Q., Bischof, J.: Pulse timing during irreversible electroporation achieves enhanced destruction in a hindlimb model of cancer. Ann. Biomed. Eng. **1**, 1 (2014)
307. Appelbaum, L., Ben-David, E., Faroja, M., Nissenbaum, Y., Sosna, J., Goldberg, S.N.: Irreversible electroporation ablation: creation of large-volume ablation zones in in vivo porcine liver with four-electrode arrays. Radiology **270**(2), 416–424 (2014)
308. Diller, K.R.: Modeling of bioheat transfer processes at high and low temperatures. Adv. Heat Transf. **22**, 157–357 (1992)
309. Davalos, R.V., Rubinsky, B.: Temperature considerations during irreversible electroporation. Int. J. Heat Mass Transf. **51**(23), 5617–5622 (2008)
310. Thomsen, S., Pearce. J.A.: Thermal damage and rate processes in biologic tissues. In: Optical-Thermal Response of Laser-Irradiated Tissue, pp. 487–549. Springer, Dordrecht (2011)
311. Davalos, R.V., Rubinsky, B., Mir, L.M.: Theoretical analysis of the thermal effects during in vivo tissue electroporation. Bioelectrochemistry **61**(1–2), 99–107 (2003)
312. Neal II, R.E., Davalos, R.V.: The feasibility of irreversible electroporation for the treatment of breast cancer and other heterogeneous systems. Ann. Biomed. Eng. **37**(12), 2615–2625 (2009)

313. Županič, A., Miklavčič, D.: Tissue heating during tumor ablation with irreversible electroporation. Electrotechnol. Rev. **78**, 42–47 (2011)
314. Garcia, P.A., Rossmeisl, J.H., Neal, R.E., Ellis, T.L., Davalos, R.V.: A parametric study delineating irreversible electroporation from thermal damage based on a minimally invasive intracranial procedure. Biomed. Eng. Online **10**(1), 34 (2011)
315. Shafiee, H., Garcia, P.A., Davalos, R.V.: A preliminary study to delineate irreversible electroporation from thermal damage using the arrhenius equation. J. Biomech. Eng. **131** (7), 074509 (2009)
316. Garcia, P.A., Davalos, R.V., Miklavčič, D.: A numerical investigation of the electric and thermal cell kill distributions in electroporation-based therapies in tissue. PLoS One **9**(8), e103083 (2014)
317. Qin, Z., Jiang, J., Long, G., Lindgren, B., Bischof, J.C.: Irreversible electroporation: an in vivo study with dorsal skin fold chamber. Ann. Biomed. Eng. **41**(3), 619–629 (2013)
318. Garcia, P., Rossmeisl, J., Neal, R., Ellis, T., Olson, J., Henao-Guerrero, N., Robertson, J., Davalos, R.: Intracranial nonthermal irreversible electroporation: in vivo analysis. J. Membr. Biol. **236**(1), 127–136 (2010)
319. Long, G., Bakos, G., Shires, P.K., Gritter, L., Crissman, J.W., Harris, J.L., Clymer, J.W.: Histological and finite element analysis of cell death due to irreversible electroporation. Technol. Cancer Res. Treat. **13**(6), 561–569 (2014)
320. Neal 2nd, R.E., Rossmeisl Jr., J.H., Garcia, P.A., Lanz, O.I., Henao-Guerrero, N., Davalos, R. V.: Successful treatment of a large soft tissue sarcoma with irreversible electroporation. J. Clin. Oncol. Off. J. Am. Soc. Clin. Oncol. **29**(13), e372–e377 (2011)
321. Bower, M., Sherwood, L., Li, Y., Martin, R.: Irreversible electroporation of the pancreas: definitive local therapy without systemic effects. J. Surg. Oncol. **104**(1), 22–28 (2011)
322. Neal 2nd, R.E., Millar, J.L., Kavnoudias, H., Royce, P., Rosenfeldt, F., Pham, A., Smith, R., Davalos, R.V., Thomson, K.R.: In vivo characterization and numerical simulation of prostate properties for non-thermal irreversible electroporation ablation. Prostate **74**(5), 458–468 (2014)
323. Edd, J.F., Davalos, R.V.: Mathematical modeling of irreversible electroporation for treatment planning. Technol. Cancer Res. Treat. **6**(4), 275–286 (2007)
324. Ben-David, E., Ahmed, M., Faroja, M., Moussa, M., Wandel, A., Sosna, J., Appelbaum, L., Nissenbaum, I., Goldberg, S.N.: Irreversible electroporation: treatment effect is susceptible to local environment and tissue properties. Radiology **11**, 11 (2013)
325. Neal II, R.E., Singh, R., Hatcher, H.C., Kock, N.D., Torti, S.V., Davalos, R.V.: Treatment of breast cancer through the application of irreversible electroporation using a novel minimally invasive single needle electrode. Breast Cancer Res. Treat. **123**(1), 295–301 (2010)
326. Corovic, S., Zupanic, A., Kranjc, S., Al Sakere, B., Leroy-Willig, A., Mir, L.M., Miklavčič, D.: The influence of skeletal muscle anisotropy on electroporation: in vivo study and numerical modeling. Med. Biol. Eng. Comput. **48**(7), 637–648 (2010)
327. Neal II, R., Smith, R., Kavnoudias, H., Rosenfeldt, F., Ou, R., Mclean, C., Davalos, R., Thomson, K.: The effects of metallic implants on electroporation therapies: feasibility of irreversible electroporation for brachytherapy salvage. Cardiovasc. Interv. Radiol. **36**(6), 1638–1645 (2013)
328. Duck, F.A.: Physical Properties of Tissue: A Comprehensive Reference Book. Academic, New York (1990)
329. Neal II, R.E., Garcia, P.A., Robertson, J.L., Davalos, R.V.: Experimental characterization and numerical modeling of tissue electrical conductivity during pulsed electric fields for irreversible electroporation treatment planning. IEEE Trans. Biomed. Eng. **59**(4), 1076–1085 (2012). Epub 2012 Jan 1076
330. Osswald, K.: Messung der Leitfähigkeit und Dielektrizitätskonstante biologischer Gewebe und Flüssigkeiten bei kurzen Wellen. Akad. Verlagsges. (1937)
331. Mcrae, D.A., Esrick, M.A.: The dielectric parameters of excised EMT-6 tumours and their change during hyperthermia. Phys. Med. Biol. **37**(11), 2045 (1992)

332. Sel, D., Cukjati, D., Batiuskaite, D., Slivnik, T., Mir, L.M., Miklavčič, D.: Sequential finite element model of tissue electropermeabilization. IEEE Trans. Biomed. Eng. **52**(5), 816–827 (2005)
333. Ivorra, A., Rubinsky, B.: In vivo electrical impedance measurements during and after electroporation of rat liver. Bioelectrochemistry **70**(2), 287–295 (2007)
334. Pavšelj, N., Miklavčič, D.: Numerical modeling in electroporation-based biomedical applications. Radiol. Oncol. **42**(3), 159–168 (2008)
335. Ivorra, A., Mir, L.M., Rubinsky, B.: Electric field redistribution due to conductivity Changes during tissue electroporation: experiments with a simple vegetal model. In: IFMBE Proceedings, vol. 25/13, edn, pp. 59–62. Springer, Berlin/Heidelberg (2009)
336. Corovic, S., Lackovic, I., Sustaric, P., Sustar, T., Rodic, T., Miklavčič, D.: Modeling of electric field distribution in tissues during electroporation. Biomed. Eng. Online **12**(1), 16 (2013)
337. Neal, R.E., Garcia, P.A., Kavnoudias, H., Rosenfeldt, F., Mclean, C.A., Earl, V., Bergman, J., Davalos, R.V., Thomson, K.R.: In vivo irreversible electroporation kidney ablation: experimentally correlated numerical models. IEEE Trans. Biomed. Eng. **62**(2), 561–569 (2015). doi: 510.1109/TBME.2014.2360374. Epub 2362014 Sep 2360325
338. Gaylor, D.C., Prakah-Asante, K., Lee, R.C.: Significance of cell size and tissue structure in electrical trauma. J. Theor. Biol. **133**(2), 223–237 (1988)
339. Neal II, R.E., Rossmeisl Jr., J.H., Garcia, P.A., Lanz, O.I., Henao-Guerrero, N., Davalos, R. V.: Successful treatment of a large soft tissue sarcoma with irreversible electroporation. J. Clin. Oncol. **29**(13), e372–e377 (2011)
340. Wimmer, T., Srimathveeravalli, G., Gutta, N., Ezell, P.C., Monette, S., Maybody, M., Erinjery, J.P., Durack, J.C., Coleman, J.A., Solomon, S.B.: Planning irreversible electroporation in the porcine kidney: are numerical simulations reliable for predicting empiric ablation outcomes? Cardiovasc. Intervent. Radiol. **38**(1), 182–190 (2015)
341. Miklavčič, D., Semrov, D., Mekid, H., Mir, L.M.: A validated model of in vivo electric field distribution in tissues for electrochemotherapy and for DNA electrotransfer for gene therapy. Biochim. Biophys. Acta **1523**(1), 73–83 (2000)
342. Wimmer, T., Srimathveeravalli, G., Gutta, N., Ezell, P.C., Monette, S., Kingham, T.P., Maybody, M., Durack, J.C., Fong, Y., Solomon, S.B.: Comparison of simulation-based treatment planning with imaging and pathology outcomes for percutaneous CT-guided irreversible electroporation of the porcine pancreas: a pilot study. J. Vasc. Interv. Radiol. **24**(11), 1709–1718 (2013)
343. Majno, G., Joris, I.: Apoptosis, oncosis, and necrosis: an overview of cell death. Am. J. Pathol. **146**, 3–15 (1995)
344. Galluzzi, L., Bravo-San Pedro, J.M., Vitale, I., Aaronson, S.A., Abrams, J.M., Adam, D., et al. (2014a) Essential versus accessory aspects of cell death: recommendations of the NCCD 2015. Cell Death Differ. 2014 Sept 19. doi: 10.1038/cdd.2014.137
345. Galluzzi, L., Kepp, O., Krautwald, S., Kroemer, G., Linkermann, A.: Molecular mechanisms of regulated necrosis. Semin. Cell Dev. Biol. **35**, 24–32 (2014)
346. Kerr, J.F., Wyllie, A.H., Currie, A.R.: Apoptosis: a basic biological phenomenon with wide-ranging implications in tissue kinetics. Br. J. Cancer **26**, 239–257 (1972)
347. Degterev, A., Yuan, J.: Expansion and evolution of cell death programmes. Nat. Rev. Mol. Cell Biol. **9**, 378–390 (2008)
348. Arvanitis, M., Li, D.D., Lee, K., Mylonakis, E.: Apoptosis in C. elegans: lessons for cancer and immunity. Front Cell Infect. Microbiol. **3**, 67 (2013)
349. Galluzzi, L., Vitale, I., Abrams, J.M., Alnemri, E.S., Baehrecke, E.H., Blagosklonny, M.V., et al.: Molecular definitions of cell death subroutines: recommendations of the Nomenclature Committee on Cell Death 2012. Cell Death Differ. **19**, 107–120 (2012)
350. Yan, Q., Liu, J.P., Li, D.W.: Apoptosis in lens development and pathology. Differentiation **74**, 195–211 (2006)

351. Taylor, E.L., Rossi, A.G., Dransfield, I., Hart, S.P.: Analysis of neutrophil apoptosis. Methods Mol. Biol. **412**, 177–200 (2007)
352. Kroemer, G., El-Deiry, W.S., Golstein, P., Peter, M.E., Vaux, D., Vandenabeele, P., et al.: Classification of cell death: recommendations of the Nomenclature Committee on Cell Death. Cell Death Differ. **2**, 1463–1467 (2005)
353. Kroemer, G., Galluzzi, L., Vandenabeele, P., Abrams, J., Alnemri, E.S., Baehrecke, E.H., et al.: Classification of cell death: recommendations of the Nomenclature Committee on Cell Death 2009. Cell Death Differ. **16**, 3–11 (2009)
354. Galluzzi, L., Maiuri, M.C., Vitale, I., Zischka, H., Castedo, M., Zitvogel, L., Kroemer, G.: Cell death modalities: classification and pathophysiological implications. Cell Death Differ. **14**, 1237–1243 (2007)
355. Fulda, S., Gorman, A.M., Hori, O., Samali, A.: Cellular stress responses: cell survival and cell death. Int. J. Cell Biol. **2010**, 214074 (2010)
356. Clarke, P.G.: Developmental cell death: morphological diversity and multiple mechanisms. Anat. Embryol. (Berl.) **181**, 195–213 (1990)
357. Kroemer, G., Mariño, G., Levine, B.: Autophagy and the integrated stress response. Mol. Cell **40**, 280–293 (2010)
358. Eisenberg-Lerner, A., Bialik, S., Simon, H.U., Kimchi, A.: Life and death partners: apoptosis, autophagy and the cross-talk between them. Cell Death Differ. **16**, 966–975 (2009)
359. Ellis, H.M., Horvitz, H.R.: Genetic control of programmed cell death in the nematode C. elegans. Cell **44**, 817–829 (1986)
360. Scaffidi, C., Fulda, S., Srinivasan, A., Friesen, C., Li, F., Tomaselli, K.J., Debatin, K.M., Krammer, P.H., Peter, M.E.: Two CD95 (APO-1/Fas) signaling pathways. EMBO J. **17**, 1675–1687 (1998)
361. Muppidi, J.R., Siegel, R.M.: Ligand-independent redistribution of Fas (CD95) into lipid rafts mediates clonotypic T cell death. Nat. Immunol. **5**, 182–189 (2004)
362. Hengartner, M.O.: The biochemistry of apoptosis. Nature **407**, 770–776 (2000)
363. Jost, P.J., Grabow, S., Gray, D., McKenzie, M.D., Nachbur, U., Huang, D.C., Bouillet, P., Thomas, H.E., Borner, C., Silke, J., Strasser, A., Kaufmann, T.: XIAP discriminates between type I and type II FAS-induced apoptosis. Nature **460**, 1035–1039 (2009)
364. Willis, S.N., Adams, J.M.: Life in the balance: how BH3-only proteins induce apoptosis. Curr. Opin. Cell Biol. **17**, 617–625 (2005)
365. Shamas-Din, A., Brahmbhatt, H., Leber, B., Andrews, D.W.: BH3-only proteins: orchestrators of apoptosis. Biochim. Biophys. Acta **1813**, 508–520 (2011)
366. Tourneur, L., Chiocchia, G.: FADD: a regulator of life and death. Trends Immunol. **31**, 260–269 (2010)
367. Festjens, N., Vanden Berghe, T., Vandenabeele, P.: Necrosis, a well-orchestrated form of cell demise: signalling cascades, important mediators and concomitant immune response. Biochim. Biophys. Acta **1757**, 1371–1387 (2006)
368. Sosna, J., Voigt, S., Mathieu, S., Lange, A., Thon, L., Davarnia, P., Herdegen, T., Linkermann, A., Rittger, A., Chan, F.K., Kabelitz, D., Schütze, S., Adam, D.: TNF-induced necroptosis and PARP-1-mediated necrosis represent distinct routes to programmed necrotic cell death. Cell. Mol. Life Sci. **71**, 331–348 (2014)
369. Vandenabeele, P., Galluzzi, L., Vanden Berghe, T., Kroemer, G.: Molecular mechanisms of necroptosis: an ordered cellular explosion. Nat. Rev. Mol. Cell Biol. **11**, 700–714 (2010)
370. Schoenbach, K.H., Joshi, R.P., Stark, R.H., Dobbs, F., Beebe, S.J.: Bacterial decontamination of liquids with pulsed electric fields. IEEE Trans. Dielectr. Electr. Insul. **7**, 637–645 (2000)
371. Beebe, S.J., White, J.A., Blackmore, P.F., Deng, Y., Somers, K., Schoenbach, K.H.: Diverse effects of nanosecond pulsed electric fields on cells and tissues. DNA Cell Biol. **22**, 785–796 (2003)
372. Vernier, P.T., Aimin, L., Marcu, L., Craft, C.M., Gundersen, M.A.: Ultrashort pulsed electric fields induce membrane phospholipid translocation and caspase activation: differential

sensitivities of Jurkat T lymphoblasts and rat glioma C6 cells. IEEE Trans. Dielectr. Electr. Insul. **10**, 795–809 (2003)
373. Hall, E.H., Schoenbach, K.H., Beebe, S.J.: Nanosecond pulsed electric fields induce apoptosis in p53-wildtype and p53-null HCT116 colon carcinoma cells. Apoptosis **12**, 1721–1731 (2007)
374. Ford, W.E., Ren, W., Blackmore, P.F., Schoenbach, K.H., Beebe, S.J.: Nanosecond pulsed electric fields stimulate apoptosis without release of pro-apoptotic factors from mitochondria in B16f10 melanoma. Arch. Biochem. Biophys. **497**, 82–89 (2010)
375. Ren, W., Beebe, S.J.: An apoptosis targeted stimulus with nanosecond pulsed electric fields (nsPEFs) in E4 squamous cell carcinoma. Apoptosis **16**, 382–393 (2011)
376. Chen, X., Yin, S., Hu, C., Chen, X., Jiang, K., Ye, S., Feng, X., Fan, S., Xie, H., Zhou, L., Zheng, S.: Comparative study of nanosecond electric fields in vitro and in vivo on hepatocellular carcinoma indicate macrophage infiltration contribute to tumor ablation in vivo. PLoS One **9**, e86421 (2014)
377. Fadeel, B., Xue, D.: The ins and outs of phospholipid asymmetry in the plasma membrane: roles in health and disease. Crit. Rev. Biochem. Mol. Biol. **44**, 264–277 (2009)
378. Segawa, K., Kurata, S., Yanagihashi, Y., Brummelkamp, T.R., Matsuda, F., Nagata, S.: Caspase-mediated cleavage of phospholipid flippase for apoptotic phosphatidylserine exposure. Science **344**, 1164–1168 (2014)
379. Suzuki, J., Denning, D.P., Imanishi, E., Horvitz, H.R., Nagata, S.: Xk-related protein 8 and CED-8 promote phosphatidylserine exposure in apoptotic cells. Science **341**, 403–406 (2013)
380. Vernier, P.T., Ziegler, M.J., Sun, Y., Gundersen, M.A., Tieleman, D.P.: Nanopore-facilitated, voltage-driven phosphatidylserine translocation in lipid bilayers—in cells and in silico. Phys. Biol. **3**, 233–2147 (2006)
381. Tekle, E., Wolfe, M.D., Oubrahim, H., Chock, P.B.: Phagocytic clearance of electric field induced 'apoptosis-mimetic' cells. Biochem. Biophys. Res. Commun. **376**, 256–260 (2008)
382. Wang, Y., Dawson, V.L., Dawson, T.M.: Poly(ADP-ribose) signals to mitochondrial AIF: a key event in parthanatos. Exp. Neurol. **218**, 193–202 (2009)
383. Charriaut-Marlangue, C., Ben-Ari, Y.: A cautionary note on the use of the TUNEL stain to determine apoptosis. Neuroreport **7**, 61–64 (1995)
384. de Torres, C., Munell, F., Ferrer, I., Reventós, J., Macaya, A.: Identification of necrotic cell death by the TUNEL assay in the hypoxic-ischemic neonatal rat brain. Neurosci. Lett. **230**, 1–4 (1997)
385. Kanoh, M., Takemura, G., Misao, J., Hayakawa, Y., Aoyama, T., Nishigaki, K., Noda, T., Fujiwara, T., Fukuda, K., Minatoguchi, S., Fujiwara, H.: Significance of myocytes with positive DNA in situ nick end-labeling (TUNEL) in hearts with dilated cardiomyopathy: not apoptosis but DNA repair. Circulation **99**, 2757–2764 (1999)
386. Grasl-Kraupp, B., Ruttkay-Nedecky, B., Koudelka, H., Bukowska, K., Bursch, W., Schulte-Hermann, R.: In situ detection of fragmented DNA (TUNEL assay) fails to discriminate among apoptosis, necrosis, and autolytic cell death: a cautionary note. Hepatology **21**, 1465–1468 (1995)
387. Smith, M.A., Schnellmann, R.G.: Calpains, mitochondria, and apoptosis. Cardiovasc. Res. **96**, 32–37 (2012)
388. Song, J., Joshi, R.P., Beebe, S.J.: Cellular apoptosis by nanosecond, high-intensity electric pulses: model evaluation of the pulsing threshold and extrinsic pathway. Bioelectrochemistry **79**, 179–186 (2010)
389. Estlack, L.E., Roth, C.C., Thompson 3rd, G.L., Lambert 3rd, W.A., Ibey, B.L.: Nanosecond pulsed electric fields modulate the expression of Fas/CD95 death receptor pathway regulators in U937 and Jurkat Cells. Apoptosis **19**, 1755–1768 (2014)
390. Beebe, S.J., Sain, N.M., Ren, W.: Induction of cell death mechanisms and apoptosis by nanosecond pulsed electric fields (nsPEFs). Cells **2**, 136–162 (2013)

391. Morotomi-Yano, K., Akiyama, H., Yano, K.: Different involvement of extracellular calcium in two modes of cell death induced by nanosecond pulsed electric fields. Arch. Biochem. Biophys. **555–556**, 47–54 (2014)
392. Ibey, B.L., Ullery, J.C., Pakhomova, O.N., Roth, C.C., Semenov, I., Beier, H.T., Tarango, M., Xiao, S., Schoenbach, K.H., Pakhomov, A.G.: Bipolar nanosecond electric pulses are less efficient at electropermeabilization and killing cells than monopolar pulses. Biochem. Biophys. Res. Commun. **443**, 568–573 (2014)
393. Kotnik, T., Mir, L.M., Flisar, K., Puc, M., Miklavčič, D.: Cell membrane electropermeabilization by symmetrical bipolar rectangular pulses. Part I. Increased efficiency of permeabilization. Bioelectrochemistry **54**, 83–90 (2001)
394. Tekle, E., Astumian, R.D., Chock, P.B.: Electroporation by using bipolar oscillating electric field: an improved method for DNA transfection of NIH 3T3 cells. Proc. Natl. Acad. Sci. U. S. A. **88**, 4230–4234 (1991)
395. Jacobson, J., Duchen, M.R.: Mitochondrial oxidative stress and cell death in astrocytes—requirement for stored Ca^{2+} and sustained opening of the permeability transition pore. J. Cell Sci. **115**, 1175–1188 (2002)
396. Brookes, P.S., Yoon, Y., Robotham, J.L., Anders, M.W., Sheu, S.S.: Ca^{2+}, ATP, and ROS: a mitochondrial love-hate triangle. Am. J. Physiol. Cell Physiol. **287**, C817–C833 (2004)
397. Pakhomova, O.N., Khorokhorina, V.A., Bowman, A.M., Rodaitė-Riševičienė, R., Saulis, G., Xiao, S., Pakhomov, A.G.: Oxidative effects of nanosecond pulsed electric field exposure in cells and cell-free media. Arch. Biochem. Biophys. **527**, 55–64 (2012)
398. Sato, T., Machida, T., Takahashi, S., Iyama, S., Sato, Y., Kuribayashi, K., Takada, K., Oku, T., Kawano, Y., Okamoto, T., Takimoto, R., Matsunaga, T., Takayama, T., Takahashi, M., Kato, J., Niitsu, Y.: Fas-mediated apoptosome formation is dependent on reactive oxygen species derived from mitochondrial permeability transition in Jurkat cells. J. Immunol. **173**, 285–296 (2004)
399. Stacey, M., Stickley, J., Fox, P., Statler, V., Schoenbach, K., Beebe, S.J., Buescher, S.: Differential effects in cells exposed to ultra-short, high intensity electric fields: cell survival, DNA damage, and cell cycle analysis. Mutat. Res. **542**, 65–75 (2003)
400. Romeo, S., Zeni, L., Sarti, M., Sannino, A., Scarfı', M.R., et al.: DNA electrophoretic migration patterns change after exposure of jurkat cells to a single intense nanosecond electric pulse. PLoS One **6**, e28419 (2011)
401. Nuccitelli, R., Pliquett, U., Chen, X., Ford, W., James Swanson, R., Beebe, S.J., Kolb, J.F., Schoenbach, K.H.: Nanosecond pulsed electric fields cause melanomas to self-destruct. Biochem. Biophys. Res. Commun. **343**, 351–360 (2006)
402. Nuccitelli, R., Chen, X., Pakhomov, A.G., Baldwin, W.H., Sheikh, S., Pomicter, J.L., Ren, W., Osgood, C., Swanson, R.J., Kolb, J.F., Beebe, S.J., Schoenbach, K.H.: A new pulsed electric field therapy for melanoma disrupts the tumor's blood supply and causes complete remission without recurrence. Int. J. Cancer **125**, 438–445 (2009)
403. Chen, X., Zhuang, J., Kolb, J.F., Schoenbach, K.H., Beebe, S.J.: Long term survival of mice with hepatocellular carcinoma after pulse power ablation with nanosecond pulsed electric fields. Technol. Cancer Res. Treat. **11**, 83–93 (2012)
404. Chen, R., Sain, N.M., Harlow, K.T., Chen, Y.J., Shires, P.K., Heller, R., Beebe, S.J.: A protective effect after clearance of orthotopic rat hepatocellular carcinoma by nanosecond pulsed electric fields. Eur. J. Cancer **50**, 2705–2713 (2014)
405. Nuccitelli, R., Tran, K., Lui, K., Huynh, J., Athos, B., Kreis, M., Nuccitelli, P., De Fabo, E.C.: Pigment Cell Melanoma Res. **25**, 618–629 (2012)
406. Nuccitelli, R., Wood, R., Kreis, M., Athos, B., Huynh, J., Lui, K., Nuccitelli, P., Epstein Jr., E.H.: First-in-human trial of nanoelectroablation therapy for basal cell carcinoma: proof of method. Exp. Dermatol. **23**, 135–137 (2014)